An Electronically Steered, Wearable Transcranial Doppler Ultrasound System

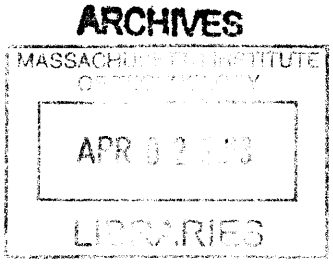

by

Sabino Joseph Pietrangelo

B.S. Electrical Engineering
University of Michigan – Ann Arbor, 2008

Submitted to the Department of Electrical Engineering and Computer Science in partial fulfillment of the requirements for the degree of

Master of Science in Electrical Engineering and Computer Science

at the

MASSACHUSETTS INSTITUTE OF TECHNOLOGY

February 2013

Author .....
Department of Electrical Engineering and Computer Science
December 18, 2012

Certified by .....
Charles G. Sodini
Professor of Electrical Engineering
Thesis Supervisor

Certified by .....
Hae-Seung Lee
Professor of Electrical Engineering
Thesis Supervisor

Accepted by .....
Leslie A. Kolodziejski
Chairman, Department Committee on Graduate Theses

An Electronically Steered, Wearable Transcranial Doppler Ultrasound System

by

Sabino Joseph Pietrangelo

B.S. Electrical Engineering

University of Michigan – Ann Arbor, 2008

Submitted to the Department of Electrical Engineering and Computer Science
on December 18, 2012, in partial fulfillment of the
requirements for the degree of
Master of Science in Electrical Engineering and Computer Science

Abstract

This thesis details the design of a transcranial Doppler (TCD) ultrasound system to measure cerebral blood flow velocity (CBFV) at the middle cerebral artery (MCA). TCD sonography has been clinically indicated in a variety of neurovascular diagnostic applications. Acceptance of conventional TCD methods, however, has been primarily impeded by several constraints, including restrictive system form factors, measurement reliability concerns, and the need for a highly-skilled operator. The goal of this work is to reduce the effects of such limitations through the development of a highly-compact, wearable TCD ultrasound system for autonomous CBFV measurement.

A first-generation, eight channel printed circuit board prototype system has been designed, fabricated, and experimentally tested. Characterization of the prototype system using a Doppler flow phantom resulted in a normalized root-mean-square error of $< 3.5\%$ over the range of expected *in vivo* MCA flow velocities. Extension of the initial prototype to higher channel count systems and the development of phased array beamformation and algorithmic vessel location are also examined in this work. The emergence of simple, robust, and non-invasive neurovascular diagnostic methods presents an enormous opportunity for the advancement of neurovascular monitoring, particularly in applications where – due to restrictions in current diagnostic modalities – standard monitoring procedures have not yet been established.

Thesis Supervisor: Charles G. Sodini
Title: Professor of Electrical Engineering

Thesis Supervisor: Hae-Seung Lee
Title: Professor of Electrical Engineering

Acknowledgments

First, I'd like to thank my parents and sisters for their enduring support, understanding, and faith in me as both an individual and a student. I cannot imagine completing this adventure without the persistent motivation and encouragement from my family members. I would like to express my deepest gratitude to my research advisors – Professors Charlie Sodini and Hae-Seung Lee – for their mentorship, advice, and technical intuition.

The generous support of MIT Lincoln Laboratory and the lasting guidance and inspiration from Dr. Helen Kim is greatly appreciated and has made my graduate studies a practical reality. I would also like to acknowledge Maxim Integrated, especially Dr. Brian Brandt, for believing in the vision of this research and supporting the progression of my project.

Members of the Computational Physiology and Clinical Inference Group at MIT have been incredibly helpful – especially Dr. Thomas Heldt, for his vast knowledge of physiology and biomedical research, and Dr. Faisal Kashif, whose groundbreaking work in noninvasive intracranial pressure estimation provided the impetus for this research. I would like to acknowledge Ron Gatzke (of Gatzke Technologies) and Dr. Kai Thomenius (of GE Global Research) for their extraordinary technical expertise in the field of medical ultrasound and for helping me to make sense of a seemingly overwhelming number of technical details.

Lastly, I'd like to thank my friends – especially Anton Hunt, Michael Street, and Michael Tomovich – for demanding that I maintain a minimum amount of work-life balance and sustenance during even the most trying periods of my research. Thanks also to all my colleagues in 38-265 for creating an enjoyable – and memorable – office environment and for helping me to advance beyond the many difficulties encountered throughout the course of my research. Help from Kailiang Chen was particularly useful in troubleshooting ultrasound hardware and experimental testing issues.

This work was sponsored in part by generous support from the MIT Medical Electronic Device Realization Center (MEDRC) and MIT Lincoln Laboratory.

Contents

List of Figures

List of Tables

Chapter 1

Introduction

1.1 Background

The brain, due to its high metabolic rate, is vitally dependent on continually attaining sufficient oxygenation. A complex autoregulatory system within the cerebral vasculature enables stable perfusion across a wide range of cerebral perfusion pressures (CPPs). Regulation is achieved by closely matching oxygen supply to demand in brain tissue through the constriction and dilation of cerebral arteries and arterioles [1,2]. However, under extremely hypertensive – or hypotensive – conditions and certain cerebrovascular pathologies, these regulation mechanisms become impaired and the body can no longer support adequate cerebral blood flow (CBF). Neurological symptoms appear within seconds of brain tissue ischemia and, if conditions persist, a high risk of irreversible brain damage exists [3].

The central objective of critical care for patients affected by neurotrauma, cerebrovascular accident (i.e., stroke), and other neurovascular pathologies is to monitor patient state and provide suitable medical intervention to mitigate secondary injury and aid in recovery [3]. While several non-invasive cerebrovascular diagnostic modalities exist, including positron emission tomography (PET) and magnetic resonance angiography (MRA), the use of transcranial Doppler (TCD) sonography is highly compelling for certain diagnostic needs due to its safety in prolonged studies, high temporal resolution, and relative portability [4,5].

TCD sonography is a specialized Doppler ultrasound technique that enables the measurement of blood flow velocities from the basal intracerebral vessels. Clinically relevant parameters, including peak-systolic and end-diastolic flow velocities, time-averaged flow velocity, and pulsatility index, are extracted from time-varying cerebral blood flow velocity (CBFV) measurements. TCD sonography is primarily used clinically in the identification of intracranial vasospasm and stenosis, cerebral embolism detection, intra-operative monitoring, and assessment of cerebrovascular autoregulation.

Intracranial vasospasm is a delayed contraction of the cerebral vessels and is a major cause of mortality following aneurysmal subarachnoid hemorrhage (SAH) [2]. Spasm, which results in stenosis and a consequent increase in CBFV, is induced by sustained contact between blood products and the cerebral vessel wall. The onset of cerebral vasospasm, if experienced following SAH, generally occurs roughly three days after hemorrhaging and may be episodic in nature [6]. Continuous monitoring of the cerebral vasculature is desired as intermittent measurements may exclude significant transients and subsequently lead to misdiagnoses or delays in medical intervention [2]. Studies have demonstrated a high sensitivity and positive predictive value in the identification of vasospasm using TCD measurements of CBFV in these patient populations [7–9]. Other causes of intracranial stenosis, such as atheromatous disease and sickle cell anemia, are more persistent and require repeated measurements throughout the course of therapy. In the case of sickle cell anemia, periodic evaluation of stenosis severity using TCD and subsequent treatment, where appropriate, can significantly reduce the occurrence of stroke in children with the disease [10, 11].

Among non-invasive diagnostic methods, TCD is uniquely capable of detecting both gaseous and solid circulating cerebral emboli [4]. Embolus dimensions are approximately the same magnitude as acoustic wavelengths used in diagnostic ultrasound. The presence of an embolus within the volume of insonation therefore results in specular reflection of acoustic energy, which appears as a high intensity transient in the Doppler sonogram. In patients with symptomatic carotid artery stenosis, detection of cerebral emboli has been shown to be an independent predictor of risk for

transient ischemic attack (TIA) and embolic stroke [12]. Monitoring of cerebral emboli may also prove useful in assessing patient response to antithrombotic agents [13].

TCD is well-suited for intra-operative monitoring due to its minimal restrictions on environmental surroundings and relatively unobtrusive measurement procedure. In patients with inadequate collateral cerebral routes undergoing carotid endarterectomy, impaired collateral flow is identified by markedly diminished CBFV in the ipsilateral middle cerebral artery (MCA) during cross-clamping of the carotid artery. If CBFV measurements fall below prescribed thresholds during the procedure, surgical intervention (e.g., insertion of a temporary intraluminal shunt) can reduce the risk of cerebral ischemia [14]. In addition, TCD is commonly used to detect cerebral emboli during carotid endarterectomy and cardiopulmonary bypass surgery, which may aid the surgeon in locating the embolic origin and reducing their occurrence [5, 15, 16].

The high temporal resolution of TCD is necessary for evaluation of cerebral hemodynamics. Cerebral autoregulatory function can be assessed directly, by inducing a rapid disturbance in arterial blood pressure (ABP), or indirectly, through carbon dioxide reactivity testing. In direct evaluation, simultaneous measurements of CBFV via TCD and instantaneous ABP – non-invasively via Portapres unit (Finapres Medical Systems, Amsterdam, NL) or minimally-invasively via arterial line – are required. A step decrease in ABP is achieved by rapid deflation of a thigh cuff. When unimpaired, cerebral autoregulatory mechanisms cause CBFV to return to its baseline value more rapidly than ABP. The rates of return to homeostasis for CBFV and ABP can be used to derive an index of cerebral autoregulatory function [4]. Diminished cerebral autoregulation is common following head injury and is associated with trauma severity and increased mortality. Cerebral autoregulatory evaluation may therefore be useful in the management of therapy for patients under neurocritical care [2, 17].

An exciting, but evolving, application of TCD velocimetry is the real-time assessment of intracranial pressure (ICP). ICP is the pressure of cerebrospinal fluid (CSF) within the cranial vault and is a key factor in neurocritical monitoring and subsequent therapeutic guidance. Recent developments in model-based physiological signal processing have shown great promise in non-invasive estimation of ICP using

simultaneous CBFV and ABP measurements [3,18]. Elevated ICP, known as intracranial hypertension, is frequently found in cases of severe traumatic brain injury (TBI) and is directly correlated with poor patient outcome [19]. TBI occurs when an external force acts to injure the brain, resulting in disrupted brain function, and is a major cause of morbidity and mortality in the developed world, occurring annually in an estimated 1.7 million persons in the United States alone [2,20]. Early identification of TBI severity, along with continuous ICP monitoring and proper medical intervention, can greatly lower the risk of secondary injury and improve patient outcome [21].

TCD evaluation has also been clinically indicated for determination of prognosis following acute stroke, identification of arteriovenous malformations, and confirmation of brain death. A comprehensive review of clinical TCD sonography applications and an evidence-based assessment of diagnostic merit for each application can be found in [22].

1.2 Motivation

Despite a number of proposed advantages and a growing list of potential diagnostic applications (e.g., functional TCD and intracranial pressure estimation), use of TCD sonography is often confined to highly-specific clinical environments (e.g., neurocritical care units and vascular laboratories) and the reliability of TCD velocimetry data has not been generally accepted by the medical community [23, 24]. Several notable constraints have impeded the extension of current TCD ultrasound techniques to a wider variety of contexts. These limitations include the need for an experienced TCD sonographer, operator dependent measurement results, the lack of a patent acoustic window in significant portions of the patient population, and inadequate TCD system architecture and form factor in certain emerging applications.

Conventional TCD ultrasound systems employ a single element transducer that must be manually steered by a skilled TCD sonographer, requiring fine manual dexterity, proficient knowledge of the underlying cerebral anatomy and characteristic Doppler waveforms, and extensive training (with a recommended 25 to 50 supervised

TCD examinations) [14, 23, 25]. Even in environments where such expertise is accessible, there can be critical delays in the administration of TCD examination and the availability of measurement results, thus often excluding the use of TCD sonography by emergency medical personnel for rapid diagnosis of time-sensitive disorders. During prolonged TCD monitoring, a headframe can be employed to hold the transducer in position after an acceptable Doppler signal is obtained for the vessel of interest. Patient movement and environment dynamics can, however, cause probe misalignment and a consequent loss of signal fidelity. The frequency of probe displacement effects is highly dependent on measurement application, being more problematic in prolonged evaluation of non-comatose patients. The operator (i.e., sonographer) must therefore assess measurement results during the course of TCD monitoring, ensuring adequate signal quality and suitable probe placement [24].

The integration of power motion-mode Doppler (PMD), which uses multi-gate sampling to provide flow signal intensity and direction across a broad range of intracranial depths, into conventional TCD ultrasound systems facilitates cranial window location and beam alignment [26]. Visualization of flow in TCD systems via PMD intensity imaging allows the operator to manually steer the transducer solely through visual feedback rather than by traditional auditory Doppler cues [27]. Developments in transcranial color-coded duplex sonography (TCCS) also expedite vessel location procedures by incorporating color flow imaging (CFI) capabilities into TCD ultrasound systems. Transcranial ultrasound imaging of flow velocity via CFI, however, suffers from exceedingly poor spatial resolution due primarily to distortion of the ultrasound beam through cranial bone [28].

CFI can be advantageous in gaining a general impression of hemodynamics within a region of interest and identifying several specific pathologies (e.g., arteriovenous malformation, aneurysm), but yields less accurate CBFV measurements than conventional TCD techniques. Therefore, when quantitative CBFV data is required, CFI can be employed to spatially locate the vessel and conventional TCD is used for velocimetry [28]. While technological developments such as PMD and TCCS are beneficial in providing a richer set of information regarding the cerebral vasculature

and improving the usability of TCD hardware, a qualified sonographer is still decidedly necessary throughout the extent of transcranial ultrasound examination. Such expertise is unavailable or impractical in many circumstances where the diagnostic capabilities of TCD sonography would otherwise be appropriate and advantageous.

General acceptance of TCD sonography as a clinically relevant medical diagnostic is confounded by critical deficiencies in measurement accuracy and reproducibility [29]. In practice, Doppler ultrasound velocimetry is a highly operator dependent technology. TCD sonography is especially reliant on operator technique due to pronounced signal attenuation and acoustic reflection caused by cranial bone and severely diminished, if any, imaging capabilities. TCD velocimetry measurements are predominately affected by operator proficiency in acoustic window location, vessel identification (including anatomic variations), probe angulation, region of insonation placement within the vessel of interest, and to a lesser degree, selection of sample volume extent, pulse repetition frequency, acoustic transmit power, Doppler filtering parameters, and receiver gain.

Measurement accuracy is principally related to operator experience, with measurement error being lowest in highly-trained, well-practiced sonographers [23]. The level of measurement error that is clinically acceptable for TCD velocimetry measurements, however, is unknown and greatly dependent on clinical application. Among expert technologists within an accredited vascular laboratory, Doppler measurements exhibited significant inter-operator variability (for peak systolic velocities in the extracranial internal carotid), leading to difficulties in evaluating the progression of stenosis beyond broad categorization (i.e., $< 50\%$, $50\% - 70\%$, and $> 70\%$ diameter reduction) [30].

Similar conclusions were reached in a TCD study, where moderate variability was found among experienced users resulting in a mean inter-operator difference of 1.8 cm/s (with 95% limits of agreement at ± 22.1 cm/s) for mean CBFV in the MCA [29]. Aberrant results in several examinations, however, led the authors to conclude that caution should be used when interpreting isolated MCA velocity measurements and that serial CBFV data must be combined with other clinical parameters

prior to the evaluation treatment options (with angiography – an invasive method – being the only reliable means of detecting intracranial vasospasm) [29, 31]. CBFV measurement error is not confined solely to operator competence, but is also influenced by TCD system design considerations (e.g., Doppler processing algorithms) and physical limitations (e.g., variability of acoustic propagation velocity within tissue). Technological developments that enhance TCD signal processing capabilities and lessen the reliance on operator participation and expertise to achieve accurate transcranial velocimetry data promise to bring rapid and definitive diagnoses for a wide variety of neurological conditions and to greatly expand the acceptance and use of TCD sonography across a broad range of clinical environments.

A recurrent challenge associated with the use of TCD sonography remains the lack of a patent acoustic window (i.e., no detectable receive Doppler signal) in approximately 5 – 10% of subjects [4,5]. Absence of a patent temporal acoustic window (TAW) – the sole location from which the MCA can be insonated – was observed in 8.2% of individuals [32]. Lack of a satisfactory TAW is principally related to increased thickness of the temporal bone squama and is markedly more prevalent in non-white races, females, and patients aged 65 and older [32]. Because a majority of patients with cerebrovascular disease are elderly, age dependent effectiveness creates a substantial concern for the clinical acceptance of TCD sonography.

Ultrasonic contrast agents can generally be used to diminish TAW patency effects by considerably enhancing the effective scattering coefficient of blood and therefore greatly increasing the intensity of the received backscatter signal [33]. However, administration of contrast agents requires intravenous injection, making the examination an invasive procedure and notably complicating its administration.

Experimental studies reveal that transmission of ultrasound through cranial bone also leads to substantial and irregular acoustic refraction, thereby severely distorting acoustic beam shape, further reducing peak intensity within the sample volume, and greatly increasing the intensity of secondary lobes [34, 35]. Refraction effects can be mitigated in phased array based TCD systems through the use of phase-correction. The development of phase-correction algorithms for low-frequency (i.e., 0.74 MHz)

transcranial focused ultrasound has demonstrated success in restoring beam shape and acoustic intensity for transmission through *ex vivo* cranial bone – increasing peak focal intensities by a factor of 2.5 or more compared to the uncorrected measurement [36]. Refinements to phase-correction methods and their application to TCD sonography will lead to substantial increases in acoustic intensity at the vessel of interest while maintaining fixed acoustic output power. Such advancements are essential to further acceptance of TCD sonography by clinicians, as they are expected to improve TAW patency rates without a corresponding increase in the thermal cranial index (TIC) – a quantity that characterizes changes in tissue temperature, which is the relevant safety metric in most applications of transcranial ultrasound [28].

Although traditional cart-based TCD systems are fairly compact and inexpensive relative to other cerebrovascular diagnostic modalities, the use of TCD sonography in unconventional and emerging applications can be prohibitively constrained by system integration and architecture decisions (e.g., form factor, operator interface, electrical connectivity, cost). A notable limitation of standard TCD examinations is the severe restriction on patient movement throughout the procedure, making extended TCD evaluations in non-comatose patients remarkably challenging [24]. The development of wearable systems for ambulatory TCD recordings of cerebral emboli has, to a degree, overcome this concern and achieved prolonged monitoring in patients with carotid stenosis – an essential requirement in determining temporal variability in embolization [13, 37]. Such systems, however, provide reduced capabilities beyond their intended application (e.g., lack of real-time measurement data, need for manual signal quality assessment and probe adjustment throughout the monitoring period).

Advances in wearable TCD systems that allow real-time data processing and elimination of operator engagement during the course of measurement (i.e., autonomous operation) will be extremely useful in the application of TCD based ICP estimation. Current ICP measurement modalities are highly invasive, relying on surgical penetration of the skull and placement of an intracranial transducer. Consequently, ICP measurements are typically withheld except in cases where evidence of severe TBI can justify the risks of infection and surgical complications inherent in conventional

ICP measurement techniques. Cases of TBI that appear to be mild or moderate in severity are thus evaluated solely by indirect means, such as neurological examination and medical imaging. While these methods can provide useful information to clinicians, they at best determine a patient's state at a fixed point in time and prove ineffective in capturing the transitory behavior associated with secondary injury that continuous ICP monitoring can provide. Therefore, an alternate means of measuring ICP – over the course of hours or several days – without penetration of the skull will yield a significant benefit to TBI patients, especially in cases where the use of invasive procedures may be avoidable. The realization of a reliable, easy to use method for non-invasive ICP monitoring will be a crucial development in the diagnosis and treatment of brain trauma and various neurological disorders (e.g., hydrocephalus, brain tumor, repeated concussion, intracranial hematoma) [3].

TCD is rapidly evolving from a simple screening tool to a diagnostic modality with a broad spectrum of clinical applications and a direct impact on patient management [27]. Enabling technological advancements and a changing atmosphere toward point-of-care testing and mobile health paradigms has stimulated a renewed interest in portable, non-invasive, and highly usable tools for cerebrovascular monitoring and diagnostics.

1.3 Approach

This work details the development of a highly-compact, wearable TCD ultrasound system for prolonged, autonomous measurement of CBFV in support of neurovascular monitoring.

The use of a two-dimensional (2D) ultrasound transducer array and beam steering algorithm allows for autonomous vessel location and tracking. Automated mechanical steering – via servo control – has been previously investigated and successfully demonstrated for TCD vessel tracking, but is considerably limited by the single allowable steering direction of a transducer element [13,37]. A phased array approach, in contrast, can establish multiple concurrent focal regions and thereby achieve back-

ground vessel tracking and focal point optimization during (i.e., without interruption to) flow velocity measurements. Phased array implementations – in addition to beam steering – enable dynamic beam focusing, which yields a significant increase in acoustic intensity at the region of interest than can be achieved, for a fixed acoustic output power, from the planar (i.e., unfocused) single element transducers commonly used in TCD instrumentation [27,37]. Additionally, phased array beamformation permits the application of phase-correction techniques to further improve energy focusing and mitigate the effects of refraction and focal aberrations [34,35].

Recent advances in ultrasound electronics and system architectures have led to substantial reductions in ultrasound instrumentation dimensions (e.g., GE Vscan, Siemens ACUSON P10). This work extends such reductions in system dimensions to a wearable form factor by identifying the anatomical, physiological, and algorithmic constraints particular to portable TCD sonography.

To facilitate development and limit system complexity, this work concentrates on unilateral TAW insonation of the MCA for velocimetry applications. Although this decision generally restricts the clinical utility of the system, it proves sufficient for a number of TCD applications – particularly non-invasive ICP estimation, a primary motivation for this research. Of the major cerebral vessels, insonation and spectral Doppler (i.e., non-imaging) identification of the MCA through the TAW is generally the most straightforward due to favorable anatomical structure. The MCA is a high flow velocity, relatively large diameter cerebral vessel with approximately lateral course (i.e., normal to skull surface). TAW insonation of the ipsilateral MCA thereby typically results in moderate steering angle magnitude ($< 15°$ in azimuth and elevation planes), negligible Doppler angle, and moderate insonation depths (30 – 60 mm). Further efforts to expand insonation capabilities to additional cerebral vessels (e.g., anterior and posterior cerebral arteries) will not be discussed; the majority of analyses and designs presented in this work, however, remain valid.

Ultrasound field solvers, particularly Field II, are used extensively in the evaluation and refinement of transducer array designs and Doppler processing algorithms [38,39]. Although such simulation tools do not provide a suitable treatment

of noise effects, nonlinearities, and bulk inhomogeneities, they are useful in validating functionality and comparing design performance metrics – especially relative to existing TCD systems – using simplifying assumptions.

To expedite development, initial system architecture configurations for this work leverage commercially available discrete electronic components. Because access to internal nodes within discrete components is restricted and device operation is generally predefined, this decision severely limits the extent of realizable architectures. For this work, a fully digital phased array, with dedicated transmit and receive electronics for each array element, was selected due to its fully software defined configurability and ease of implementation when utilizing existing commercial electronics. Although this approach is somewhat excessive in terms of electronic hardware, power dissipation, and intermediate data rates – as compared to more elegant mixed-signal architectures – it provides a reasonable means of determining the viability of wearable TCD sonography, typical underlying signal levels, and algorithm performance for practical *in vivo* measurements. Following concept validation – but beyond the scope of this current work – significant reductions in system size and power dissipation can be realized through the effective design and implementation of integrated circuit electronics.

This work describes the design and evaluation of a prototype TCD system and examines expansion to higher channel count systems. The prototype system, referred to as Prototype I in this work, was designed, fabricated, and experimentally tested. Prototype I is an eight channel system employing single element transducers and was developed to validate transmit and receive electronics, processor system control, and Doppler signal processing methods. The Prototype I transmit and receive signal paths were tested electrically and Doppler velocimetry was experimentally validated using a flow phantom. Clinical *in vivo* validation of Prototype I for CBFV measurements at the MCA will also be investigated by comparing velocimetry data to measurements from a commercial TCD system, but has not yet been completed.

Future designs leverage the system architecture and Doppler signal processing methods found in Prototype I, but extend the system to 64 channel operation. A custom transducer matrix (i.e., 2D array) has been designed for these systems and it's

simulated characteristics are examined. With the addition of a phased array capable transducer, electronic beam steering algorithms for vessel location and tracking can be developed and experimentally refined.

1.4 Thesis Organization

This thesis begins with a general description of acoustic wave theory, transducer characterization, Doppler velocity estimation, and other concepts applicable to the functionality of TCD instrumentation in Chapter 2. Following an explanation of fundamental TCD principles of operation, Chapter 3 presents an overview of the relevant cerebrovascular anatomy, expected relationships between physiological variables and acoustic waveforms, and conventional techniques for TCD examination.

From recognition of the salient system parameters for TCD velocimetry applications, the system architecture, hardware design, and prototype TCD system implementation are defined in Chapter 3. Chapter 4 presents the results from electrical testing of the Prototype I system. Validation of the velocity estimation procedures is performed experimentally for the Prototype I system using a flow phantom under realistic flow velocities and vessel dimensions.

Lastly, this work is summarized in Chapter 5. Functionality and performance of the devised system architectures, as well as extensions to more capable systems for general TCD applications, are discussed. Necessary future work and the identification of practical enhancements to subsequent system implementations are also presented.

Chapter 2

Theory of Operation

2.1 General Ultrasound Principles

Ultrasound is a cyclic acoustic disturbance at frequencies above the limit of human hearing ($>$ 20 kHz). Acoustic energy perturbs the particles composing a propagating medium, causing them to oscillate about their equilibrium positions with no net displacement and producing local fluctuations in pressure. Because fluids continually deform under shear stress, a fluid medium can only support longitudinal acoustic waves, thereby confining particle motion along the direction of propagation. Human tissue is predominately an elastic solid comprised of complex structural formations and nonuniform interfaces. Due to its high water content, tissue is often approximated as a fluid acoustic medium. This simplification is less appropriate for highly anisotropic (e.g., striated muscle) and particularly dense (e.g., bone) structures, but allows reasonably tractable analysis of ultrasonic radiation through basic tissue formations.

Acoustic waves, like all physical processes, are fundamentally nonlinear. Finite pressure amplitudes cause variations in wave velocity, resulting in progressive waveform distortion and harmonic frequency generation [40]. Nonlinearities also lead to a phenomenon known as acoustic saturation, where pressure amplitudes asymptotically approach a material dependent maximum as source output power increases [41]. Nonlinear effects are exploited in certain uses of medical ultrasound (e.g., harmonic

imaging, therapeutic ultrasound). Diagnostic applications, however, typically involve low to moderate acoustic output power with significant attenuation through tissue and linear propagation is generally assumed. In practice, pressure amplitudes can become a considerable fraction of static pressure and the linear assumption is often not strictly valid [42]. Nonetheless, the use of linear acoustic models for diagnostic ultrasound applications is normally justified as they capture most salient features of propagation and provide valuable insight into underlying phenomena without excessively complicating analysis. An in-depth discussion of elastic waves in solids and nonlinear acoustics are beyond the scope of this thesis and are described fully in [40]. A fluid acoustic medium and linear wave propagation are appropriate for most uses in diagnostic sonography and will be assumed for the remainder of this work, unless explicitly stated.

Consequently, vibrations in Cartesian space can be described by the linear wave equation:

$$\left(\frac{\partial^2}{\partial x^2}+\frac{\partial^2}{\partial y^2}+\frac{\partial^2}{\partial z^2}\right)u(x,y,z,t)=\frac{1}{c^2}\frac{\partial^2 u(x,y,z,t)}{\partial t^2} \tag{2.1}$$

where u denotes the magnitude of instantaneous particle velocity (i.e., $u = |\vec{u}|$), (x, y, z, t) are spatiotemporal Eulerian coordinates, and c is the velocity of propagation. The wave equation can, in general, express multiple modes of propagation. However, because a fluid medium is assumed, longitudinal mode vibration is implied.

Propagation velocity (c) and wavelength (λ) are influenced by the mechanical properties of a medium. Although velocity is strictly dependent on wave amplitude, use of the linear propagation assumption yields a single value within a given medium – assuming negligible dispersion effects.

$$c=\sqrt{\frac{1}{\rho_0\kappa}} \tag{2.2}$$

$$\lambda=\frac{c}{f}=\frac{1}{f\sqrt{\rho_0\kappa}} \tag{2.3}$$

where f is the frequency of oscillation (related to angular frequency ω by $f = \frac{\omega}{2\pi}$), ρ_0 is mean density, and κ is the adiabatic compressibility of the material [43].

Pressure variations (p) – referenced to static pressure – and particle velocity magnitude are related by the characteristic acoustic impedance Z. In general, the relationship between p and u may vary with position and exhibit non-zero phase. However, Z is normally assumed to be purely real and solely dependent on the acoustic medium:

$$Z = \frac{p}{u} = \rho_0 c \tag{2.4}$$

The characteristic acoustic impedance is typically given in units of rayls ($1\,\text{rayl} = 1\,\text{kg} \cdot \text{s}^{-1} \cdot \text{m}^{-2}$) and is particularly significant at the interface of dissimilar media due to reflection effects [40].

Attenuation in tissue arises from several complex phenomena and is exceedingly difficult to precisely derive from fundamental principles. Thermo-viscous effects in physical media result in absorption, which is typically the dominant cause of attenuation in medical ultrasound applications, accounting for $85 - 90\%$ of attenuative losses in macroscopically homogeneous tissue [40]. Scattering and mode-conversion also contribute to attenuation, although often nominally within a given material. Simple phenomenological models are generally used to combine these distinct sources of energy loss by employing a single frequency-dependent attenuation factor $\alpha(f)$:

$$\alpha(f) = \alpha_0 + \alpha_1 f \tag{2.5}$$

where the offset term is commonly neglected ($\alpha_0 \approx 0$), α_1 is determined empirically for a specific tissue type, and α is often expressed in $\text{Np} \cdot \text{cm}^{-1}$. Because both are based on the logarithmic scale, the Neper can be easily converted to decibels ($1\,\text{Np} = 8.686\,\text{dB}$) when needed. Attenuation has significant influence on the design and use of medical ultrasound instrumentation. As acoustic frequency increases, resolution increases (related to wavelength) while depth of penetration decreases (related to attenuation and acceptable signal to noise ratio). The appropriate magnitude of these opposing factors is therefore highly dependent on application specific constraints.

Approximate acoustic parameters are given for media relevant to transcranial Doppler (TCD) applications in Table 2.1. For biological media, acoustic properties are

highly influenced by myriad factors (e.g., blood hematocrit, tissue water content, bone density) and can differ appreciably between specimen and in varying environmental conditions.

Table 2.1: Acoustic parameters for selected media [28, 44].

Medium	Phase Velocity, c [m/s]	Impedance, Z [Mrayl]	Atten. Coefficient, α_1 [Np/ (cm · MHz)]
Air	333	0.0004	—
Water	1480	1.48	0.0002
Soft Tissue	1540	1.63	0.08
Blood	1580	1.67	0.02
Brain	1460	1.50	0.06
Cranial Bone	2770	4.80	2.5

While the general wave equation is suitable for full-wave numerical simulations, it affords limited intuitive and analytical utility. Particular solutions to the general wave equation under bounded domains facilitate the study of several relevant geometries. The spherical wave equation, which describes the harmonic emission of acoustic energy from an infinitesimal radiator within a homogeneous medium, is fundamental to the analysis of acoustic fields. Using Huygens' principle, any finite radiator can be accurately characterized by an equivalent set of exceedingly small ($\ll \lambda$) sources, each radiating a spherical wave. For a monochromatic radiator at the origin, the pressure of an outwardly propagating spherical wave can be expressed as:

$$p(r,t) = \frac{p_s\, e^{-\alpha(f)r}}{r} \sin(2\pi f t - kr) \tag{2.6}$$

where $r = |\vec{r}| = |(r_x, r_y, r_z)|$ is the magnitude of the spatial vector from the origin to the field observation point P, p_s is an amplitude scale factor, and k is the angular wavenumber given by $k = \frac{2\pi}{\lambda}$ [43]. At extremely short distances from the radiator, where $r \to 0$, the spherical wave equation no longer adequately represents physical

reality since the linear approximations used in its derivation become invalid as pressure increases without bound. For medical ultrasound applications, radial distances of interest (i.e., $r > \lambda$) typically exceed such regimes and use of the spherical wave equation remains justified.

At sufficiently far distances from an acoustic source, the resulting pressure field can be approximated as a plane wave over short transverse distances. In this region, known as the far-field of the source ($r \gg \lambda$ for an infinitesimal radiator), spatial variations in pressure amplitude are markedly reduced, allowing reliable field measurements for source characterization. In addition to being particularly mathematically tractable, plane waves can be used in conjunction with the spatial Fourier transform to synthesize the far-field beam pattern of a transducer geometry. At depth z, the pressure of a harmonic plane wave propagating in the $+z$ direction can be expressed as:

$$p(z,t) = p_0\, e^{-\alpha(f)z} \sin\left(2\pi f t - kz\right) \tag{2.7}$$

where p_0 is the pressure amplitude at $z = 0$.

For analysis of acoustic fields, it is often convenient to define a plane wave existing over a limited transverse extent, referred to as a plane wave region. A harmonic plane wave region propagating in the $+z$ direction is expressed as:

$$p(x,y,z,t) = \begin{cases} p_0\, e^{-\alpha(f)z} \sin\left(2\pi f t - kz\right), & x, y \in S_{pw} \\ 0, & \text{otherwise} \end{cases} \tag{2.8}$$

where S_{pw} is a planar region perpendicular to the direction of propagation that defines the transverse extent of the plane wave.

Acoustic intensity (I), known also as power density, is the instantaneous flux of acoustic power across a unit area normal to the direction of propagation. Intensity has a spatiotemporal dependence and is expressed as:

$$I(\vec{r},t) = p(\vec{r},t) \cdot u(\vec{r},t) = \frac{p(\vec{r},t)^2}{Z} = u(\vec{r},t)^2 \cdot Z \tag{2.9}$$

where I is often given in units of $\mathrm{mW} \cdot \mathrm{cm}^{-2}$ for medical ultrasound applications.

Time averaged intensity $\langle I \rangle_t$ is useful in representing acoustic fields for pulsed ultrasound architectures as it removes temporal dependence:

$$\langle I(\vec{r}) \rangle_t = \frac{1}{T_{PRP}} \int_0^{T_{PRP}} I(\vec{r}, t)\, dt \tag{2.10}$$

where T_{PRP} is the pulse repetition period (i.e., the time between successive pulses).

Acoustic intensity is highly relevant in characterizing safe use and regulatory limitations of ultrasound systems. Several derived variants, notably spatial-peak-temporal-peak intensity (I_{SPTP}) and spatial-peak-temporal-averaged intensity (I_{SPTA}), allow the strength of a complicated acoustic field to be quantified by a single value:

$$I_{SPTP} = \max\{I(\vec{r}, t)\} \tag{2.11}$$

$$I_{SPTA} = \frac{1}{T_{PRP}} \int_0^{T_{PRP}} I(\vec{r}_{\max}, t)\, dt \tag{2.12}$$

where $\max\{\cdot\}$ denotes the maximum value across all valid inputs (i.e., $0 \leq t < T_{PRP}$ and $r_z > 0$) and $\vec{r}_{\max}$ is the position of maximum intensity.

2.1.1 Acoustic Scattering

Scattering is the underlying physical phenomena that enables the use of ultrasound for diagnostic purposes. Neglecting non-idealities, an ultrasound B-mode image simply characterizes the magnitude of a backscattered signal as a function of the spatial position of insonation. In Doppler sonography, backscattered energy from a collection of scatterers is utilized to determine particle velocities.

Scattering of ultrasound energy occurs due to deviations in acoustic properties (e.g., density, compressibility) of the propagating medium. The behavior of acoustic waves upon encountering a scatterer (i.e., region with distinct acoustic properties) is highly affected by the dimensions of the scatterer relative to acoustic wavelength. Biological media contains structure over a wide range of length scales (e.g., molecules,

cells, organs). In general, scattering effects can be separated into three dimension dependent categories: specular scattering, diffusive scattering, and diffractive scattering [40].

Specular Scattering

Specular scattering, known simply as reflection, occurs for scatterer boundaries much larger than acoustic wavelength and can be accurately analyzed using basic ray theory. Reflection mechanisms are independent of acoustic frequency, but are markedly influenced by boundary shape. A planar surface (i.e., flat boundary between dissimilar media) acts as a specular scatterer when $\min\{l_s\} \gg \frac{\lambda}{\pi}$, where $\min\{l_s\}$ is the smallest dimension of the surface. Certain organ boundaries and interfaces between bone and soft tissue can be approximated as planar surfaces over a restricted transverse extent. Although of limited utility in the precise analysis of acoustic propagation within physical tissues structures, insight into the basic principles of reflection greatly aid in recognizing the function and inherent limitations of diagnostic sonography.

In the specular regime, the interaction of an incident plane wave with a planar surface yields both reflected and transmitted plane waves, as shown in Figure 2-1, where Z_1 and Z_2 are the acoustic characteristic impedances of the incident and transmit media, respectively.

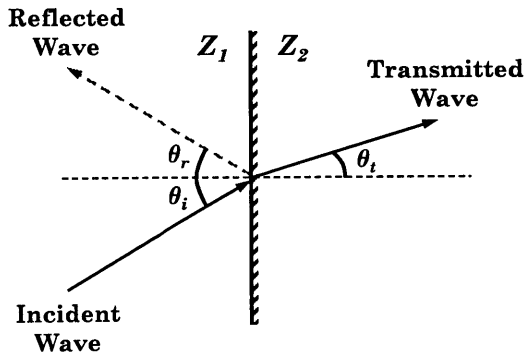

Figure 2-1: Specular scattering at a planar surface.

The relationship between the angles of incidence (θ_i), reflection (θ_r), and trans-

mission (θ_t) are determined using Snell's law [45].

$$\theta_r = \theta_i \tag{2.13}$$

$$\frac{\sin\theta_t}{\sin\theta_i} = \frac{c_t}{c_i} \tag{2.14}$$

where c_i and c_t are the propagation velocities within the incident and transmitted media, respectively. The resulting variation between the angle of incidence and angle of transmission is known as refraction. Recall from Table 2.1 that acoustic propagation velocity remains nearly constant for all soft tissue types, but diverges markedly in bone. Refraction effects are therefore most pronounced at interfaces between bone and soft tissue, particularly at oblique angles of incidence. For TCD applications, refraction due to cranial bone can lead to considerable beam pattern distortion, further complicating intracranial examination [34,35].

The reflection coefficient (Γ) and transmission coefficient (T) describe the ratio between pressure wave magnitudes at the reflecting boundary. Assuming plane wave propagation:

$$\Gamma = \frac{p_r}{p_i} = \frac{Z_2\cos\theta_i - Z_1\cos\theta_t}{Z_2\cos\theta_i + Z_1\cos\theta_t} \tag{2.15}$$

$$T = \frac{p_t}{p_i} = \frac{2Z_2\cos\theta_i}{Z_2\cos\theta_i + Z_1\cos\theta_t} \tag{2.16}$$

where p_i, p_r, and p_t are the amplitudes of the incident, reflected, and transmitted pressure plane waves at the material interface, respectively.

Similarly, reflectivity (Γ_I) and transmissivity (T_I) characterize the relationship between acoustic plane wave intensities at the reflecting boundary [43]:

$$\Gamma_I = \frac{I_r}{I_i} = \Gamma^2 = \left(\frac{Z_2\cos\theta_i - Z_1\cos\theta_t}{Z_2\cos\theta_i + Z_1\cos\theta_t}\right)^2 \tag{2.17}$$

$$T_I = \frac{I_t}{I_i} = T^2\frac{Z_1}{Z_2} = \frac{4Z_1Z_2\cos^2\theta_i}{(Z_2\cos\theta_i + Z_1\cos\theta_t)^2} \tag{2.18}$$

where a planar reflecting surface larger than the insonated surface is assumed and I_i, I_r, and I_t are the acoustic intensities of the incident, reflected, and transmitted plane

waves at the material interface, respectively.

The concept of acoustic reflection highlights another notable challenge associated with TCD sonography. Using characteristic impedance values for cranial bone and soft tissue from Table 2.1 – and approximating the cranial bone surface near the transducer as planar – yields a transmissivity of $T_I = 0.76$ for normal incidence. This suggests a significant decrease in the acoustic power transmitted through the skull due solely to characteristic impedance mismatch, in addition to beam refraction and increased attenuation through bone. Degradation of acoustic intensity due to reflection is further exacerbated by the pulse-echo nature of sonography, where acoustic propagation to and returning from the cerebral vessels encounters four distinct interfaces between bone and soft tissue. Although the preceding analysis of intracranial applications is overly simplistic, neglecting the formation of standing wave patterns and the stratified internal structure of cranial bone, it illustrates a major limitation of transtemporal insonation and indicates a potential necessity for increased acoustic output power in TCD applications.

Reflection yields scattered wavefronts similar to the scatterer surface. For a spherical scatterer of diameter d_s, specular scattering occurs when $d_s \gg \frac{\lambda}{\pi}$ and results in a scattered spherical wave sector (i.e., spherical wave existing only for the sector defined by the insonated surface) as represented in Figure 2-2. A transmitted wave is also physically present, but not shown for clarity.

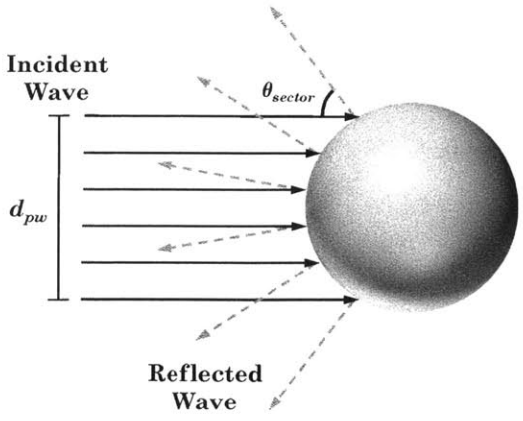

Figure 2-2: Specular scattering at a spherical scatterer.

In the specular regime, a plane wave – having a circular extent of diameter d_{pw} – normally incident on a spherical scatterer results in a reflected intensity characterized by the spherical reflectivity $\Gamma_{I,sphere}$ [40]:

$$\Gamma_{I,sphere}(r,\theta_r) = \frac{I_r(r,\theta_r)}{I_i} = \begin{cases} \frac{\Gamma^2 d_{pw}^2}{16r^2}, & |\theta_r| \leq \theta_{sector} \\ 0, & \text{otherwise} \end{cases} \tag{2.19}$$

where r is the distance from scatterer center to the point of observation, θ_r is the angle between plane wave incidence and the outward vector normal to the sphere surface (i.e., direction of reflected ray), and $2\theta_{sector}$ is the cone angle defining the insonated sphere surface.

Diffusive Scattering

In contrast to reflection, diffusive scattering – known also as Rayleigh scattering – occurs when scatterer dimensions are much smaller than acoustic wavelength. Rayleigh scattering is highly dependent on frequency, but ideally independent of scatterer shape and roughness features. For a spherical scatterer of diameter d_s, Rayleigh scattering occurs when $d_s \ll \frac{\lambda}{\pi}$ and results in the emission of an approximately spherical scattered wave.

For an individual scatterer, the differential scattering cross-section $\sigma_{ds}(\theta)$ defines the ratio of power scattered in a given direction $dp_s(\theta)$ to the differential solid angle $d\Omega$ and incident intensity I_i, where θ is the angle between the observation vector and the incident ray (i.e., z-axis in Figure 2-3). The differential scattering cross-section indicates the strength of scattering and is determined by both geometric (e.g., volume) and mechanical (e.g., density, compressibility) properties of the scatterer. Parameters relevant to the analysis of diffusive scattering are depicted in Figure 2-3.

$$\sigma_{ds}(\theta) = \frac{dp_s(\theta)}{d\Omega I_i} \tag{2.20}$$

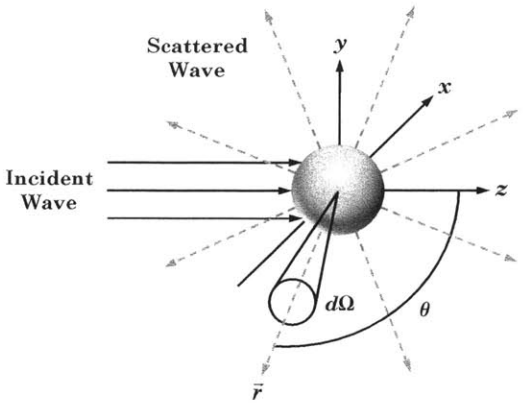

Figure 2-3: Diffusive scattering at a spherical scatterer.

For ideal diffusive scattering, the process is completely isotropic and $\sigma_{ds}(\theta)$ is constant across all angles, as expected for a spherical wave. In general, however, scattered intensity I_s from a single diffusive scatterer is dependent on both r and θ (neglecting attenuation effects):

$$\frac{I_s(r,\theta)}{I_i} = \frac{\sigma_{ds}(\theta)}{r^2} \tag{2.21}$$

Although diffusive scatterers cannot be individually resolved, scattering in this regime has important implications in sonography as tissue can often be modeled as an aggregate of sub-wavelength point scatterers. In medical Doppler ultrasound, diffusive scattering from blood is the fundamental mechanism that enables measurement of blood flow velocity. The evaluation of blood as a scatterer is therefore critically important for a realistic understanding of Doppler ultrasound functionality.

Blood is not a homogeneous liquid but rather a suspension of cells and other particles within plasma. Erythrocyte (i.e., red blood cells or RBCs) are flexible biconcave discs approximately 7 μm in diameter by 2 μm in thickness. Whole (i.e., unmodified) human blood contains approximately 5 million erythrocytes per microliter [40]. Erythrocytes make up roughly 45% of total blood volume, a value known as hematocrit (Ht). Scattering of ultrasound by blood is believed to be almost entirely due to erythrocytes [46]. Empirical measurements have established, however, that

physical scattering of blood and other tissue structures remains partially anisotropic, even within the diffusive scattering regime [47].

Neglecting structural complexities, a single erythrocyte can be accurately modeled as a spherical scatterer of equivalent volume, corresponding to a diameter of $\approx 6\,\mu$m. Considerable agreement between analytical and experimental results is achieved by representing the differential scattering cross-section of an erythrocyte as a function of angle between the incident ray and the observation vector (i.e., θ as shown in Figure 2-3) [42, 48].

$$\sigma_{ds}(\theta) = \frac{V_e^2 \pi^2}{\lambda^4} \left[\frac{\kappa_e - \kappa_f}{\kappa_f} + \frac{3(\rho_e - \rho_f)}{2\rho_e + \rho_f} \cos\theta \right]^2 \tag{2.22}$$

where V_e is erythrocyte volume, κ_e, ρ_e are erythrocyte compressibility and density, and κ_f, ρ_f are the compressibility and density of the surrounding fluid, respectively.

A scattered wave emanates from each erythrocyte within the region of insonation, yielding a Gaussian distribution of individual scattered wave intensities (I_s) that is therefore fully characterized by its mean and variance. This distribution arises mainly due to slight differences in the volume, compressibility, and density of each erythrocyte from the ensemble mean. In addition to amplitude deviations, every scattered waveform originates from an erythrocyte with a unique spatial position within the volume of insonation. Appreciable phase offsets between scatterers thereby results in interference between scattered wavefronts. The preceding effects lead to the formation of a complex speckle pattern that, although often characterized using statistical terms, is deterministically related to the underlying tissue microstructure and acoustic instrumentation characteristics. An equivalent speckle pattern will therefore be observed (in theory, when neglecting noise effects) when insonating a stationary tissue volume.

Diffusive scattering from a collection of point scatterers is characterized by the differential scattering coefficient $\mu_{ds}(\theta)$, which is the average power received from a volume of scatterers per steradian when insonified by a unit amplitude plane wave. The differential scattering coefficient – in the absence of multiple scattering – can

thereby be expressed as the accumulative contribution for all scatterers:

$$\mu_{ds}(\theta) = \left| \sum_i f_{ds}(\vec{r_i})\, \sigma_{ds,i}(\theta_i) \right| \tag{2.23}$$

where $f_{ds}(\vec{r_i})$ is a scaling function between -1 and 1 accounting for position (i.e., $\vec{r_i}$) dependent phase interference effects and $\sigma_{ds,i}$ is the differential scattering cross-section of an individual scatterer.

The nature of blood scattering, as evidenced in Equation 2.22, contains both isotropic (due to compressibility variation) and anisotropic (due to density variation) scattering contributions. A consequence of these combined scattering mechanisms is a degree of anisotropy that is dependent on tissue characteristics. For erythrocytes, the relative scattering coefficient is maximal for scattering toward the incident source (i.e., $\theta \approx \pi$) [42,47]:

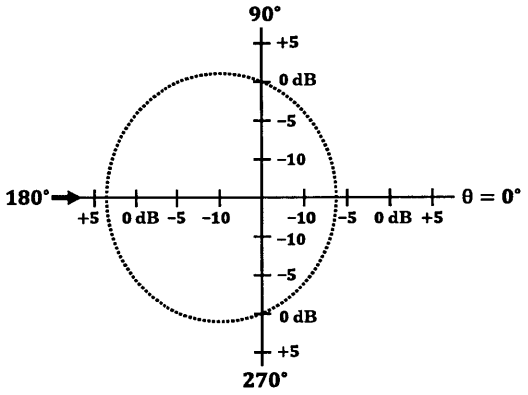

Figure 2-4: Differential scattering coefficient μ_{ds} angular dependence. Data from [42] at 6 MHz.

Because transmit and receive apertures are coincident in most modern ultrasound systems, the backscatter cross-section σ_{bs} and backscatter coefficient μ_{bs}, which characterize the power scattered in the direction of the incident source (i.e., $\theta = \pi$), are typically of primary importance.

$$\sigma_{bs} = \sigma_{ds}(\pi) \tag{2.24}$$

$$\mu_{bs} = \mu_{ds}(\pi) \tag{2.25}$$

The quartic dependence of the backscatter coefficient on frequency (recall $f \propto \frac{1}{\lambda}$), as suggested by Equation 2.22, has been verified experimentally for diluted human blood across a range of hematocrits as shown in Figure 2-5.

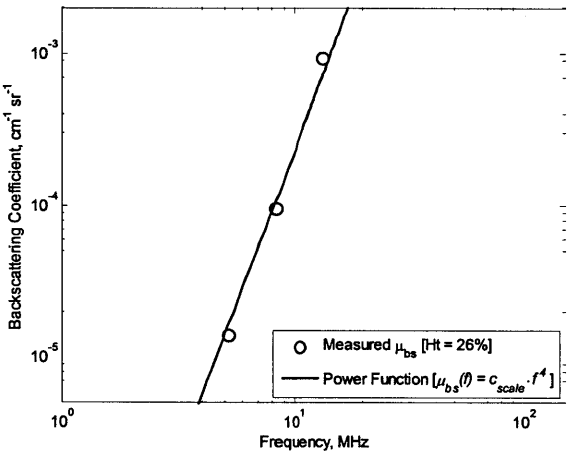

Figure 2-5: Erythrocyte backscatter coefficient μ_{bs} frequency dependence. Data from [49] for $Ht = 26\%$.

For media with no measureable spatial correlation in scattering properties, the scattering processing is incoherent and backscatter intensity is proportional to the number of insonated scatterers. At artificially low erythrocyte concentrations ($Ht < 8\%$), blood can be approximated as incoherent and the backscatter coefficient is approximately linearly proportional to the number of erythrocytes present within the volume of insonation [48]. At higher erythrocyte concentrations, the scattering process becomes exceedingly convoluted – likely resulting from multiple scattering effects and a progressive reduction in the incoherence of erythrocytes, which no longer behave as a random distribution of point scatterers. For *in vivo* erythrocyte concentrations (i.e, $Ht \approx 40 - 45\%$), the distance between scatterers becomes a modest fraction of erythrocyte diameter and therefore the position and motion of individual scatterers is highly dependent on surrounding erythrocytes [48].

The effect of hematocrit on the backscatter coefficient of human blood can be

expressed by the following empirical relationship [50]:

$$\mu_{bs} = \frac{Ht(1-Ht)^4}{(1+2Ht)^2}\frac{\sigma_{bs}}{V_e} \tag{2.26}$$

Experimental results for porcine erythrocyte suspensions of varied hematocrit, which have been shown to behave similarly to human erythrocytes, demonstrate reasonable agreement with the preceding analytical backscatter coefficient expression [50]. Maximal backscatter coefficient is achieved for hematocrit $\approx 14\%$.

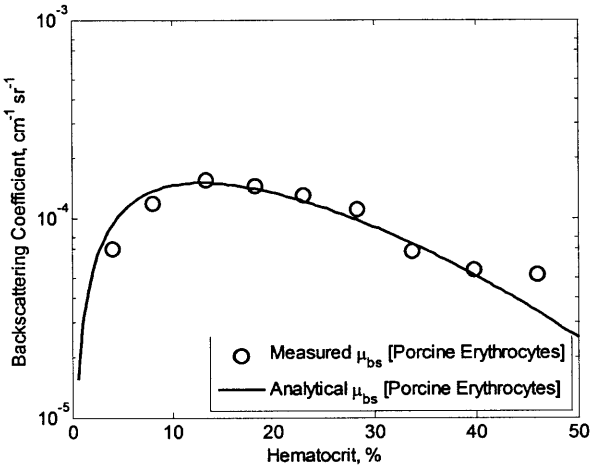

Figure 2-6: Porcine erythrocyte backscatter coefficient μ_{bs} hematocrit dependence under laminar flow. Data from [50] at 7.5 MHz

Under low shear rates, blood has a tendency to aggregate due to the presence of certain macromolecules within plasma (e.g., fibrinogen) [51]. The aggregation of erythrocytes into multi-cellular structures, known as rouleaux, significantly raises backscatter intensity (according to $\sigma_{ds} \propto V_e^2$), further increases the degree of scattering anisotropy, and potentially yields scatterer dimensions outside the diffusive regime. Experimental results from stationary blood yield backscatter intensities a factor of ten or more greater than from laminar flow measurements [50]. Because scattering is shear rate dependent, backscatter intensity is thereby a function of flow rate and the spatial position of erythrocytes within the vessel. For arterial blood flow, sufficiently high shear rates tend to disrupt aggregation such that erythrocytes are

primarily monodispersed [48]. Increased echogenicity has, however, been observed in venous blood due to erythrocyte aggregation. Turbulent flow has also been shown to considerably increase backscatter intensity, although the exact mechanism is not fully understood [52].

In practice, most insonation volumes for blood flow velocity estimation contain both erythrocytes and stationary tissue scatterers, which can have a substantial effect on the accuracy of Doppler ultrasound. For a given volume, stationary tissues (e.g., vascular wall structure) typically yield a substantial increase – by a factor of one to three orders of magnitude – in backscatter intensity when compared to erythrocyte scattering alone [43]. Although scattered power from stationary tissues, often referred to as clutter, can be highly attenuated via high pass filtering during Doppler signal processing, the increased signal levels place considerable constraints on system dynamic range, clutter filter complexity, and transducer beamwidth to ensure functional Doppler operation.

Diffractive Scattering

For scatterers with intermediate dimensions ($l_s \approx \frac{\lambda}{\pi}$), a process known as diffractive scattering occurs. Diffractive scattering is observed in TCD sonography for cerebral emboli, which are $\approx 0.5 - 3$ mm in maximum dimension (recall that $\lambda \approx 0.77$ mm for 2 MHz acoustic vibrations in tissue) [53]. The presence of a circulating gaseous or solid embolus within the region of insonation results in increased Doppler (i.e., non-stationary) backscatter power when compared to erythrocyte scattering alone. Embolus detection is thereby attained when backscatter power transiently increases beyond a given threshold (typically ≥ 7 dB) above the average background level [12].

In the diffractive regime, scattered waves can, to first order, be considered to originate from scatterer surfaces, which act as secondary sources [40]. In general, the shape of scattered waves is not, however, similar to media boundaries and is instead highly dependent on the relationship between scatterer dimensions and acoustic wavelength. The Born approximation can be used to obtain the differential scattering

cross-section for a spherical diffractive scatterer $\sigma_{ds,sphere}(\theta)$ [40,47]:

$$\sigma_{ds,sphere}(\theta) = \left\{ \frac{\lambda}{16\pi \sin^3(\theta/2)} \left[\gamma_\kappa + \gamma_\rho \cos\theta\right] \left[\sin\left(\frac{d_s}{2\lambda_s}\right) - \frac{d_s}{2\lambda_s} \cos\left(\frac{d_s}{2\lambda_s}\right) \right] \right\}^2 \tag{2.27}$$

where $\lambda_s = \frac{\lambda}{4\pi sin\left(\frac{\theta}{2}\right)}$, $\gamma_\kappa = \frac{\kappa_e - \kappa_f}{\kappa_f}$, $\gamma_\rho = \frac{\rho_e - \rho_f}{\rho_e}$, and the relevant geometry is equivalent to that shown in Figure 2-3.

2.1.2 Tissue Inhomogeneities

The presence of rigid cranial bone between the ultrasonic transducer and cerebral arteries of interest has profound effects on the performance and operation of TCD ultrasound systems. Although soft tissue can be approximated as a fluid acoustic medium, transmission through bone further complicates propagation. In general, a longitudinal wave incident on the surface of bone, or any elastic solid, creates both longitudinal and shear transmitted waves [54]. Mode conversion is, however, highly dependent on the angle of incidence and numerical studies suggest that shear wave generation can be effectively neglected for the small incidence angles typically encountered in TCD evaluations ($\theta_i < 20°$) [55,56].

Transmission through bone leads to several other significant phenomena. The large difference in phase velocities between bone and soft tissue creates refraction in acoustic wave transmissions, which can substantially alter transducer beam patterns [35]. As discussed previously, the large mismatch in characteristic acoustic impedance at the interface between bone and soft tissue yields considerable reductions in transmitted wave intensity due to reflection effects. Also, cranial bone is an extremely absorptive medium and its high attenuation factor further decreases wave intensity during propagation through the skull. The extent to which these preceding mechanisms influence acoustic propagation primarily determines the patency of acoustic windows (i.e., whether or not a receive Doppler signal is detectable) in patients undergoing TCD evaluation.

A detailed numerical analysis of acoustic wave propagation through realistic cranial geometries would yield marginal insight into the various design considerations

associated with the development TCD instrumentation. Such an approach also provides limited appreciation of effects due to anatomical disparities across the patient population. This work therefore incorporates basic homogeneous propagation models to guide system design choices. Experimental data from *ex vivo* cranial bone is utilized to evaluate the salient features of tissue inhomogeneities, which are treated primarily as simple attenuative elements (see Section 3.1.2).

2.2 Ultrasound Transducer Characterization

Transducer geometry and electromechanical properties are a critical design aspect of ultrasound systems and are highly dependent on application requirements. TCD ultrasound systems often employ a single manually steered circular transducer element, although imaging capable TCD systems (i.e., transcranial color-coded duplex sonography, referred to as TCCS) require transducer arrays for electronic beam steering. The single element transducer will be considered first, due to its relative simplicity. Results from this basic analysis will subsequently be used to characterize transducer arrays.

At the most fundamental level, an ultrasonic transducer simply converts energy between the electrical and acoustic (i.e., mechanical) domains. Subtleties related to this conversion process, however, have an enormous impact on system performance and functionality. The ultimate axial and lateral resolution of ultrasound instrumentation is determined by the electrical excitation, geometric, and material properties of the transducer. Transducer elements are traditionally fabricated from a variety of piezoelectric materials, including lead zirconate titanate (referred to as PZT), modified lead titanate ($PbTiO_3$), and PZT 1-3 composites [42, 57]. Developments in emerging non-piezoelectric transducer technologies, such as capacitive micromachined ultrasonic transducers (CMUTs), have shown promise in achieving high channel count integration with front-end electronics at potentially greatly reduced unit costs [58]. Irrespective of their underlying technology, transducers should be evaluated by a consistent set of performance metrics (e.g., bandwidth, efficiency, beam pattern for-

mation). The physical dimensions and equivalent circuit models used in this work, however, imply piezoelectric construction.

2.2.1 Transducer Impulse Response and Quality Factor

For acoustic transmission, an electrical signal (typically a driven voltage, which will be assumed throughout this work) at the electrical port of the transducer induces acoustic vibrations at the front and back surfaces of the transducer. The relationship between the electrical driving signal and the transducer front surface velocity $u(t)$ is characterized by the electroacoustic conversion impulse response $g_T(t)$ of the transducer [40]. A notional transducer electroacoustic conversion impulse response is shown in Figure 2-7.

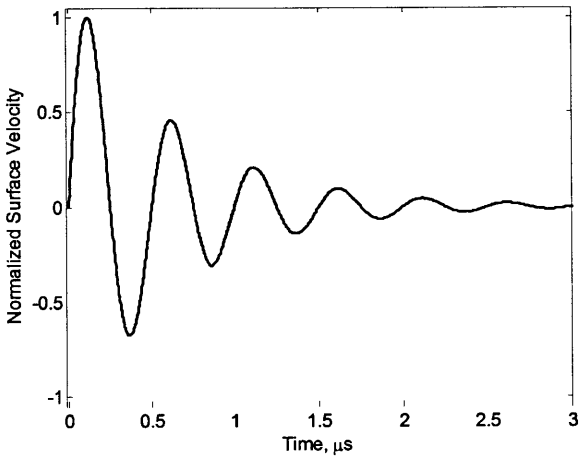

Figure 2-7: Transmit electroacoustic conversion impulse response of a 2 MHz transducer with a quality factor of 4.

It is important to note that $g_T(t)$ is not constant for a specific physical transducer geometry, but is instead highly dependent on the load impedance at each port. In most cases of interest for medical ultrasound, the front transducer surface is loaded by acoustic matching layers constructed within the element housing (to reduce impedance mismatch effects) and soft tissue, while the back transducer surface is loaded by air or a fixed backing material. Because the acoustic properties of soft tissue are fairly constant and the back transducer surface is embedded within

the element case, loading and therefore transducer characteristics are assumed to be effectively constant for a given transducer element over all relevant circumstances.

A primary characteristic of the electroacoustic conversion impulse response is transducer quality factor (Q), defined as:

$$Q = 2\pi \frac{\text{energy stored}}{\text{energy lost per cycle}} \tag{2.28}$$

Quality factor is inversely related to the impulse response decay constant through the relation [44]:

$$\text{Env}\left\{g_T\left(t\right)\right\} = u_0 e^{\frac{-f_0 \pi t}{Q}} \tag{2.29}$$

where Env $\{\cdot\}$ denotes the envelope function, u_0 is a velocity scaling factor, and f_0 is the resonant frequency transducer.

The transducer frequency response is computed as the Fourier transform of $g_T\left(t\right)$. For a given half-power bandwidth (Δf), the quality factor of the transducer is determined by:

$$Q = \frac{f_0}{\Delta f} \tag{2.30}$$

The range of suitable transducer quality factors is dependent on desired application. Axial resolution (AR) represents the ability of an ultrasound instrument to differentiate closely spaced scatterers in the axial dimension (i.e., depth). For imaging purposes, low axial resolution is desired for improved image resolution. Both transducer quality factor and the excitation waveform influence axial resolution, with minimal axial resolution AR_{min} occurring for impulse excitations [44]. The quality factor of a transducer used for imaging is often intentionally lowered by placing ultrasound absorber at the back transducer surface to introduce additional losses. Doppler applications, in contrast, do not require fine axial resolution and therefore can use higher Q transducers, which yield increased transducer efficiency.

$$AR_{\text{min}} \approx \frac{Q\lambda}{4} \tag{2.31}$$

In practice, second order effects such as frequency dependent tissue absorption, known

as dispersive absorption, effectively lengthen the pulse and result in larger axial resolutions than analytically predicted.

2.2.2 Transducer Excitation

Electrical transducer driving signals fall under two general classes, continuous wave (CW) and pulsed wave (PW) excitations. Ultrasound imaging systems operate solely in the PW regime due to spatial resolution requirements. Doppler ultrasound instrumentation, however, can employ CW or PW excitations. Although CW operation is less common in modern ultrasound systems, continuous analysis is relatively straightforward and often yields significant insight into PW functionality.

For CW excitation, the transducer is driven by a periodic waveform $e_{T,CW}(t)$ – typically a sinusoid or square wave – with an excitation frequency f_e at or near the resonant frequency of the transducer (f_0).

$$e_{T,CW}(t) = e_{periodic}(t, T_e) \tag{2.32}$$

where $T_e = \frac{1}{f_e}$ is the fundamental period of $e_{periodic}(t, T_e)$, such that $e_{periodic}(t, T_e) = e_{periodic}(t + T_e, T_e)\ \forall t$.

PW excitation employs a gated periodic function to drive the transducer. The basis function of pulsed excitation $e_{T0}(t)$ can be expressed as:

$$e_{T0}(t) = \prod\left(\frac{t}{T_e M} - \frac{1}{2}\right) e_{periodic}(t, T_e) \tag{2.33}$$

where M is the number of cycles (of period T_e) within a single gate and the gating function $\prod\left(\frac{t-t_{shift}}{t_{ON}} - \frac{1}{2}\right)$ is a shifted, time-scaled rect function with interval $[t_{shift}, t_{shift+t_{ON}}]$, written as:

$$\prod\left(\frac{t - t_{shift}}{t_{ON}} - \frac{1}{2}\right) = \begin{cases} 1, & t_{shift} \leq t \leq t_{shift} + t_{ON} \\ 0, & \text{otherwise} \end{cases} \tag{2.34}$$

The basis function $e_{T0}(t)$ can therefore be alternately expressed as:

$$e_{T0}(t) = \prod\left(\frac{t}{T_e M} - \frac{1}{2}\right) e_{periodic}(t, T_e) = \begin{cases} e_{periodic}(t, T_e), & 0 \leq t \leq T_e M \\ 0, & \text{otherwise} \end{cases} \tag{2.35}$$

Because PW excitations typically are used to drive transducers with high fractional bandwidths (> 50%), the periodic excitation frequency f_e does not necessarily need to be near the resonant frequency of the transducer f_0, but within the transducer bandwidth (i.e., $f_0 \pm \frac{\Delta f}{2}$).

The PW driving waveform can then be synthesized as a combination of time-shifted basis functions:

$$e_{T,PW}(t) = \sum_{n=0}^{\infty} e_{T0}(t - nT_{PRP}) \tag{2.36}$$

where n corresponds to the pulse repetition number and T_{PRP} is the pulse repetition period. Another meaningful parameter often used to characterize pulsed operation is the pulse repetition frequency $f_{PRF} = 1/T_{PRP}$.

A notional PW excitation waveform is shown in Figure 2-8.

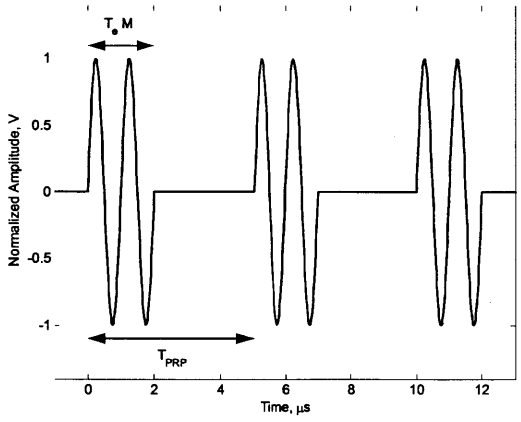

Figure 2-8: Pulsed wave excitation waveform for $M = 2$, $T_e = 1.0\mu s$, and $T_{PRP} = 5\mu s$.

Note that an artificially low T_{PRP} is used for illustration clarity. A realistic pulse repetition period is typically $T_{PRP} \approx 0.1 - 0.2$ ms for medical ultrasound applications.

2.2.3 Equivalent Circuit Transducer Model

Although useful for a basic understanding of transducer operation, the preceding analysis is often overly simplistic in assuming a second-order transducer model. Transducer characteristics – for a dominant resonant mode – can be well described by an equivalent circuit model. Transducer circuit models are useful for simulated verification of electronic hardware within the ultrasound system under realistic loading conditions. The KLM model, developed by Krimholtz, Leedom, and Matthaei, is often used in the design and characterization of ultrasound transducers and is depicted in Figure 2-9.

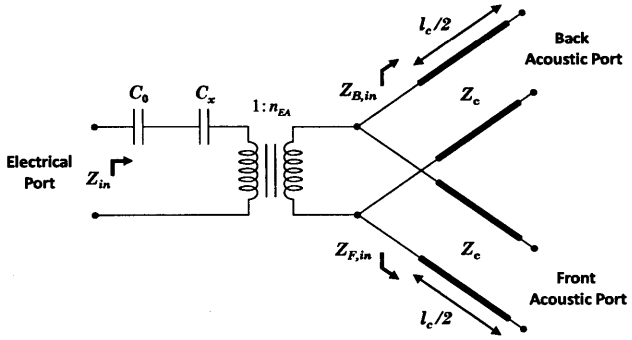

Figure 2-9: KLM equivalent circuit transducer model. Adapted from [59]

In the KLM model, an electrical port is coupled to the acoustic domain at the center junction of the resonant transducer dimension (l_c) through a transformer, with electroacoustic transformer ratio n_{ea}. The piezoelectric crystal is modeled by transmission lines of length $l_c/2$, phase velocity c_c, and specific acoustic impedance $Z_c = A_c\rho_c c_c$. Note that the specific acoustic impedance differs from characteristic acoustic impedance in that it accounts for the cross-sectional area (A_c) of the piezoelectric crystal. The front acoustic port is connected to an impedance defined by matching layers and soft tissue, while the back acoustic port is often connected to a backing material.

Resonance occurs when the resonant transducer dimension l_c is odd multiples of $\lambda/2$. The fundamental transducer resonant frequency can therefore be expressed as $f_0 = c_c/2l_c$. It is critical that the resonant dimension l_c is sufficiently different from

other transducer dimensions, such that multi-resonant effects can be neglected and the equivalent KLM model remains valid. Further expansion of the KLM model for various transducer geometries and physical insight into its lumped element parameters can be found in [40]. Although individual elements within the KLM model can be derived from mechanical principles, higher-order effects – especially for array element geometries – often greatly degrade the integrity of analytical models. Numerical methods, such as finite element analysis (FEA), are therefore generally used to accurately determine transducer response and extract equivalent model parameters.

The previous analysis has focused on utilizing the transducer for acoustic transmission (i.e., transforming electrical energy to mechanical energy). Due to the reciprocity principle, the equivalent circuit models used to characterize acoustic transmission are also valid for electrical reception (i.e., transforming mechanical energy into electrical energy). Formally, a transducer represented as an ABCD matrix with an input at the electrical port is described by a DCBA matrix with an input at the acoustic port [40].

2.2.4 Continuous Transducer Beam Patterns

The beam pattern of a rigidly mounted transducer radiating into a homogeneous fluid can be found by dividing the transducer surface into a collection of infinitesimal radiators of surface area dS. This framework is presented in Figure 2-10 and, although illustrated for a circular transducer, is valid for any arbitrary planar transducer surface.

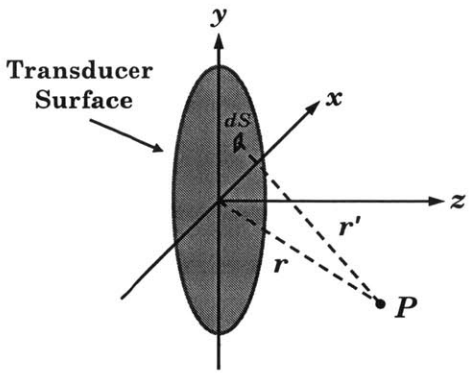

Figure 2-10: Coordinate system for analysis of planar transducer beam patterns.

For a transducer surface vibrating uniformly with velocity $u(t) = u_0 \cos(2\pi f t)$ normal to the surface (i.e., along the z-axis in Figure 2-10), the pressure contribution dp from each infinitesimal radiator, neglecting attenuative losses, is given as [44]:

$$dp = \frac{u_0 Z}{\lambda r'} \cos\left(2\pi f t - kr' + \frac{\pi}{2}\right) dS \tag{2.37}$$

where r' is the distance from the elemental radiator to the observation point P. Note that because a single harmonic velocity waveform is used, CW excitation is implied. Due to their relative amenability, transducer radiation patterns will first be developed for continuous excitations and will then be extended into pulsed fields. Although pulsed operation yields excitation dependent beam patterns, CW analysis can provide a practical starting point for transducer design since general approximate relationships between aperture dimensions and energy boundaries typically persist in the PW regime.

Using Huygens' principle, the resultant pressure field from a transducer surface is evaluated by the superposition of spherical waves from each radiator.

$$p(\vec{r}, t) = \int_S dp = \frac{u_0 Z}{\lambda} \int_S \frac{\cos\left(2\pi f t - kr' + \frac{\pi}{2}\right)}{r'} dS \tag{2.38}$$

where S denotes the transducer surface. The preceding expression, known as the Rayleigh integral for continuous wave excitation, does not yield a general solution and often must be solved numerically.

For unfocused planar transducers, the progression from the near-field (i.e., Fresnel region) to the far-field (i.e., Fraunhofer region) occurs at the transition distance z_r, referred to as the natural focus of the transducer [44].

$$z_r = \frac{\max\{l_t\}^2}{4\lambda} \tag{2.39}$$

where $\max\{l_t\}$ is the largest dimension of the transducer surface (e.g., diameter of a circular transducer).

Circular Transducer

Due to symmetry, the pressure field of a circular transducer for observation points along the axial dimension (i.e., z-axis) can be found analytically as [44]:

$$p(z,t) = Zu_0 \left[\cos(2\pi ft - kz) - \cos\left(2\pi ft - k\sqrt{\frac{D^2}{4} + z^2} \right) \right] \tag{2.40}$$

where D is transducer diameter.

Obtaining the envelope of the preceding spatiotemporal function yields a more useful representation of pressure variation [40]:

$$p_{env}(z) = 2Zu_0 \left| \sin\left\{ \frac{\pi z}{\lambda} \left[\sqrt{1 + \left(\frac{D}{2z} \right)^2} - 1 \right] \right\} \right| \tag{2.41}$$

For circular transducers, the depth of the last axial maximum (z_{lam}) is equal to the transition distance (z_r) and is therefore the boundary between near-field and far-field. For non-planar radiating surfaces and transducers without radial symmetry (e.g., rectangular sources), however, the value of z_lam is less meaningful.

As shown in Figure 2-11, the pressure envelope of a circular transducer varies dramatically in the near-field. These pressure irregularities are produced by constructive and destructive interference between spherical wavefronts originating from distinct spatial positions on the transducer surface. Beyond the transition distance z_r, the phase difference between individual wavefronts is no longer sufficient to achieve maximal destructive interference and axial pressure variation is thereby substantially reduced.

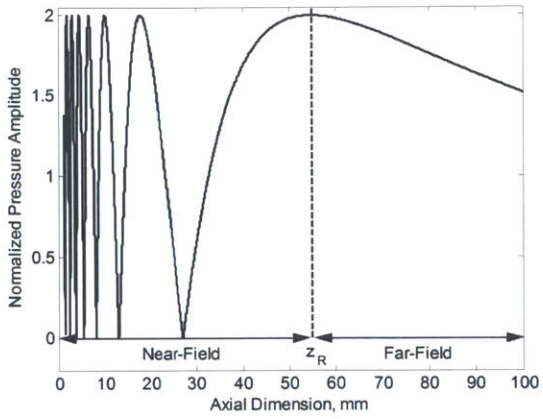

Figure 2-11: Analytical variation of on-axis pressure envelope for a 13 mm diameter circular transducer operating at 2 MHz. Values are normalized to the pressure magnitude at the transducer surface.

The off-axis beam pattern of a circular transducer cannot be expressed analytically for the near-field, but is readily computed using an acoustic field solver, as shown in Figure 2-12 [38, 39]. Field solvers can also incorporate attenuation effects, but such effects are neglected here to yield consistency with analytical models. Attenuation is not used when showing transducer beam patterns unless explicitly noted in this work.

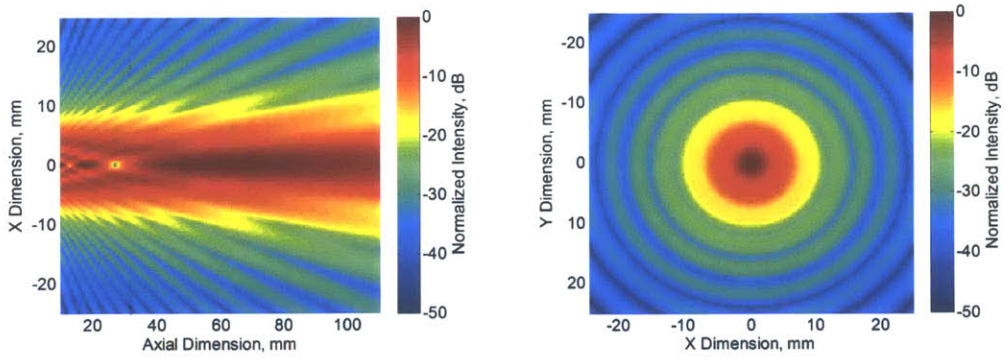

(a) Intensity variation in the xz-plane at $y = 0$ mm.

(b) Intensity variation in the xy-plane at $z = 60$ mm.

Figure 2-12: Simulated intensity beam pattern for a 13 mm diameter circular transducer operating at 2 MHz.

Rectangular Transducer

Beamformation for rectangular transducers is of particular interest for medical applications as they are commonly used in linear and phased arrays for imaging and Doppler applications. Unlike the circular transducer, the beam pattern of a rectangular transducer is determined by two orthogonal dimensions, transducer height (L_y) and width (L_x).

Under continuous excitation the pressure field envelope of a rectangular transducer for observation points along the axial dimension is expressed as [40]:

$$p_{env}(z) = \left| 2Zu_0 \mathrm{Im}\left\{ F\left(\frac{L_x}{\sqrt{2\lambda}}\right) F\left(\frac{L_y}{\sqrt{2\lambda}}\right) \right\} \right| \tag{2.42}$$

where $F(x)$ is the Fresnel integral, given by $F(x) = \int_0^x e^{-\jmath\pi t^2/2} dt$.

Due to diminished symmetry, modulation of the near-field pressure envelope is much less exaggerated for rectangular radiating surfaces than for circular transducers, as illustrated in Figure 2-13.

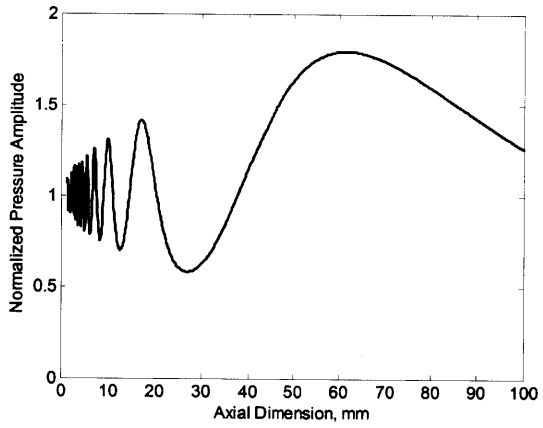

Figure 2-13: Analytical variation of on-axis pressure envelope for a rectangular transducer ($L_x = 12$ mm, $L_y = 12$ mm) operating at 2 MHz. Values are normalized to the pressure magnitude at the transducer surface.

Figure 2-14 characterizes the simulated single frequency beam pattern in a lossless, homogeneous medium for a rectangular transducer in the xy and xy-planes [38, 39].

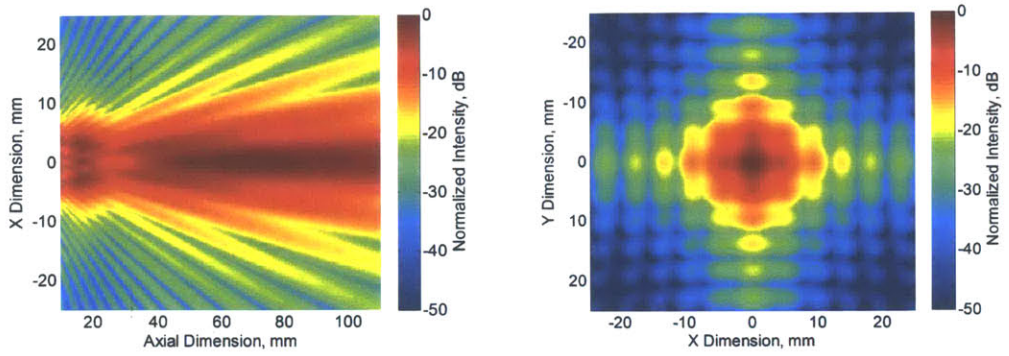

(a) Intensity variation in the xz-plane at $y = 0$ mm.

(b) Intensity variation in the xy-plane at $z = 60$ mm.

Figure 2-14: Simulated intensity beam pattern for a rectangular transducer ($L_x = 12$ mm, $L_y = 12$ mm) operating at 2 MHz.

2.2.5 Far-Field Transducer Beam Patterns

Within the near-field region of an unfocused transducer, acoustic energy is mostly confined to the transverse extent of the transducer. As the beam propagates into the far-field, a single main lobe is established and acoustic energy diverges transversely with a roughly constant angle, known as the divergence half-angle θ_d, as depicted in Figure 2-15.

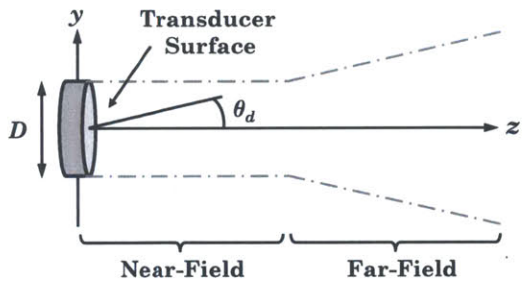

Figure 2-15: Approximate beam shape and far-field divergence for an unfocused transducer. Adapted from [44].

For observation points in the far-field of the transducer, the acoustic waveform is less irregular and the off-axis beam pattern can be expressed analytically for both circular and rectangular transducers.

Circular Transducer

Acoustic pressure in the far-field of a continuously driven circular transducer – with uniform surface velocity $u(t) = u_0 \cos(2\pi f t)$ – is expressed as [44]:

$$p(\theta, r, t) = \frac{kD^2 Z u_0}{4r} \cos\left(2\pi f t - kr + \frac{\pi}{2}\right) \left[\frac{2J_1\left(\frac{kD}{2}\sin\theta\right)}{\frac{kD}{2}\sin\theta}\right] \tag{2.43}$$

where $J_1(\cdot)$ denotes a Bessel function of the first kind with order one, D is the radiating surface diameter, and θ is the angle between the z-axis and the observation vector $\vec{r}$.

From Equation 2.43, the angular dependence of acoustic pressure is determined by the transducer directivity factor $H_c(\theta)$:

$$H_c(\theta) = \left|\frac{2J_1\left(\frac{kD}{2}\sin\theta\right)}{\frac{kD}{2}\sin\theta}\right| \tag{2.44}$$

For a given observation radius (i.e., fixed r), the directivity factor is often visually represented using a polar radiation plot, as shown in Figure 2-16.

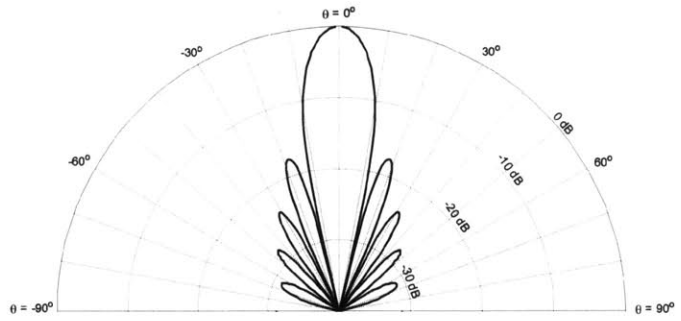

Figure 2-16: Analytical far-field directivity pattern for a 4 mm diameter circular transducer operating at 2 MHz.

The divergence angle $2\theta_d$ is defined as the angle between the first zeros of the main lobe and is expressed for a circular transducer as:

$$2\theta_d = 2\sin^{-1}\left(\frac{1.22\lambda}{D}\right) \tag{2.45}$$

The half-power angle ($2\theta_{3dB}$), known also as the angular full width to half maximum (FWHM), is defined as the angle between the half-power values of the main lobe. For a circular transducer, the half-power angle is expressed as:

$$2\theta_{3dB} = 2\sin^{-1}\left(\frac{0.51\lambda}{D}\right) \tag{2.46}$$

Within the far-field region, main lobe width increases linearly with axial distance. Full beamwidth $w(z)$ (i.e., lateral spatial extent of the main lobe) and half-power beamwidth $w_{3dB}(z)$ are therefore determined at a given far-field depth z as:

$$w(z) = 2z\tan(\theta_d) \tag{2.47}$$

$$w_{3dB}(z) = 2z\tan(\theta_{3dB}) \tag{2.48}$$

Rectangular Transducer

For a sinusoidally driven rectangular transducer – of width L_x and height L_y – acoustic pressure in the far-field is computed as [44]:

$$p(\phi_x, \phi_y, r, t) = \frac{L_x L_y k Z u_0}{2\pi r}\cos\left(2\pi f t - kr + \frac{\pi}{2}\right)\operatorname{sinc}\left(\frac{L_x k\sin\phi_x}{2\pi}\right)\operatorname{sinc}\left(\frac{L_y k\sin\phi_y}{2\pi}\right) \tag{2.49}$$

where the sinc function is defined as:

$$\operatorname{sinc}(x) = \frac{\sin(\pi x)}{\pi x} \tag{2.50}$$

As illustrated in Figure 2-17, the azimuth angle ϕ_x is the angle between the z-axis and the projection of $\vec{r}$ on the xz-plane. The elevation angle ϕ_y is the angle between the z-axis and the projection of $\vec{r}$ in the yz-plane.

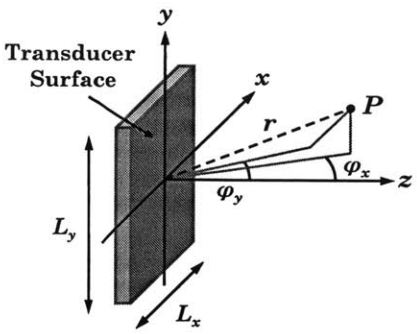

Figure 2-17: Coordinate system for analysis of planar rectangular transducer beam patterns.

The directivity factor of a rectangular transducer $H_r(\phi_x, \phi_y)$ is thereby dependent on directivity in two orthogonal planes, the xz-plane (i.e., azimuth plane) and the yz-plane (i.e., elevation plane):

$$H_r(\phi_x, \phi_y) = H_x H_y = \left|\text{sinc}\left(\frac{L_x k \sin\phi_x}{2\pi}\right)\right| \left|\text{sinc}\left(\frac{L_y k \sin\phi_y}{2\pi}\right)\right| \tag{2.51}$$

A polar directivity plot therefore exists for both the azimuth plane, primarily dependent on L_x dimension, and the elevation plane, primarily dependent on L_y dimension. Figure 2-18 shows the directivity of a square transducer element, which has an equivalent directivity pattern in both the azimuth (i.e., H_x) and elevation (i.e., H_y) planes due to transducer symmetry. The observed sidelobe levels for a rectangular transducer element are markedly higher than for a circular transducer of similar dimensions.

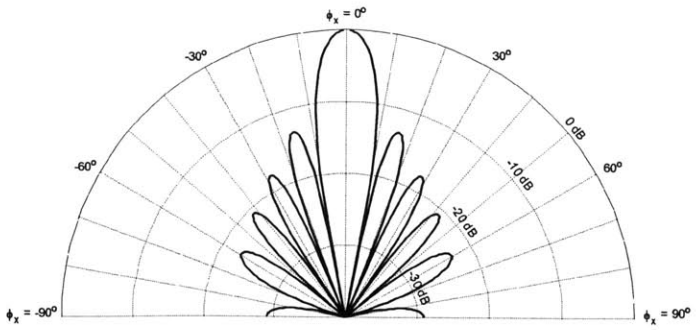

Figure 2-18: Analytical far-field directivity pattern in the azimuth plane for rectangular transducer ($L_x = 4$ mm, $L_y = 4$ mm) operating at 2 MHz.

As in the circular transducer case, the divergence angle ($2\theta_d$) and half-power angle ($2\theta_{3dB}$) can be defined from the main lobe characteristics. For the rectangular transducer, however, these parameters exist for both orthogonal directivity planes.

$$2\theta_{x,d} = 2\sin^{-1}\left(\frac{\lambda}{L_x}\right), \quad 2\theta_{y,d} = 2\sin^{-1}\left(\frac{\lambda}{L_y}\right) \tag{2.52}$$

$$2\theta_{x,3dB} = 2\sin^{-1}\left(\frac{0.44\lambda}{L_x}\right), \quad 2\theta_{y,3dB} = 2\sin^{-1}\left(\frac{0.44\lambda}{L_y}\right) \tag{2.53}$$

Full beamwidth $w(z)$ and half-power beamwidth $w_{3dB}(z)$ can be computed for a given far-field depth z:

$$w_x(z) = 2z\tan(\theta_{x,d}), \quad w_y(z) = 2z\tan(\theta_{y,d}) \tag{2.54}$$

$$w_{x,3dB}(z) = 2z\tan(\theta_{x,3dB}), \quad w_{y,3dB}(z) = 2z\tan(\theta_{y,3dB}) \tag{2.55}$$

Arbitrary Planar Transducer

For elements with aperture dimensions on the order of a wavelength, the directivity pattern can be approximated by the inverse Fourier transform of the spatial aperture functions in each transducer dimension [40].

$$H(x,y,z) \approx \int_{-\infty}^{+\infty} A_x(x_0)\, e^{j2\pi x_0(x/\lambda z)} dx_0 \int_{-\infty}^{+\infty} A_y(y_0)\, e^{j2\pi y_0(y/\lambda z)} dy_0 \tag{2.56}$$

where $A_x(x)$ and $A_y(y)$ are the aperture functions of the transducer element in the x and y dimensions.

For a rectangular element, the aperture function is simply a scaled rect function:

$$A_x(x) = \prod(x/L_x), \quad A_y(y) = \prod(y/L_y) \tag{2.57}$$

2.2.6 Transducer Arrays

Transducer arrays are found in the majority of modern ultrasound imaging systems. Although most array transducers are one-dimensional (1D) arrays, advances in transducer fabrication and electronic interconnects have greatly facilitated the development of two-dimensional (2D) transducer arrays. The intention of this work is to utilize electronic steering of acoustic energy to accurately locate a specific cerebral vessel (i.e., MCA) within a designated spatial volume. This task necessitates the use of a 2D transducer array, which will therefore be examined specifically.

A piezoelectric transducer matrix is typically composed of rectangular radiating elements spatially offset by the element pitch in each dimension (pitch_x and pitch_y), as shown in Figure 2-19. Other parameters relevant to the array geometry are the lateral dimensions of individual elements (L_x and L_y), the number of elements along each dimension (N_x and N_y), and the spacing between adjacent element edges (kerf_x and kerf_y).

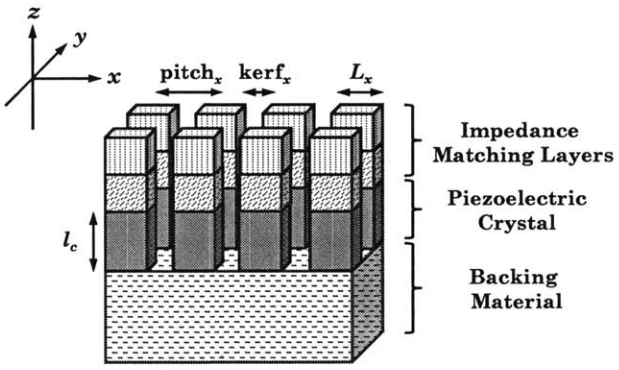

Figure 2-19: Configuration of partial 2D transducer array structure.

Ultrasound arrays are configured into two basic functional modes, linear operation and phased array operation, as depicted in Figure 2-20.

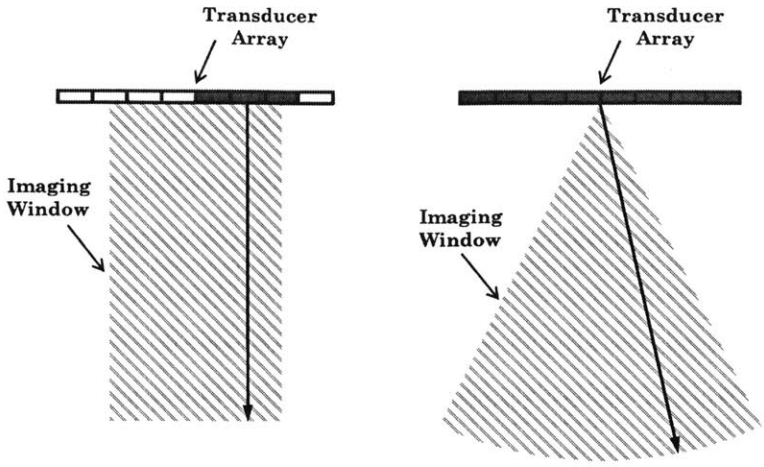

(a) Linear operation of 1D transducer array.

(b) Phased array operation of 1D transducer array.

Figure 2-20: Basic transducer array operating modes. Adapted from [42].

Linear operation utilizes a limited subset of transducer elements during each pulse emission, with adjacent element groups excited sequentially, to achieve lateral resolution. Because only a limited number of elements are employed simultaneously in linear operation, total acoustic output power is markedly reduced for a given excitation amplitude. For TCD applications, however, the presence of cranial bone leads to significantly increased acoustic output power requirements. Also, beam focusing capabilities are severely degraded for linear operation due to a reduced instantaneous aperture, thus additionally decreasing the acoustic pressure attainable within the region of interest. Linear array excitation is therefore not suitable for transcranial velocimetry measurements and will not be considered further.

To first order, a 2D phased array can be estimated as an equivalent mechanically steered solid aperture with variable focal length. The effective dimensions of this equivalent aperture are approximated as $L_{x,eq} \approx N_x \cdot \text{pitch}_x$ and $L_{y,eq} \approx N_y \cdot \text{pitch}_y$. This analogy is overly simplistic in that electronic steering of the phased array can create focal patterns that are not physically realizable in a focused element. Also, additional complexities are observed in the phased array beam pattern due to the

segmentation of the transducer surface into array elements.

Unlike single element transducers, array apertures are formed electronically through delay mechanisms rather than by physical form. Such electrically defined apertures are advantageous in that both transmit and receive apertures can be defined independently, aperture characteristics (e.g., steering angle, focal region) can be directly altered, and – for certain system architectures – multiple receive apertures can be defined post hoc via post-processing. For TCD applications, the ability to rapidly steer electronically facilitates the development of vessel location and tracking algorithms. Additionally, utilization of multiple receive beams enables simultaneous velocimetry measurement and uninterrupted vessel tracking throughout the evaluation period.

A transducer array cannot be accurately analyzed as a coherent set of infinitesimal isotropic radiators, as is done for a single element transducer. Instead, the transducer array is a collection of individual radiating elements with appreciable dimensions, relative to λ, and therefore an anisotropic directivity pattern. The beam pattern of a phased array is dependent on both the relative excitation delay between elements and the radiation pattern of the elements themselves. Figure 2-21 presents the beam patterns of two square array elements with dimensions on the order of λ (i.e., 0.5mm = 0.65λ and 1.2mm = 1.6λ for 2 MHz acoustic vibrations in soft tissue).

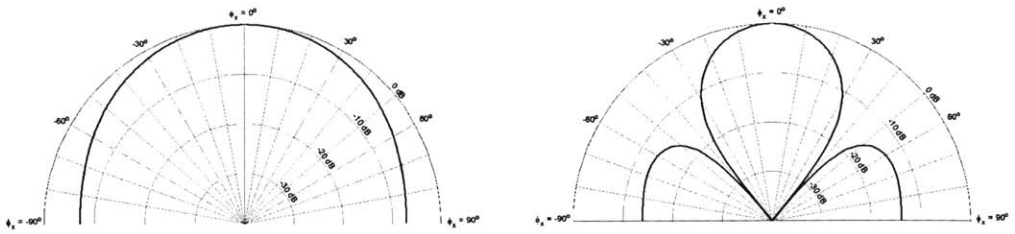

(a) Intensity variation for element with dimensions $L_x = 0.5$ mm, $L_y = 0.5$ mm.

(b) Intensity variation for element with dimensions $L_x = 1.2$ mm, $L_y = 1.2$ mm.

Figure 2-21: Analytical far-field directivity pattern in the azimuth plane for a square array element operating at 2 MHz.

Although smaller element dimensions yield more favorable element directivity patterns (i.e., approaching isotropic), practical transducer array designs introduce several

conflicting aims. As described in Section 2.2.8, the equivalent aperture dimensions of a transducer array must increase when focusing is required at greater tissue depths.

As individual element dimensions decrease, the total number of elements required to obtain a given aperture area rises quadratically. The corresponding addition of electrical hardware and element interconnects leads to greater fabrication difficulty, system complexity, cost, and power dissipation. However, as transducer element dimensions increase – especially greater than λ – the range of realizable steering angles for the phased array system is limited due to element directivity effects.

Due to the discrete structure of a transducer array, a variety of secondary factors – including element variation, cross coupling between elements, time delay quantization, and apodization amplitude quantization – can influence beam pattern formation. Quantization effects, which tend to predominately affect sidelobe levels, are tolerable in most applications for quantization errors $< 10\%$ of the underlying signal period (i.e., T_e) and can be readily assessed using acoustic field solvers [60]. The result of element variation and electromagnetic cross coupling between elements, however, is typically assessed using multiphysics FEA or, more practically, through experimental acoustic field characterization.

An added complexity related to the radiation pattern of transducer arrays is the emergence of grating lobes. Grating lobes occur at specific angles in which acoustic waves emerging from two neighboring elements are exactly in phase for a certain angle (referred to as the grating angle), creating constructive interference and substantial acoustic intensity outside the main beam. In ultrasound imaging, the presence of grating lobes leads to confounding receive echoes since acoustic energy is no longer confined along the main beam direction. The presence of grating lobes can also degrade Doppler ultrasound measurements, even when no appreciable flow exists within grating lobes, by markedly increasing stationary backscattered power and thereby degrading the minimum detectable signal for a given system dynamic range. Grating lobes are typically stronger than sidelobes and can yield intensities on the order of main lobe intensities. The grating angle differs for both the azimuth and elevation

planes and is given by:

$$\phi_{x,gn} = \sin^{-1}\left(\frac{n\lambda}{\text{pitch}_x}\right) \tag{2.58}$$

$$\theta_{y,gn} = \sin^{-1}\left(\frac{n\lambda}{\text{pitch}_y}\right) \tag{2.59}$$

where n is an integer value, although typically the fundamental (i.e., $n = 1$) is of primary interest. Solutions resulting in $|\phi_{x,gn}| > 90°$ or $|\theta_{y,gn}| > 90°$ are non-physical and therefore invalid.

To avoid grating lobe formation, element pitch must satisfy the following conditions:

$$\text{pitch}_x < \frac{\lambda_{\text{min}}}{2},\ \text{pitch}_y < \frac{\lambda_{\text{min}}}{2} \tag{2.60}$$

where, due to an inverse relationship between wavelength and frequency, λ_{min} corresponds to the highest frequency component in the emitted signal. The preceding inequality can be viewed as a consequence of the Nyquist sampling theorem in the spatial domain, where the presence of grating lobes are an indication spatial aliasing. Grating lobe effects can be reduced through PW excitation and for angles ϕ_{gn} that occur beyond the element directivity main lobe.

As observed for element directivity, grating lobe limitations can lead to element sizing that results in an impractical number of elements for the aperture dimensions required. Ultrasound system architectures must therefore balance the conflicting objectives of performance and complexity in consideration of target applications.

2.2.7 Apodization

Amplitude weighting across an acoustic aperture is known as apodization. Apodization can be achieved during acoustic transmission via radially non-uniform single element transducer structures or, in transducer arrays, through scaled driving voltages and scaled receiver gains for individual transducer elements. Single element transducers attain equivalent apodization during signal reception due to transducer reciprocity. Because apodization mechanisms differ on transmit and receive for transducer arrays, apodization of the transmit and receive apertures is independent. Recognition that

a Fourier relationship exists between spatial aperture geometries and their far-field directivity patterns is essential in understanding the objective of apodization. As observed for the far-field beam pattern of a rectangular transducer element in Equation 2.49, the rect and sinc functions form a Fourier transform pair.

Sidelobes are local maxima of the far-field directivity pattern outside the main lobe. The presence of sidelobes in a transducer beam pattern can interfere with the assessment of tissue structures within the main beam, especially when a strong reflector is located within the sidelobe. Although similar in effect to grating lobes, sidelobes are a distinct phenomena, occurring in both single element and transducer arrays, and are a resulting function of the total equivalent transducer aperture.

A rectangular aperture is particularly unfavorable for low sidelobe beamformation as its first sidelobe is only 13 dB below main lobe intensity. Using insights from Fourier analysis, applying an acceptable weighting function to the rectangular aperture will significantly suppress sidelobe levels. As presented in Figure 2-22, applying a Hamming weighting function to the rectangular aperture results in a drastic decrease in peak sidelobe level from -13 dB to -42 dB, relative to main lobe intensity [61]. The use of apodization is not, however, without inherent limitations. For Hamming weighted apertures, a reduction in main lobe acoustic power (by a factor of ≈ 5) and significant broadening of main lobe beamwidth (by a factor of ≈ 2) are observed. Both effects are in most applications undesirable, but not necessarily unacceptable and are encountered, to some degree, in all apodization weighting functions.

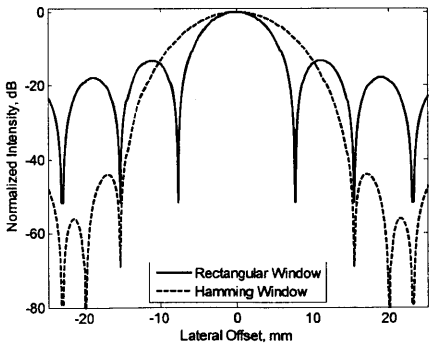

Figure 2-22: Effect of aperture apodization on normalized acoustic intensity.

2.2.8 Focused Transducers

Acoustic focusing, which converges a radiating beam into a spot at the focal plane, is often employed in medical ultrasound to improve lateral resolution and increase the maximum attainable intensity for a given driving signal amplitude. Focusing is physically realized by a lens or curved transducer surface. In transducer arrays, focusing is achieved by time (or phase) shifting the waveform associated with each transducer element to produce an equivalent lens. Figure 2-23 depicts the approximate extent of appreciable acoustic energy in a notional focused transducer, where l_f is focal length and w_x and w_y are the spot widths in the x and y dimensions, respectively.

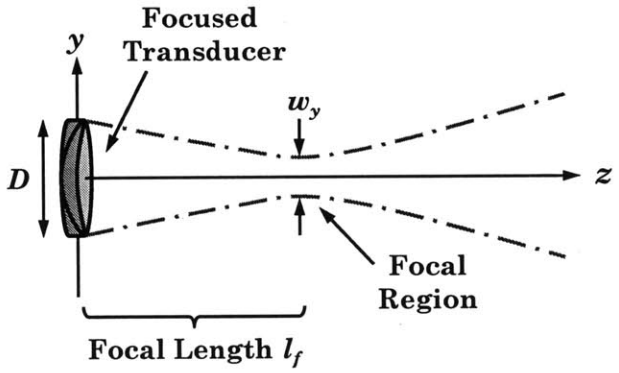

Figure 2-23: Approximate beam shape of a focused transducer. Adapted from [44].

It is convention to define l_f as the length at which the beam intensity is maximal (i.e., acoustic focus), which can differ from geometric focal length [42].

The on-axis pressure envelope for a focused and unfocused square transducer aperture (with equivalent dimensions, driving signal, and transducer impulse response) is shown in Figure 2-24.

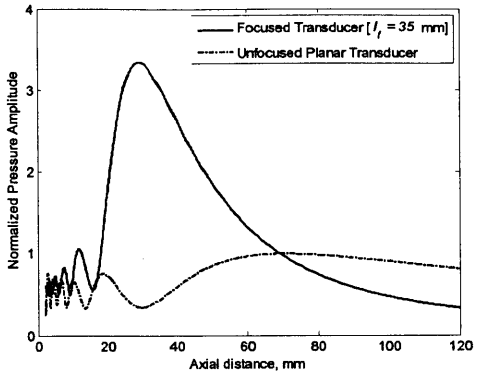

Figure 2-24: Simulated variation of on-axis pressure envelope for focused and unfocused rectangular transducer. Values are normalized to the maximum pressure magnitude of the unfocused transducer.

As expected, the focused transducer achieves significantly higher pressure at its focal region relative to the unfocused transducer maximum. Acoustic energy, however, cannot be focused beyond an aperture dependent maximum focal length $l_{f,\max}$ [44]:

$$l_{f,\max} = \frac{D^2}{2.44\lambda} \approx z_R \tag{2.61}$$

where a circular transducer is assumed, but can be extended to other geometries by using the transition distance (z_R) of the aperture. Therefore, to achieve focusing for greater insonation depths, a larger transducer aperture must be employed.

At the focal plane, the focused spot width (i.e., lateral distance between main lobe nulls) is expressed for a circular transducer as:

$$w_c = \frac{2.44\lambda l_f}{D} \tag{2.62}$$

For a rectangular aperture, spot width is determined for each lateral axis:

$$w_x = \frac{2\lambda l_f}{L_x}, \; w_y = \frac{2\lambda l_f}{L_y} \tag{2.63}$$

The minimum lateral spacing at which two point scatterers are resolvable, known as lateral resolution (LR), is reasonably estimated by spot width.

Focused half-power spot width is expressed for the circular transducer as:

$$w_{c,3dB} = \frac{1.02\lambda l_f}{D} \tag{2.64}$$

and for the rectangular transducer as:

$$w_{x,3dB} = \frac{0.88\lambda l_f}{L_x},\ w_{y,3dB} = \frac{0.88\lambda l_f}{L_y} \tag{2.65}$$

For simplicity, acoustic intensity within the half-power spot width is often assumed to be relatively uniform.

From Figure 2-24, it is apparent that pressure amplitudes near the focal region decrease more rapidly than pressure amplitudes near the axial maximum of the unfocused transducer. The axial distance over which the beam remains focused is known as the depth of focus l_{dof}. As energy becomes more concentrated in the lateral dimensions (i.e., smaller spot width), depth of focus decreases. For a circular transducer, this is expressed by the relation [44]:

$$l_{dof} \approx \frac{w_c^2}{2\lambda} \tag{2.66}$$

The relationship between l_{dof} and transducer dimensions is less straightforward for non-radially symmetric geometries, but is primarily influenced by the largest transducer dimension.

Narrow depth of focus is a critical limitation of fixed focus sonography systems. Focusing is highly advantageous in TCD systems due to considerable increases in local pressure amplitude at the region of interest. TCD sonography, however, requires velocimetry measurements over a range of insonation depths ($\approx 30 - 80$ mm), which is well beyond the depth of focus for a single transducer element. Although lenses can be interchanged to alter focal length, this procedure is exceedingly inconvenient in TCD evaluations since measurements throughout a vessel course are necessary. Phased array architectures, which enable dynamic focal length variation, are therefore suitable for focused TCD sonography.

2.2.9 Pulsed Transducer Beam Patterns

The classic treatment of acoustic fields is based on continuous wave solutions. Although analytical beam pattern expressions from CW derivations are useful in obtaining insight into PW functionality, such results do not yield a precise description of PW beam pattern formation (especially for short pulses where $M < 6$) [42]. Because pulsed operation is achieved through time gating, time domain expressions are amenable for PW analysis.

A widely used method, first developed by Tupholme and Stepanishen and further refined by Jensen, employs the transducer spatial impulse response to compute radiation patterns for an arbitrary excitation waveform [62–64]. The coordinate system used in planar transducer beam pattern analysis is shown in Figure 2-10, which is repeated here as Figure 2-25 for convenience.

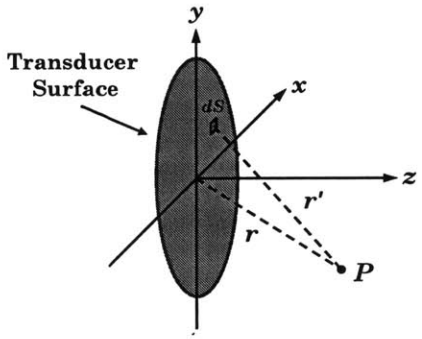

Figure 2-25: Coordinate system for analysis of planar transducer beam patterns.

Assuming an infinite rigid transducer baffle and a homogeneous propagating medium, the pressure variation at point P is expressed by a general form of the Rayleigh integral [43]:

$$p\left(\vec{r},t\right)=\frac{\rho_0}{2\pi}\int_S\frac{\frac{\partial u}{\partial t}\left(\vec{r_s},t-\frac{|\vec{r}'|}{c}\right)}{|\vec{r}'|}dS \tag{2.67}$$

where S denotes the transducer surface and $u\left(\vec{r_s},t\right)$ is the time dependent velocity normal to the transducer surface at dS (i.e., $\vec{r_s}$ is a vector from the origin to dS).

Separation of the transducer spatial impulse response $h\left(\vec{r},t\right)$, which characterizes the three-dimensional field due to impulse excitation, from the Rayleigh integral is

used to facilitate radiation pattern calculations. Assuming uniform velocity across the transducer surface, $h(\vec{r},t)$ can be expressed as [64]:

$$h(\vec{r},t) = \int_S \frac{\delta\left(t - \frac{|\vec{r}'|}{c}\right)}{2\pi|\vec{r}'|} dS \tag{2.68}$$

where $\delta(\cdot)$ denotes the Dirac delta function. Effects due to attenuation and non-uniform surface velocity – caused by media absorption and apodization, respectively – can be incorporated into this analysis framework through direct modification of the spatial impulse response.

For transducer arrays, an equivalent spatial impulse response $h_{\text{array}}(\vec{r},t)$ is defined by combining the spatial impulse responses of individual transducer elements:

$$h_{\text{array}}(\vec{r},t) = \sum_{n=1}^{N} h_n(\vec{r}_n,t_n) = \sum_{n=1}^{N} h_{\text{el}}(\vec{r} - \vec{r}_{\text{offset},n}, t - t_{\text{delay},n}) \tag{2.69}$$

where $h_{\text{el}}(\vec{r},t)$ is the spatial impulse response for an element at the origin, N is the number of array elements, $\vec{r}_{\text{offset},n}$ is a vector from the origin to the n^{th} transducer element center, and $t_{\text{delay},n}$ is the excitation delay for the n^{th} transducer element. Equation 2.69 assumes equivalent transducer elements and simple time delays between element excitations. Apodization can be achieved through scaling of the individual element spatial impulse responses $h_n(\vec{r_n},t_n)$ within the summation term.

Because the spatial impulse technique separates transducer geometry effects from the excitation waveform, modifications to the driving signal – such as timing delays in phased array systems – do not require repeated integration to determine $h(\vec{r},t)$ and therefore often result in more efficient computation. As pulse length expands (i.e., M increases), the resulting field pattern converges to the continuous wave solution. The resultant pressure field for a given excitation is expressed as [64]:

$$p(\vec{r},t) = \rho_0 u(t) \underset{t}{*} \frac{\partial h(\vec{r},t)}{\partial t} \tag{2.70}$$

where $\underset{t}{*}$ denotes temporal convolution.

Analytical solutions for the spatial impulse response can be computed for a number of basic transducer geometries, as described in [43, 65]. The method is often solved numerically by field solvers, such as the Field II ultrasound simulator developed by Jensen [38, 39]. Figure 2-26 displays the effect of pulse length on the pulse intensity profile.

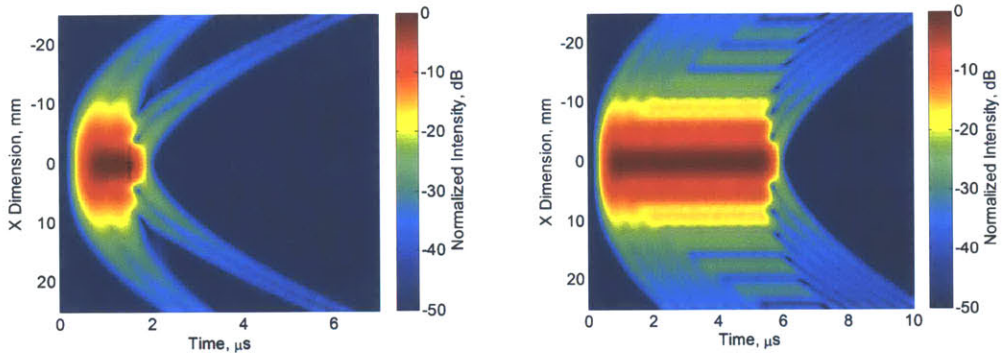

(a) Time dependent intensity variation in the x dimension for $M = 2$

(b) Time dependent intensity variation in the x dimension for $M = 10$

Figure 2-26: Simulated intensity envelope for a 13 mm diameter circular transducer operating at 2 MHz.

Using the concept of time averaged intensity, the beam pattern for pulsed excitation apertures can also be computed using field solvers, as shown in Figure 2-27.

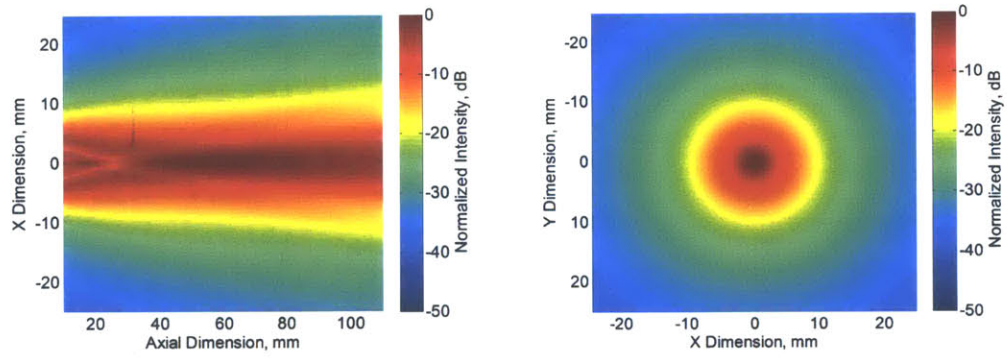

(a) Intensity variation in the xz-plane at $y =$ 0 mm.

(b) Intensity variation in the xy-plane at $z =$ 60 mm.

Figure 2-27: Simulated time averaged intensity for a 13 mm diameter circular transducer operating at 2 MHz for M = 2.

Comparison of Figure 2-27 to CW simulations for an equivalent transducer, as shown in Figure 2-12, highlights the significant effect of PW operation on beam pattern formation. Pulsed excitations, as a result of their considerable bandwidth, tend to produce less abrupt beam patterns (i.e., lower spatial derivatives) and lower sidelobe levels than observed in monochromatic CW operation. This effect is most pronounced in the near-field region, where CW operation leads to high intensity variability.

2.2.10 Pulse-Echo Operation

The spatial impulse response method developed in Section 2.2.9 can be extended to analysis of the pulse-echo process for point scattering (i.e., exceedingly small inhomogeneities).

Figure 2-28 presents the fundamental components of a pulse-echo ultrasound system.

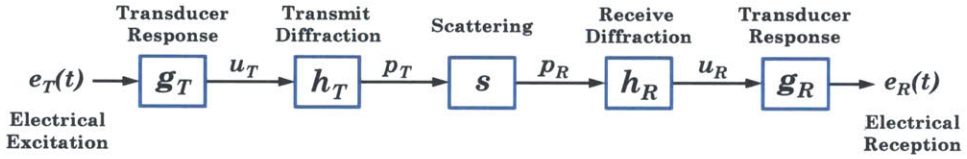

Figure 2-28: Block diagram representation of a pulse-echo ultrasound system. Adapted from [65].

During transmission, the electrical excitation signal $e_T(t)$, denoted $e_{PW}(t)$ in Section 2.2.2 for a PW excitation signal, yields a transmit velocity $u_T(t)$ at the transducer surface. Using the transmit electroacoustic conversion impulse response $g_T(t)$, transmit surface velocity is expressed as:

$$u_T(t) = e_T(t) \underset{t}{*} g_T(t) \tag{2.71}$$

Transmit and receive electroacoustic conversion impulse responses – $g_T(t)$ and $g_R(t)$, respectively – can be determined from an equivalent circuit transducer model, as discussed in Section 2.2.3.

The transmit (i.e., incident) pressure field $p_T(\vec{r},t)$ can thereby be computed as:

$$p_T(\vec{r},t) = \rho_0 u_T(t) \underset{t}{*} \frac{\partial h_T(\vec{r},t)}{\partial t} = \rho_0 e_T(t) \underset{t}{*} g_T(t) \underset{t}{*} \frac{\partial h_T(\vec{r},t)}{\partial t} \tag{2.72}$$

where $h_T(\vec{r},t)$ is the transmit aperture spatial impulse response.

Inhomogeneities are treated as point scatterers using the scattering field function $s(\vec{r})$, defined as [43]:

$$s(\vec{r}) = \frac{\Delta\rho(\vec{r})}{\rho_0} - 2\frac{\Delta c(\vec{r})}{c_0} \tag{2.73}$$

where ρ_0 and c_0 are the average density and velocity of propagation within the medium, respectively. Functions $\Delta\rho(\vec{r})$ and $\Delta c(\vec{r})$ contain perturbations in acoustic properties and thereby produce scattering.

For a finite number of point scatterers ($N_{\text{scatterers}}$), functions $\Delta\rho(\vec{r})$ and $\Delta c(\vec{r})$ are expressed as:

$$\Delta\rho(\vec{r}) = \sum_{n=1}^{N_{\text{scatterers}}} (\rho_n - \rho_0)\,\delta(\vec{r} - \vec{r}_n) \tag{2.74}$$

$$\Delta c(\vec{r}) = \sum_{n=1}^{N_{\text{scatterers}}} (c_n - c_0)\,\delta(\vec{r} - \vec{r}_n) \tag{2.75}$$

where ρ_n and c_n indicate the density and acoustic velocity of perturbations (i.e., discrete scatterers), respectively, and $\vec{r}_n$ denotes the position vector of the n^{th} scatterer with respect to transducer origin.

The electrical receive signal $e_R(t)$ can thereby be computed completely in terms of the electrical excitation, transducer impulse responses, aperture spatial impulse responses, and the scattering field function. Assuming coincident transmit and receive apertures – such that the origin remains common – $e_R(t)$ is expressed as [40, 64]:

$$e_R(t) = \frac{1}{c_0^2} e_T(t) \underset{t}{*} g_T(t) \underset{t}{*} g_R(t) \underset{t}{*} \frac{\partial h_T(\vec{r},t)}{\partial t} \underset{t}{*} \frac{\partial h_R(\vec{r},t)}{\partial t} \underset{r}{*} s(\vec{r}) \tag{2.76}$$

where $h_R(\vec{r},t)$ is the receive aperture spatial impulse response and $g_R(t)$ is the receive electroacoustic conversion impulse response, which is necessary to convert between

receive velocity $u_R(t)$ and the receive voltage waveform $e_R(t)$:

$$e_R(t) = u_R(t) \underset{t}{*} g_R(t) \tag{2.77}$$

The point spread function (PSF), a common measure of resolution capability in ultrasound systems, can be obtained using the convolution based field analysis methods described. A single perturbation in the scattering field function is first defined. Receive signal magnitude across a set of spatial locations adjacent to the perturbation yields the PSF. An acoustic floor of the PSF is established by the sidelobe levels of the transmit and receive apertures. In general, the PSF is dependent on scatterer location within the field of view.

The preceding analysis of pulse-echo operation assumes linearity, time-invariance, and point single scattering (i.e., scattering at discrete points due solely to incident radiation). This method can, in principal, be modified to account for anisotropic point scattering via the differential scattering cross-section $\sigma_{ds}(\theta)$, as discussed in Section 2.1.1. Bulk inhomogeneities, however, cannot be modeled under the previous formulation and require alternative approaches, such as modified angular spread methods, finite-difference time-domain (FDTD) methods, and FEA [66].

2.3 Phased Array Beam Steering and Focusing

Phased array beamformation is based on the coherent summation of related waveforms. An acoustic beam pattern can be electronically formed through the control of time delays and amplitude scale factors for each element in the transducer array. Beamformation is comprised of beam steering (i.e., modification of main beam direction, referred to as the steering angle) and beam focusing (i.e., convergence of main beam energy at a particular depth, referred to as the focal length). Phased array beamformation is achieved during both pulse transmit and echo receive, creating an effective pulse-echo spatial impulse response expressed by $h_{PE}(\vec{r},t) = h_R(\vec{r},t) \underset{t}{*} h_T(\vec{r},t)$.

In transmit beamforming, the excitation pulse for each element is a time-delayed version of the periodic basis function, defined by the transmit beamformer. Excitation amplitude scaling is also often applied to realize apodization of the transmit aperture. Following transduction, the delayed acoustic waveforms define a surface within the propagating media of approximately equal phase near the transducer elements, known as the equiphase surface. For a single element transducer, the transducer surface – driven by a common excitation – forms the equiphase surface. A phased array beam pattern is therefore comparable to the beam pattern of a single element transducer defined by the equiphase surface. The planar component of the equiphase surface determines the steering angle (i.e., beam steering), while surface curvature defines the focal length (i.e., beam focusing). The process of transmit beamformation is presented in Figure 2-29.

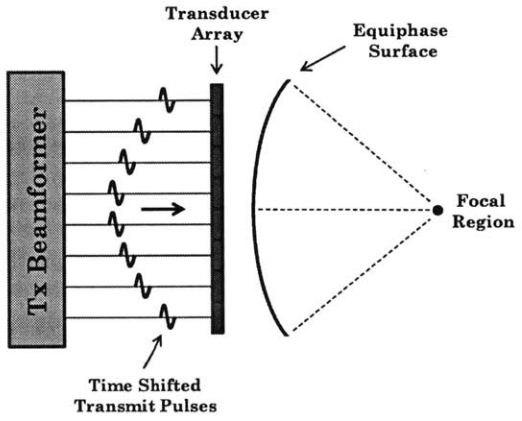

Figure 2-29: Transmit phased array beamformation.

Similarly, receive beamformation is achieved through control of time delays and amplitude scaling as defined by the receive beamformer. However, because receive waveforms are manipulated subsequent to transduction, receive beamformer designs are less restricted by implementation constraints (e.g., interfacing with high-voltage pulse signals) and are therefore often more configurable.

Electronic beamformation is utilized in the TCD applications of this work for two primary functions: to steer the main beam direction for location of the vessel of interest and to increase acoustic intensity – for a given acoustic output power –

at the vessel of interest via focusing, thereby potentially improving acoustic window patency.

The coordinate framework for basic analysis of phased array beam steering and aperture focusing in a homogeneous acoustic medium is presented in Figure 2-30.

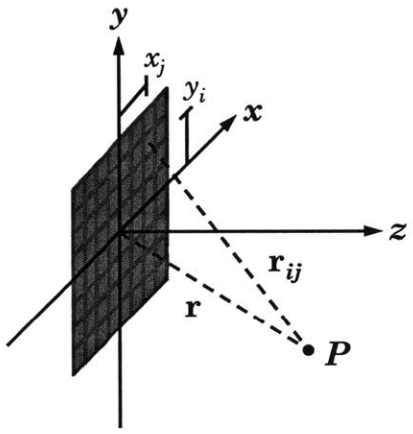

Figure 2-30: Coordinate system for analysis of electronic phased array beam steering and focusing.

To achieve beam steering along the $\vec{r}$ direction with a focal region at point P, the time delay required for a transducer element in the i^{th} row and j^{th} column – denoted $\Delta t_{i,j}$ – is expressed as:

$$\Delta t_{i,j} = \frac{r - r_{i,j}}{c} + t_0 = \frac{r - \sqrt{(r_x - x_j)^2 + (r_y - y_i)^2 + r_z^2}}{c} + t_0 \qquad (2.78)$$

where $r = |\vec{r}| = |(r_x, r_y, r_z)|$, t_0 is a constant delay term ensuring causality (i.e., $\Delta t_{i,j} \geq 0 \; \forall \; i, j$), and x_j and y_i are the element center offsets from the origin in the x and y dimensions, respectively. Amplitude scaling is defined by discretizing an amplitude weighting function, as discussed in Section 2.2.7, at the element center offsets. Additional complexities related to phased array beamformation – such as grating lobes and element directivity effects – are discussed in Section 2.2.6.

Tissue inhomogeneities act to distort the focal region, leading to spreading of acoustic energy and reductions in focal intensities. The phased array beam steering expression described in Equation 2.78 assumes a homogeneous medium and thus a

constant propagation velocity c. Because changes in propagation velocity are marginal for a variety of soft tissue types, this assumption yields tolerable effects in most medical ultrasound applications. As presented in Table 2.1, the propagation velocity through cranial bone, however, is markedly distinct from soft tissue.

For transcranial sonography applications, differences in path length through bone, due to skull thickness variations across the aperture and differences in $\vec{r_{ij}}$ angle, cause diminished coherence at the focal region – a phenomena referred to as focal aberration. Differences in acoustic propagation velocity at the interface between bone and soft tissue yield refraction effects, as discussed in Section 2.1.1, which alters wave direction and thereby produces beam pattern distortions [35]. These nonidealities are a primary reason for poor image quality in transcranial ultrasound imaging modalities, such as TCCS.

By modifying delay timings, beam pattern distortion effects due to focal aberration and refraction can be significantly mitigated and the focal region restored to its intended position. Such methods, referred to as phase-correction techniques, cannot be achieved using physical focusing mechanisms (e.g., curved transducer surfaces, lenses) – due to inadequate reconfigurability and mechanical realizability – and are thereby exclusive to phased array apertures. Phase-correction algorithms are discussed further in Section 3.1.2.

2.4 Doppler Ultrasound and Velocity Estimation

In a majority of TCD applications, the true clinical parameter of interest is cerebral blood flow (CBF). Doppler methods, however, yield flow velocities and – due to anatomical constraints – diameter of the cerebral arteries cannot be measured via acoustic means with sufficient accuracy to obtain absolute volume flow [67]. Nonetheless, Doppler ultrasound can provide a phenomenal representation of the dynamic progression of *in vivo* blood through the cerebrovasculature, which cannot be acquired from any other non-invasive modality.

Although absolute CBF cannot be accurately measured in TCD applications with-

out reliable vessel dimensions, relative changes in CBFV can be used as a surrogate marker for CBF variation when changes in vessel lumen diameter are small (or otherwise predictable). The MCA – and other major basal cerebral arteries – serve mainly as conductance channels and are not significantly involved in the active regulation of blood flow. MCA diameter does not change appreciably for moderate variations in arterial carbon dioxide partial pressure [68–70].

Studies have shown that CBF, measured at the internal carotid artery via electromagnetic flowmetry, and CBFV envelope (discussed in Section 2.4.2), measured at the MCA via TCD, are highly correlated for moderate changes in ABP [67, 71]. However, administration of certain chemical – such as nitroglycerin – result in significant vasodilation of the basal intracranial arteries and can thereby confound TCD measurements [72].

Certain applications of TCD – notably embolus detection and vasospasm monitoring – do not rely on the assumption of constant vessel diameter, but instead depend on CBFV parameters directly as indications of pathology. Recognition of the underlying assumptions required by specific TCD applications is therefore essential for the proper interpretation of measurement data.

The use of Doppler ultrasound to quantify blood flow velocity was first described in 1960 by Satomura and Kaneko [73]. It was not until 1981 that Aaslid adapted Doppler techniques for transcranial examination of the cerebral vessels [74]. Due to relatively simple hardware implementations, early Doppler sonography utilized CW operation. All CW receive samples, however, correspond to the entire depth of insonation, leading to range ambiguity. Because CW excitation is uninterrupted, physically separate transmit and receive transducers must be employed. Limited axial discrimination can be obtained via partial overlapping of transmit and receive beam patterns, but degrades as depth increases and further complicates vessel location.

By contrast, PW operation exploits time encoding of scatterer spatial position. In TCD sonography, exceedingly large amplitude reflections, due to the presence of cranial bone and other axially distant stationary scatterers, can be neglected by time gating the receive signal about the depth of interest. PW excitation enables superior

axial resolution than can be achieved solely through focal beamformation methods. Because receiver electronics must simultaneously detect low-level signals from mobile scatterers and high-level scattering from stationary tissue, PW operation greatly reduces system dynamic range requirements by eliminating scatterer reflections outside the sample volume. Further analysis of TCD velocimetry applications in this work will therefore concentrate on PW excitation.

2.4.1 Velocity Estimation for a Single Scatterer

At a basic level, scatterer velocity is determined by repeated pulse emissions and comparison of received time shifts between adjacent pulses. The PW velocity estimation algorithm is first described for a single scatterer within a highly simplified framework and then extended to an ensemble of scatterers. As shown in Figure 2-31, a scatterer starts at depth z_0 – relative to the ultrasound transducer surface – and moves with a constant velocity vector $\vec{v}$, where θ_D is the angle between $\vec{v}$ and the z-axis, $v_z = \vec{v}\cos\theta_D$ represents the velocity component normal to the transducer surface, and the scatterer is assumed to be along or sufficiently near the z-axis. The angle θ_D is generally referred to as the Doppler angle.

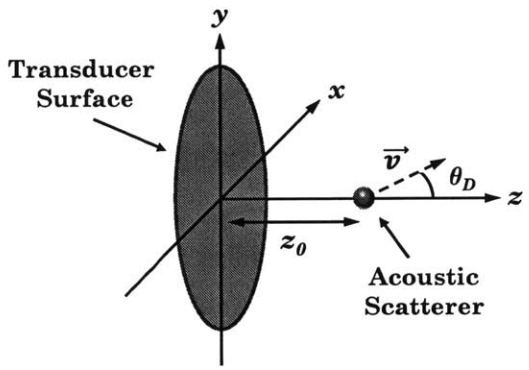

Figure 2-31: Coordinate system for analysis of PW velocity estimation.

Plane wave propagation of the incident and scattered waveforms, although not indicated in Figure 2-31, is initially assumed for analytical tractability. Transmit and receive transducer apertures, as well as transducer impulse response effects, are

therefore implicitly neglected. This highly reduced model will initially be analyzed, then further developed within a realistic acoustic context.

In medical Doppler sonography, M (i.e., number of cycles within the periodic basis function) is typically a moderate value (i.e., < 20) corresponding to a range gate length l_g of several millimeters:

$$l_g = \frac{Mc}{2f_e} \tag{2.79}$$

The range gate length characterizes the possible scatterer depths over which the electrical receive signal is influenced.

The sample offset T_s is defined as the time delay between pulse emission and sampling of the electrical receive signal. The sample depth z_s is thereby expressed as:

$$z_s = \frac{T_s c}{2} \tag{2.80}$$

where the sample depth z_s is selected to correspond to the depth of interest (e.g., z_0 in this simplified geometry, aperture focal length in typical focused Doppler applications).

Sampling of the electrical receive signal $e_R(t)$ at sample offset time T_s is therefore only affected by scatterers contained within the sample volume depth z_{sv}:

$$z_{sv} = \left[z_s - \frac{l_g}{2},\ z_s + \frac{l_g}{2} \right] \tag{2.81}$$

A single acoustic pulse emission $e_{T0}(t)$ – the pulsed excitation basis function described in Section 2.2.2 – is initiated at time t_{e0} and travels outward from the transducer with propagation velocity c. Scatterer and pulse front depth along the z-axis are expressed as:

$$z_{scatterer}(t) = z_0 + t\,|\vec{v}| \cos\theta_D = z_0 + v_z t \tag{2.82}$$

$$z_{pulse}(t) = c\,(t - t_{e0})\,H_{step}(t - t_{e0}) \tag{2.83}$$

where $H_{step}(t)$ is the Heaviside step function, given by:

$$H_{step}(t) = \begin{cases} 0, & t < 0 \\ 1, & t \geq 0 \end{cases} \tag{2.84}$$

The scatterer and pulse front are spatiotemporally coincident at the interaction time t_{i0}, which results in the emission of a scattered acoustic wave. The interaction time is calculated as:

$$z_{scatterer}(t_{i0}) = z_{pulse}(t_{i0}) \rightarrow t_{i0} = \frac{z_0}{c - v_z} + \frac{c}{c - v_z} t_{e0} \tag{2.85}$$

Beginning at time t_{r0}, a backscattered wave is received at the transducer. The time delay between pulse emission and interaction is equivalent to the time delay between interaction and pulse reception, leading to the relation [43]:

$$t_{r0} = t_{e0} + 2(t_{i0} - t_{e0}) \rightarrow t_{e0} = t_{r0}\frac{c - v_z}{c + v_z} - \frac{2z_0}{c + v_z} \tag{2.86}$$

For a single pulse emission, the received electrical waveform $e_{R0}(t)$ can therefore be described as a time-scaled and delayed version of the pulsed excitation basis function $e_{T0}(t)$:

$$e_{R0}(t) = A_R e_{T0}\left(t\frac{c - v_z}{c + v_z} - \frac{2z_0}{c + v_z}\right) \tag{2.87}$$

where A_R is an amplitude scaling coefficient (related to the reflection coefficient Γ for plane wave scattering).

As discussed in Section 2.2.2, the PW transmit excitation waveform $e_T(t)$ can be synthesized by combining time-shifted versions of the basis function $e_{Tn}(t)$:

$$e_{Tn}(t) = e_{T0}(t - nT_{PRP}) \tag{2.88}$$

$$e_T(t) = \sum_{n=0}^{\infty} e_{Tn}(t) = \sum_{n=0}^{\infty} e_{T0}(t - nT_{PRP}) \tag{2.89}$$

A notional PW transmit excitation waveform $e_T(t)$ is shown in Figure 2-8 and is

repeated here as Figure 2-32 for convenience, where waveform labels $e_{Tn}(t)$ indicate the nonzero segment of each time-shifted representation of the basis function.

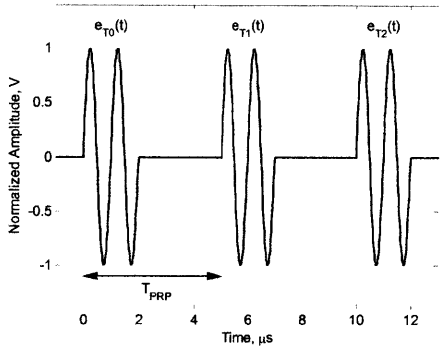

Figure 2-32: Pulsed wave excitation waveform ($M = 2$, $T_e = 1.0\mu s$, and $T_{PRP} = 5\mu s$).

The windowing function $\prod\left(\frac{t}{T_e M} - \frac{1}{2}\right)$ is fairly narrow in time. Therefore, the PW transmit excitation $e_T(t)$ has considerable half-power bandwidth $BW_{T,3dB}$:

$$BW_{T,3dB} = \frac{f_e}{M} \tag{2.90}$$

The frequency spectrum of a realistic PW excitation waveform $e_T(t)$ is given in Figure 2-33. The spectral content of $e_T(t)$ is characterized by a main tone at the excitation frequency f_e. Secondary tones occur at integer offsets of the pulse repetition frequency f_{PRF} from the main tone and are shaped by the transmit excitation bandwidth $BW_{T,3dB}$:

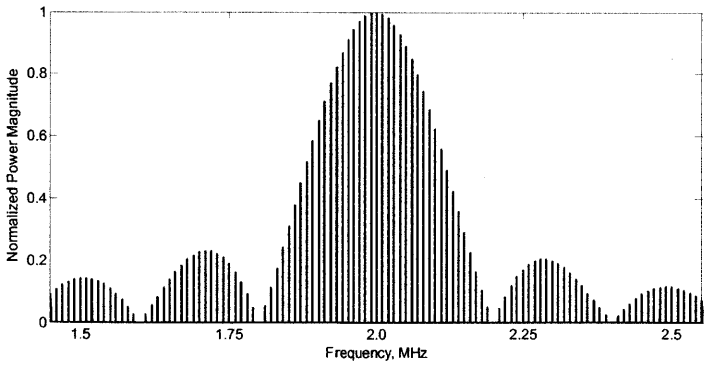

Figure 2-33: Notional pulsed transmit excitation spectrum for $M = 10$, $T_e = 0.5\mu$s, and $T_{PRP} = 0.1\mu$s.

The time-space relationship between a constant velocity scatterer and the periodic transmit waveform is depicted in Figure 2-34.

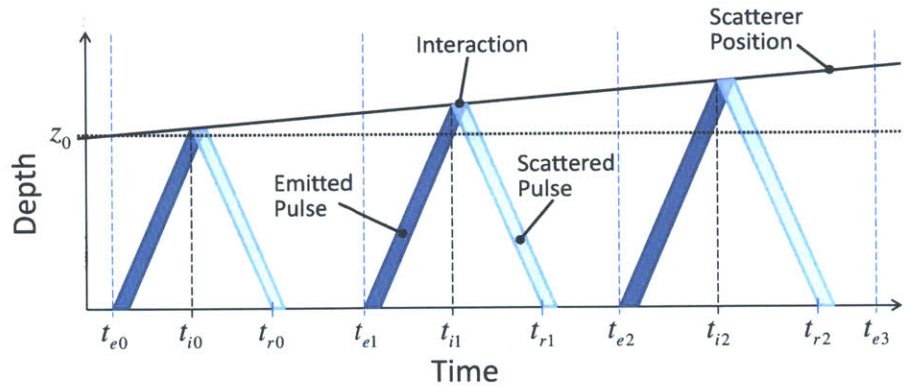

Figure 2-34: Time-space diagram of scatterer and pulse interaction.
Adapted from [43].

Due to periodic replication of the emitted pulse, a single pulse receive waveform can be written in terms of the emitted pulse from the preceding pulse repetition:

$$e_{Rn}(t) = A_R e_{Tn}\left(t\frac{c-v_z}{c+v_z} - \frac{2z_0}{c+v_z}\right) = A_R e_{T(n-1)}\left(t\frac{c-v_z}{c+v_z} - \frac{2z_0}{c+v_z} - T_{PRP}\right) \tag{2.91}$$

By recursion to the initial pulse emission, the single pulse receive waveform due to the n^{th} pulse repetition can described in terms of the pulsed excitation basis function:

$$e_{Rn}(t) = A_R e_{T0}\left(t\frac{c-v_z}{c+v_z} - \frac{2z_0}{c+v_z} - nT_{PRP}\right) \tag{2.92}$$

Summation of the single pulse receive waveforms over all pulse repetitions yields the electrical receive signal $e_R(t)$:

$$e_R(t) = \sum_{n=0}^{\infty} e_{Rn}(t) \tag{2.93}$$

Sampling $e_R(t)$ at the pulse repetition frequency (i.e., one sample per pulse period) with a constant sample offset time T_s – corresponding to the desired sampling depth

z_s – yields a discrete-time receive sequence $x[n]$:

$$x[n] = e_R(nT_{PRP} - T_s) \tag{2.94}$$

To avoid time aliasing, the pulse repetition frequency must be selected such that received signals from adjacent pulse repetitions do not overlap in time. Under this f_{PRF} requirement, the n^{th} sample is determined solely by the n^{th} single pulse receive waveform:

$$x[n] = e_{Rn}(nT_{PRP} - T_s) \tag{2.95}$$

Without loss of generality, the pulsed excitation basis function is expressed as a gated sinusoid to facilitate spectral analysis of the receive sequence $x[n]$:

$$e_{T0}(t) = \prod\left(\frac{t}{T_e M} - \frac{1}{2}\right)\sin(2\pi f_e t) = \begin{cases} \sin(2\pi f_e t), & 0 \le t \le T_e M \\ 0, & \text{otherwise} \end{cases} \tag{2.96}$$

Using the basis function expression, the receive sequence can be solved for explicitly.

$$x[n] = A_R e_{T0}\left(nT_{PRP}\frac{c - v_z}{c + v_z} - nT_{PRP} - \frac{2z_0}{c + v_z} - T_s\frac{c - v_z}{c + v_z}\right) \tag{2.97}$$

Defining a constant phase term ψ_e:

$$\psi_e = 2\pi f_e\left(\frac{2z_0}{c + v_z} + T_s\frac{c - v_z}{c + v_z}\right), \tag{2.98}$$

yields a reduced form of the expression:

$$x[n] = -A\sin\left(\frac{4\pi f_e T_{PRP} v_z n}{c + v_z} + \psi_e\right) \tag{2.99}$$

Therefore, under the simplified framework presented, sampling the electrical receive signal $e_R(t)$ at the pulse repetition frequency yields a frequency spectrum with energy concentrated at the Doppler frequency f_d:

$$f_d = \pm\frac{2f_e v_z}{c + v_z} \approx \pm\frac{2f_e v_z}{c} \tag{2.100}$$

The preceding velocity estimation procedure is primarily founded on methods introduced by Bonnefous and Pesque, which were later refined and advocated by Jensen [64, 75]. Alternative velocity estimation methods are also commonly used, including the phase and cross-correlation based estimators presented in [40].

It should be noted that use of the term Doppler in PW systems is somewhat of a misnomer. The relative shift in scatterer position between pulse emissions is the underlying phenomena measured in PW operation. The Doppler effect, in contrast, yields frequency shifts induced by instantaneous scatterer velocities. Although the distinction may appear subtle, the sizeable bandwidths used in PW operation make it exceedingly difficult to measure modest Doppler frequency variations through media with frequency dependent attenuation characteristics [43]. Nevertheless, the term Doppler, although formally incorrect, is widely established for pulsed excitation and will be used throughout this work when referring to PW velocity estimation methods. Equation 2.100 – although referring to Doppler frequency – has been specifically derived for PW operation and remains valid despite this incongruity in nomenclature.

2.4.2 Velocity Estimation for an Ensemble of Scatterers

The velocity estimation methods initially presented for a single scatterer can be expanded to practical acoustic contexts for a collection of scatterers.

Recall from Equation 2.76 that accurate calculation of the electrical receive signal $e_R(t)$ is founded on convolution of the PW transmit excitation waveform $e_T(t)$ with physical system characteristics – notably transmit and receive transducer impulse responses $g(t)$ and spatial impulse responses $h(t)$. Because the convolution operation is time invariant, the receive waveform from stationary scatterer and time-shifted pulse emissions will be exactly identical (neglecting noise effects).

If the effective pulse-echo spatial impulse response $h_{PE}(\vec{r}, t)$ is relatively constant in magnitude for the range of scatterer positions, then scatterer waveforms can be approximated solely by time delays – as presented in the previous section – with no appreciable change in amplitude. For scatterers confined to the sample volume depth range z_{sv} and within a nearly constant magnitude region of the main beam

of the pulse-echo beam pattern, the velocity estimation procedure remains valid. As scatterers move away from the z-axis, the use of a single Doppler angle θ_D becomes less valid due to angle approximation errors and velocity estimation accuracy is degraded. Such angle variation errors, however, are fairly negligible in TCD insonation of the MCA, since the scatterers are confined to a roughly 3 mm diameter vessel at a sample depth of ≈ 40 mm.

For transducer arrays, where beam steering enables the main lobe to be offset from the vector normal to the transducer surface, the coordinate system can be transformed such that the z-axis corresponds to the beam steering angle, and θ_D is defined between the steering direction and the scatterer velocity vector, thus approximating the phased array as an equivalent steered element.

Because a linear system is assumed, velocity estimation analysis can be applied to an ensemble of scatterers defined by a dynamic scattering field $s(\vec{r}, t)$, where each scatterer position is approximated using a scatterer velocity vector and previous scatterer position:

$$\vec{r_n}(t) = \lim_{\Delta t \to 0} \vec{r_n}(t - \Delta t) + \vec{v_n}(t)\,\Delta t \tag{2.101}$$

One practical inconsistency with the velocity estimation analysis presented in Section 2.4.1 is that constant scatterer velocity is maintained over all pulse repetitions, but scatterers must remain confined to the sample volume depth range z_{sv} and a constant magnitude region of the pulse-echo beam pattern. These analytical limitations present two major discrepancies. First, blood flow within major arteries is a highly pulsatile phenomenon. Scatterer velocity is therefore grossly misrepresented by a constant velocity approximation. Blood flow velocity can, however, be accurately characterized as constant over a time interval of several milliseconds [76]. Second, after sufficient time all scatterers with non-zero velocity will not be confined to the sample volume depth range or a constant magnitude region of the pulse-echo beam pattern.

These concerns can be mitigated by use of the spectrogram, known in the context of ultrasound as the sonogram, which provides a time-varying spectral representa-

tion of the receive sequence $x[n]$ through computation of the time-dependent Fourier transform [61]. To determine the spectral content of $x[n]$ for a particular sample interval – corresponding to a time interval in $e_R(t)$ – the receive sequence is multiplied by a window sequence, as described in Section 3.4. For a sufficiently short window (i.e., on the order of several milliseconds in duration), flow velocity and the pulse-echo spatial impulse response magnitude (across the length traveled by a scatterer) can be approximated as constant. For an ensemble of erythrocytes at *in vivo* concentrations and flow velocities, there will still be a large number of scatterers entering and exiting the sample volume depth range. From each pulse repetition, however, this number is a slight fraction of the total scatterers within the sample volume and can typically be neglected.

Pulse repetition frequency limits exist in order to ensure aliasing is prevented throughout the velocity estimation procedure. To avoid aliasing in the frequency domain, a minimum pulse repetition frequency $f_{PRF,min}$ is determined by the maximum scatterer velocity magnitude.

$$f_{PRF,min} = \frac{4 f_e v_{\max}}{c} \tag{2.102}$$

This restriction permits scatterer velocity to vary within $[-v_{\max}, v_{\max}]$ without risk of frequency aliasing. A priori knowledge of scatterer velocity (e.g., absence of negative flow) can be used to extend acceptable flow velocities to larger values without accuracy degradation. Pathological blood flow is, however, often notably distinct from normal flow patterns, which cannot generally be presumed. In TCD applications, flow direction is highly dependent on anatomical factors (e.g., transtemporal insonation typically yields positive flow velocities for the ipsilateral MCA and negative flow velocities for the ipsilateral anterior cerebral artery).

As sampling depth z_s increases, scattered energy from the sample volume takes additional time to reach the transducer surface and therefore the rate of pulse emissions

(i.e., f_{PRF}) must decrease to avoid time domain aliasing:

$$f_{PRF,\max} = \frac{c}{2z_s + l_g} \tag{2.103}$$

The spectral content of $x[n]$ for arterial blood flow – even when utilizing short window sequences – contains a wide distribution of frequencies, a result of radial dependent erythrocyte velocity. Within the circulatory system, blood flow is generally laminar (i.e., Reynolds number < 2000) and evidence of turbulence is often an indication of pathology (e.g., stenotic vessel). A notional scatterer velocity distribution for laminar flow is depicted in Figure 2-35.

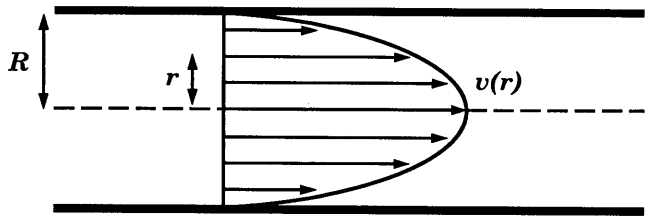

Figure 2-35: Laminar flow velocity in a long, rigid tube. Adapted from [43].

The scatterer velocity profile for steady (i.e., non-pulsatile) laminar flow in a rigid tube can be described by the Poiseuille relation, given by [43]:

$$v(r) = v_{0,\max}\left[1 - \left(\frac{r}{R}\right)^{p_0}\right] \tag{2.104}$$

where r is radial position, R is tube radius, $v_{0,\max}$ is maximum scatterer velocity, and p_0 is velocity profile order. Near an inlet, entrance effects tend to dominate thereby yielding a flat velocity profile ($p_0 \to \infty$). For long tubes, viscosity effects establish parabolic flow ($p_0 \to 2$). As indicated by Equation 2.104, a linear relationship exists between $v_{0,\max}$ and mean flow velocity.

In practice, blood vessels are elastic structures, rather than rigid tubes, and blood flow is pulsatile, rather than steady. Scatterer velocity is therefore radially and temporally influenced. Using Fourier decomposition, scatterer velocities throughout pulsatile flow can be analyzed from a set of Womersley equations, but require a number

of vessel specific parameters not generally available in a clinical setting [77, 78].

Ideally, the spectral power at a particular Doppler frequency is proportional to the number of erythrocytes within the sample volume moving at the corresponding axial velocity. Formally, since the backscatter coefficient of blood is nonmonotonic with hematocrit, this relationship is not valid for erythrocyte scattering (as described in Section 2.1.1). However, because hematocrit is constant through the sample volume and rouleaux formation is negligible in arterial flow, the proportionality assumption is approximately valid. Therefore, calculation of spectral mean Doppler frequency can theoretically yield an accurate representation of mean flow velocity $\bar{v}[n]$.

Spectral mean Doppler frequency $\bar{f}_d[n]$ is computed by power-weighting the spectral content of the time-dependent discrete Fourier transform (TDDFT) of $x[n]$:

$$\bar{f}_d[n] = \frac{\int_0^{2\pi} \lambda |X[n,\lambda)|^2 d\lambda}{\int_0^{2\pi} |X[n,\lambda)|^2 d\lambda} \tag{2.105}$$

where $X[n,\lambda)$ is the TDDFT of $x[n]$ [61]. Recall that n is a sequence index corresponding to continuous time sampling at $t_n = n \cdot T_{PRP} + T_s$.

Doppler estimated mean flow velocity $\bar{v}[n]$ is thereby expressed as:

$$\bar{v}[n] = \frac{\bar{f}_d[n]\, c}{2 f_e \cos\theta_D} \tag{2.106}$$

Volumetric flow (e.g., CBF through the MCA) can be obtained by utilizing measured vessel diameter $d_v[n]$:

$$q[n] = \frac{\pi \bar{v}[n]\, d_v^2[n]}{4} = \frac{\pi c\, \bar{f}_d[n]\, d_v^2[n]}{8 f_e \cos\theta_D} \tag{2.107}$$

Finally, if vessel diameter is constant over the cardiac cycle, volumetric blood flow through the vessel can be estimated to within a constant scale factor (i.e., q_0). For a constant vessel diameter, the linear relationship between volumetric blood flow and $\bar{v}[n]$ allows changes in blood flow through the vessel of interest to be directly

monitored using CBFV measurements.

$$\hat{q}[n] = \frac{\pi c \bar{f}_d[n] d_v^2}{8 f_e \cos\theta_D} = q_0 \bar{f}_d[n] \tag{2.108}$$

Equations 2.107 and 2.108 are not generally useful for clinical TCD evaluations, since accurate vessel diameter measurements are typically unavailable for TCD applications. However, tube diameter is accurately determined for experimental flow phantom testing and $\hat{q}[n]$ can be used to validate TCD velocimetry data against conventional in-line flowmetry techniques.

The spectral mean Doppler frequency $\bar{f}_d[n]$ was established in the analysis of velocity estimation as a primary variable of interest. However, use of $\bar{f}_d[n]$ is only formally valid under a narrow set of demanding conditions [67]:

1. There are no vascular bruits or vessel wall movements.

2. The signal to noise ratio is sufficiently high.

3. The sample volume is centered on a straight segment of the artery.

4. There are no branches or adjacent small vessels within the sample volume.

5. There is minimal beam pattern variation over the cross-section of the vessel.

In a clinical setting, most of these conditions are violated and the accuracy of velocity measurements is therefore severely degraded. Most TCD instrument designs and a majority of TCD researchers have chosen to use the Doppler spectral envelope $f_{d,\max}$ – the maximum frequency peak of the Doppler spectrum – as the relevant measurement parameter for a majority of TCD applications. The Doppler spectral envelope, and the related velocity envelope $v_{\max}$, generally corresponds to the velocity in the lumen centerline and, under laminar flow, is proportional to mean flow velocity. As previously noted, arterial blood flow is pulsatile in nature and is not entirely described by the Poiseuille relation. However, the small diameter of the cerebral vessels – relative to other major arteries – has a stabilizing effect on the velocity

profile and experimental results have validated the laminar flow approximation in the MCA [67].

Use of the Doppler spectral envelope markedly improves measurement accuracy as it is a less sensitive, more robust parameter than $\bar{f}_d[n]$. As long as some portion of the sample volume contains the location of maximal flow velocity for the vessel of interest and no other regions within the sample volume contain a scatterer axial velocity component greater than $v_{\max}$ (i.e., vessel of interest is the source of the largest velocity scatterers within the volume of insonation), velocity estimation using the spectral envelope remains accurate (assuming a known Doppler angle θ_D).

A hardware implementation of the velocity estimation procedure, and further practical challenges related to the method, can be found in Section 3.4.

Chapter 3

Transcranial Doppler Ultrasound System Design

The intended use of an ultrasound system places considerable constraints on system design aspects. This work addresses the development of transcranial Doppler (TCD) sonography instrumentation, particularly for middle cerebral artery (MCA) insonation. The design of electrical hardware and transducer geometries must therefore consider factors relevant to TCD velocimetry, specifically vascular anatomy, cranial windows, typical blood flow velocities, TCD examination and vessel identification techniques, spectral analysis, and signal processing limitations.

3.1 Anatomical and Physiological Considerations

3.1.1 Cerebral Vasculature

Brain tissue is fundamentally reliant on uninterrupted and sufficient oxygenation. Blood flow requirements for the brain, relative to other organs, are considerable. Under resting conditions, the brain accounts for almost 20% of bodily oxygen demands [3, 79]. The cerebrovascular anatomy is composed of multiple redundancies, known as collaterals, such that adequate perfusion can many times be maintained in the event of inadequate flow through a single vascular route (e.g., due to blockage or

stenosis) [80].

The main anatomical structure of the cerebrovasculature is the Circle of Willis, as depicted in Figure 3-1:

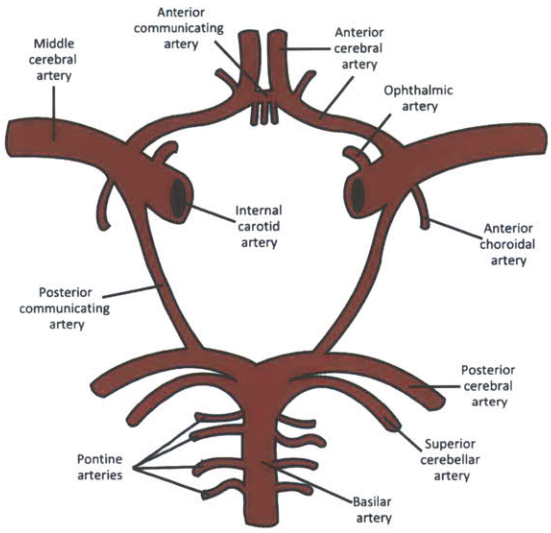

Figure 3-1: Anatomical structure of the cerebrovasculature [81]

The Circle of Willis is composed of the left and right branch pairs of the anterior cerebral artery (ACA), terminal internal carotid artery (TICA), posterior cerebral artery (PCA), posterior communicating artery (PCoA), middle cerebral artery (MCA), and the non-paired anterior communicating artery (ACoA), and basilar artery (BA). The TICA is the distal segment of the supraclinoid internal carotid artery (ICA) just proximal to its bifurcation into the ACA and MCA. For each cerebral hemisphere, under standard anatomic configurations and non-pathologic conditions, the MCA and ACA are supplied by the ipsilateral ICA. The left and right PCAs are supplied by the BA and flow through the communicating vessels (i.e., ACoA and PCoA) is generally minimal. Anatomic variation of the cerebral vasculature is, however, extremely common and considerable. Studies have shown that a "normal" Circle of Willis occurs in only 18% to 54% of individuals [67,82,83]. Such anatomic variation – including vessel caliber, course, and origin – and knowledge of the most frequent deviations – must be recognized when identifying vessels during TCD evaluation.

The left and right MCAs – the primary vessels of interest for this work – supply

blood to the lateral surface of each cerebral hemisphere and carry the vast majority of blood leaving the Circle of Willis ($\approx 80\%$) [84]. From its origin as a continuation of the left or right TICA, the ipsilateral MCA courses laterally (i.e., away from the cerebral midline) and slightly anteriorly [67]. The proximal portion of the MCA, known as the M1 or sphenoidal segment, gives rise to numerous small lenticulostriate perforators and has a normal mean diameter of 2.5 to 3.8 mm and a mean length of 16.2 mm [85, 86]. The distal M1 segment furcates – typically a bi- or trifurcation – into the MCA M2 branches, which course 90° superiorly and posteriorly into the Sylvian fissure [67].

Cerebral blood flow velocity (CBFV) measurements are generally characterized by a set of clinically relevant parameters, particularly peak systolic velocity (PSV), end diastolic velocity (EDV), and time mean velocity (MV), as defined for a notional CBFV waveform in Figure 3-2. The time mean velocity carries the highest physiological significance as it most closely correlates with cerebral perfusion. Certain TCD applications – particularly intracranial pressure (ICP) estimation and assessment of cerebrovascular autoregulation – rely, however, on the complete time domain velocity waveform for adequate temporal resolution of cerebral hemodynamics. As noted in Section 2.4.2, flow velocity measurements in TCD sonography are typically referenced to the velocity envelope. Spectral distribution characteristics are sometimes used during the detection of turbulent flow [67].

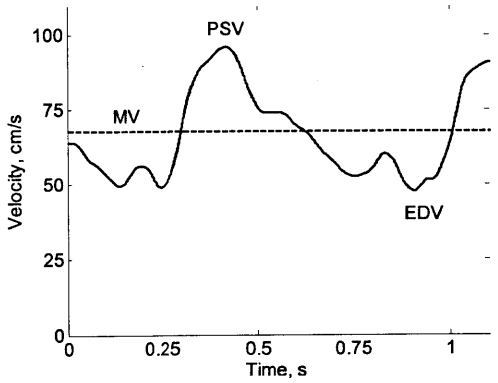

Figure 3-2: Velocity parameters PSV, EDV, and MV for notional CBFV waveform.

Table 3.1 gives typical dimension and flow velocity values for the M1 segment of the MCA in adult subjects.

Table 3.1: Summary of normal adult anatomical values and flow velocities for the M1 segment of the MCA [57,85,87].

Insonation Depth [mm]	Segment Length [mm]	Diameter [mm]	$\overline{MV} \pm \sigma_{MV}$ [cm/sec]	$\overline{PSV} \pm \sigma_{PSV}$ [cm/sec]	$\overline{EDV} \pm \sigma_{EDV}$ [cm/sec]
30 – 60	16.2	2.5 – 3.8	65 ± 17	94 ± 23	46 ± 12

Other derived parameters, such as pulsatility, have been examined in a variety of potential clinical uses. Pulsatility is a term used to describe the degree of variability in flow velocities throughout the cardiac cycle and is largely dependent, for a given vessel segment, on the resistance of more distal cerebral vessels. The Gosling pulsatility index (PI) is defined as:

$$PI = \frac{PSV - EDV}{MV} \tag{3.1}$$

Although PI can offer a degree of insight into the underlying vasculature and has been demonstrated as a rough indicator of ICP, cerebral perfusion pressure (CPP), and stenosis, it is often a poor clinical parameter for quantitative indication of pathology due to several confounding factors and is not sufficient for any particular diagnosis [88–90]. Within the M1 segment of the MCA, PI is normally in the range of 0.5 - 1.1 [67].

3.1.2 Cranial Acoustic Windows

Acoustic access to the intracranial cerebral vessels is facilitated by the occurrence of anatomical features – relative thinning of cranial bone or natural foramina – known as cranial acoustic windows [32]. In general, three primary cranial acoustic windows are used in TCD sonography: the transtemporal, transorbital, and transforaminal acoustic windows. Insonation of the MCA is normally accomplished through the transtemporal acoustic window (TAW), which will be considered in detail.

The TAW is located near the temple region and exists due to regions of thinning in the suprazygomatic portion of the temporal bone, which allows favorable transmission of acoustic energy at reduced attenuation. Despite the relative thinness of temporal bone within the TAW, considerable signal attenuation does occur, with attenuation extent being largely dependent on bone thickness. A patent TAW allows insonation of the ipsilateral TICA, ACA, MCA, PCA, ACoA, and PCoA under favorable anatomic conditions [91]. The TAW is further subdivided into four regions, known as the posterior, middle, anterior, and frontal temporal acoustic windows, as illustrated in Figure 3-3.

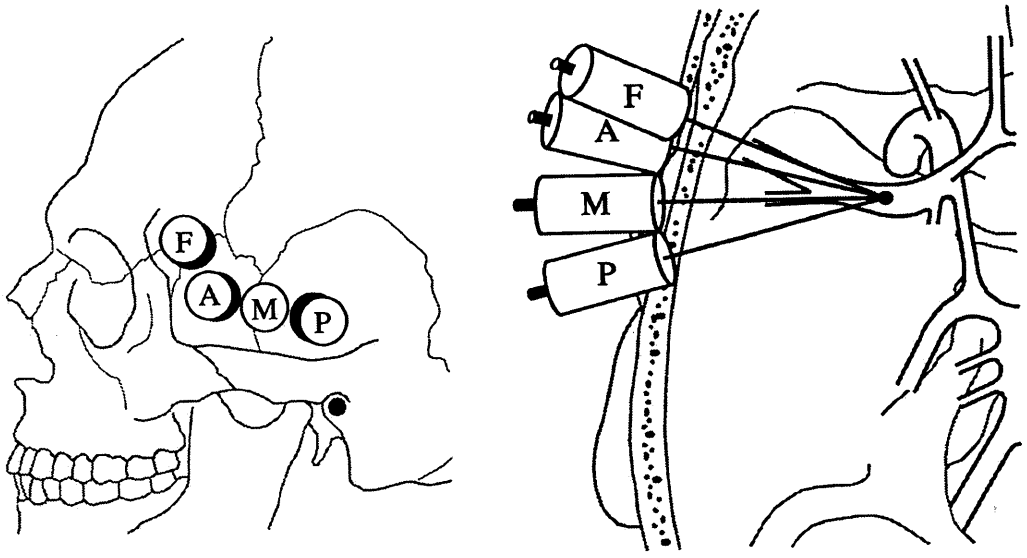

(a) Relative position of the transtemporal acoustic windows sideview.

(b) Window dependent transducer angulation.

Figure 3-3: Topview depiction of the location of the posterior (P), middle (M), anterior (A), and frontal (F) temporal acoustic window regions. From [67].

Significant variation occurs in the precise placement of patent TAW regions, therefore approximate locations as given. The posterior TAW, the TAW region with highest patency rates and the largest spatial separation of the anterior and posterior circulations, lies directly anterior to the external auditory meatus and slightly superior to the zygomatic arch [67]. The anterior TAW is roughly 3.0 cm anterior to the posterior TAW and slightly posterior to the frontal process of the zygomatic bone.

A middle TAW is located approximately midway between the posterior and anterior windows. Rarely, a frontal TAW – located just anterior to the pterion – is also used for transtemporal insonation [67]. Patent acoustic window regions are often fairly small and lateral movement of the transducer by a few millimeters can greatly degrade received Doppler signal levels [57]. The middle and anterior TAWs can generally achieve insonation of the MCA with the transducer lying relatively flat against the skin surface and result in a Doppler angle θ_D of nearly 0°. The posterior TAW often requires anterior and superior beam angulation to achieve insonation of the MCA.

The transmission of focused acoustic propagation through temporal bone has been studied experimentally by Grolimund in *ex vivo* skulls [57]. Although analytical propagation models are beneficial in understanding opposing design goals within an ultrasound system, experimentation is the only suitable means of obtaining an accurate depiction of tissue propagation losses due to a wide variability in cranial bone properties. The Grolimund experiments employed a 16 mm diameter circular transducer operating at 2 MHz and used hydrophone measurements to determine receive intensities and beam distortions following transmission through *ex vivo* skulls at the optimal temporal window (defined by the thinnest section of temporal bone). Receive intensities and beam patterns were compared to transmission characteristics in the absence of inhomogenieties (i.e., homogeneous water medium). The degree of beam distortion due to refraction was shown to depend highly on the variation of thickness within the cranial bone adjacent to the transducer. Due to irregular thickness variations, observed refraction effects cannot be corrected by physical transducer surfaces or lens structures. In the presence of cranial bone, the mean change in intensity of the transmitted acoustic wave at the thinnest temporal bone section was -7 dB (i.e., 80% intensity reduction). Pulse-echo operation is therefore expected to attain a reduction on the order of 14 to 20 dB in acoustic intensity due to the attenuative, reflective, and refractive effects of cranial bone.

A primary obstacle associated with TCD examination is the inability to obtain a detectable received Doppler signal in approximately 5 – 10% of patients due to the lack of a patent acoustic window, unusual vessel position, or excessive vessel

tortuosity [4,5]. The absence of a suitable TAW for MCA insonation was observed in 8.2% of individuals in a validation study (occurring in 5.0% of subjects monolaterally and 3.2% of subjects bilaterally) [32]. Lack of a satisfactory TAW is inherently related to increased temporal squama thickness, which has a mean value of 3.5 mm at its thinnest region, and is notably more prevalent in non-white races and females (12.1% TAW absence in females, 5.6% TAW absence in males) [92].

TAW patency is further affected by a number of bone pathologies, including hyperostosis, which causes localized increases in cranial bone density and thickness [67]. Age has also been shown to have a significant influence on TAW patency, with 5.1% of patients under the age 65 lacking an acceptable TAW, as opposed to 14.1% of patients age 65 and older [32]. Age dependent effectiveness is a major concern for the clinical use of TCD sonography as rates of cerebrovascular disease increase in elderly populations. Ultrasonic contrast agents can be used to improve TAW patency by enhancing the effective scattering coefficient of blood, but invasive administration – requiring intravenous injection – and significantly lower cavitational thresholds thereby complicate the evaluation process and create additional safety concerns [28,33]. The use of ultrasonic contrast agents is not considered for this work.

Transducer arrays, by employing timing delays, can dynamically achieve non-physically realizable apertures and are thereby well suited for phase-correction techniques, which are used to restore coherence at the focal point following refraction and aberration induced beam degradation [93]. By utilizing hydrophone-assisted phase-correction (i.e., adjustment of excitation phases based on hydrophone measurements when inhomogenieties are present) on *ex vivo* skulls for a phased array operating at an excitation frequency of 0.74 MHz, Clement and Hynynen were able to attain pronounced improvements to beam pattern definition and focal intensity as compared to uncalibrated focusing for the same acoustic output power [36].

Although hydrophone-assisted techniques are not applicable for *in vivo* measurements, they validate the utility of phase-correction methods. For pulse-echo operation, phase-correction techniques can conceivably incorporate received Doppler signal strength – and other acoustically measured parameters – into phase-correction algo-

rithms to achieve *in vivo* focal restoration using iterative optimization procedures or machine learning methods. Such developments will be considered in future extensions of this work, but are not presently discussed further.

3.2 TCD Examination Techniques

Although this work seeks to achieve autonomous measurement of CBFV in the MCA, a discussion of conventional manually steered TCD examination techniques is critical to recognizing the subtleties associated with clinical TCD evaluation. Developments in transcranial sonography have enabled transcranial ultrasound imaging (e.g., transcranial color-coded duplex sonography), which allow some delineation of intracranial structure, but – due to the distortion effects of cranial bone – generally result in poor resolution and limited clinical imaging utility [4]. Although imaging modalities can facilitate vessel location, significant knowledge of the cerebral anatomy and limitations of velocimetry are still necessary to obtain accurate CBFV measurements. The traditional "blind" (i.e., non-imaging) approach to TCD examination will therefore be presented.

Conventional TCD examination techniques are initially difficult to learn and can often be demanding to perform, even for experienced operators. Challenges associated with TCD evaluation are further exaggerated in subjects with marginal acoustic windows and in pathological conditions in which the assumption of normal flow velocities and directions may no longer be valid. The experienced sonographer must rely on proficient examination techniques to spatially position and angle the transducer, adjust the sample gate depth, and identify the source Doppler spectra (i.e., intracranial vessel identification).

The reliability of TCD velocimetry data is highly operator dependent. Measurement accuracy is primarily related to operator experience, with measurement error being lowest in highly-trained, well-practiced sonographers [23]. Accurate TCD examinations require considerable training, manual dexterity, and adequate knowledge of the underlying cerebral anatomy. The addition of technological innovations and

usability enhancements to TCD systems – including automatic vessel tracking and power motion-mode Doppler (PMD) operation – seeks to reduce necessary operator expertise and improve measurement reliability.

The TCD examination methods discussed initially in this work apply to a single element, manually steered transducer. These approaches will be extended to incorporate the use of transducer arrays, electronic beam steering, and other characteristics of the wearable TCD systems under development. Clinical TCD evaluations are generally thorough in nature and include flow velocity measurements for the entire cerebrovasculature through all acoustic windows. For this work, however, insonation of the left and right MCAs through the TAWs is considered exclusively.

3.2.1 Examination Procedure

The TCD examination procedure introduced by Aaslid has been adopted by researchers as the standard method for CBFV measurements at the basal cerebral arteries [2,57]. The introduction of PMD has considerably altered the TCD examination procedure, which is presented here in modified form [26,27,94]. PMD facilitates localization of cranial windows and guides the selection of range gate depth. PMD simultaneously displays flow signal intensity and direction over a wide range of insonation depths and expedites vessel location through visualization rather than via the auditory Doppler cues required by earlier TCD systems [27]. PMD also enables improved vessel identification by enabling a visual display of vessel depth extent.

Figure 3-4 depicts measured TCD sonography data from a commercial TCD system (ST3 PMD150, Spencer Technologies, Seattle, WA), where the power motion-mode data is presented in the upper half of the display and the Doppler sonogram (described in Section 3.4) is presented in the lower half. Within the PMD display, red indicates flow toward the transducer, while blue indicates flow away from the transducer. Color intensity characterizes the extent of moving scatterers at a particular depth within the insonation region, corresponding to the number of insonated erythrocytes. PMD data is displayed relative to time (i.e., x-axis of PMD display), which enables transient scattering phenomena – particularly circulating cerebral em-

boli – to be captured visually. The Doppler range gate depth is shown in Figure 3-4 as a yellow horizontal line positioned at an insonation depth of 50 mm.

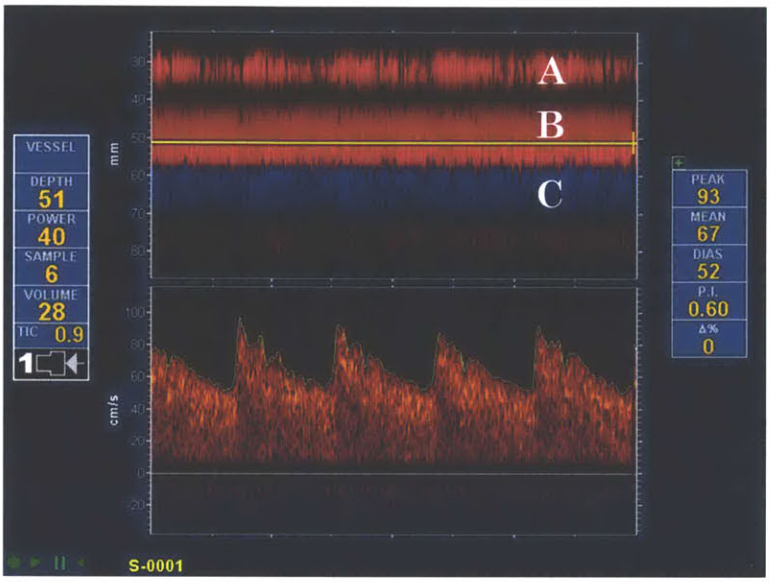

Figure 3-4: Examination of the cerebral vessels with PMD during right transtemporal insonation: right M2 MCA (A); right M1 MCA (B); right ACA (C).

Conventional single element and imaging TCD evaluations must be performed on stationary patients in a supine or sitting position, with adequate time allowed for stabilization of the subject's heart rate and blood pressure. To ensure sufficient acoustical coupling to tissue, an ample amount of ultrasound gel should be applied to the transducer surface prior to contact with the subject. A PMD insonation range of $\approx$ 20 to 70 mm and moderate output power, $< 50\%$ maximum power or equivalently $I_{SPTA} < 250\,\mathrm{mW/cm^2}$, should be selected. The transducer is then applied to the posterior TAW region, maintaining slightly upward and anterior probe angulation.

Minimal force should be used to position and angle the transducer since substantial forces may cause patient discomfort and drive ultrasound gel away from the transducer surface. If no flow signals appear within the PMD display, the transducer is advanced in slow circular movements toward the anterior TAW region, changing probe angulation throughout the motion. All three common TAW regions (i.e., posterior, middle, and anterior TAWs) should be explored. For insonation of the MCA, the

transducer should be maneuvered until a maximal extent of PMD display intensities between approximate depths of 30 – 60 mm is achieved, corresponding to a relatively straight section of the MCA M1 segment. If no Doppler signal is attainable or if the signal remains faint upon positioning optimization, the acoustic output power setting can be incrementally increased until an adequate Doppler signal is obtained or the maximum output power level is reached. If a Doppler signal is still absent at maximum output power, the patient is said to have a nonpatent temporal acoustic window.

Once the optimal TAW region has been identified, the operator attempts to maximize PMD intensity for the expected range of MCA depths through utilization of fine motor skills to incrementally adjust transducer position and angle. Transducer positioning must often be continually optimized throughout the measurement process due to slight misalignments cause by subject or operator movement. The Doppler range gate depth is then adjusted to the center of a contiguous, high intensity PMD segment within the MCA depth range to achieve Doppler velocimetry information [26]. Following TAW examination and the detection of Doppler flow velocities, emphasis of the TCD examination shifts toward identifying the Doppler signal source (i.e., the insonated vessel).

3.2.2 Vessel Identification

In addition to operator inexperience, a primary obstacle in accurate vessel identification is vast anatomical variance in cerebrovasculature structure, including variations in vessel caliber, course, and even origin.

For transtemporal insonation, five salient measurement features are typically employed during vessel identification [67]:

1. Sample volume depth and angulation.

2. Direction of flow.

3. Spatial relation of sample volume to intracranial landmarks (e.g., bifurcation of the TICA into the ACA and MCA).

4. Relative flow velocity, with highest flow velocities typically observed in the MCA and ACA.

5. Response to ipsilateral common carotid artery compression or oscillations.

The MCA – along with its branches – is normally the only vessel perceptible from the TAW using TCD sonography between insonation depths of 25–50 mm [57]. Flow direction of the ipsilateral MCA is generally toward the transducer, which is also observed for the PCA. To distinguish the MCA from the PCA, it is useful to trace the MCA extent with increasing depth to the TICA bifurcation, which is identified by bidirectional flow at an insonation depth of 55–65 mm. MCA flow velocities are typically slightly larger than those obtained at the ACA and are generally at least 25% larger than PCA flow velocities. Finally, upon compression of the ipsilateral common carotid artery under normal cerebrovascular anatomy, flow in the MCA and ACA is temporarily obliterated or severely diminished while flow in the PCA is relatively unaffected.

The PCoA and ACoA are not generally detectable using TCD sonography unless a pathological condition exists, resulting in significant collateral flow. Vessel identification features are summarized for the major intracranial vessels in Table 3.2. The reliability of vessel identification techniques varies among the intracranial vessels, with the highest accuracy of identification occurring for the ipsilateral MCA.

It is customary to assume that Doppler angle $\theta_D \approx 0°$ when performing non-imaging TCD examinations because the exact angle between the ultrasound beam and intracranial vessel segment is unknown. For MCA insonation, the Doppler angle θ_D is generally $< 20°$, resulting in a maximum underestimation of $\approx 6\%$. For clinical applications, it is therefore generally not necessary to account for Doppler angle in transtemporal MCA insonation because it is sufficiently small to permit determination of absolute flow velocity.

Table 3.2: Summary of vessel identification criteria. Adapted from [57, 67].

Artery [Segment]	Sample Volume Depth [mm]	Flow Direction	$\overline{MV} \pm \sigma_{MV}$ [cm/sec]	Compression Response
MCA [M1]	30–60	Toward	65 ± 17	Obliteration, Diminishment
ACA [A1]	60–80	Away	50 ± 11	Obliteration, Diminishment, Reversal
PCA [P1]	60–70	Toward	36 ± 10	No Change
PCA [P2]	60–70	Away	40 ± 10	No Change
TICA	55–65	Toward	39 ± 9	Obliteration, Reversal

TCD examinations commonly include bilateral evaluation. The methods described above are valid for left and right transtemporal insonation. Although the cerebrovasculature is ostensibly equivalent from either side, moderate differences in velocimetry data for the contralateral vessel often occur, especially in the presence of pathology. Differences from the left and right hemispheres should not be considered abnormal unless they exceed 30% [95].

During prolonged TCD monitoring, a headframe can be employed to hold the transducer in position after an acceptable Doppler signal is obtained. Patient movement and environment dynamics can, however, cause probe misalignment and a consequent degradation in Doppler signal strength. The frequency of probe displacement effects is highly dependent on measurement application, being more problematic in prolonged evaluation of non-comatose patients. The transducer position and angulation must therefore be regularly optimized to ensure adequate alignment and measurement accuracy [24].

3.3 Safety Considerations

Although diagnostic ultrasound is a generally safe measurement modality, analysis of acoustic bioeffects should be considered to ensure safe and effective use. Various governmental and professional standards, particularly from the United States Food and Drug Administration (FDA), American Institute of Ultrasound in Medicine (AIUM), and British Medical Ultrasound Society (BMUS), have been established to quantify safe operating regimes and thereby limit the potential of patient harm [96–98].

Safety guidelines are particularly meaningful for the continuous TCD monitoring applications of this work, due to prolonged examination duration, high acoustic absorption in bone, and the relatively high acoustic output powers necessary (in some cases) to achieve adequate insonation of the intracranial vessels. Ultrasound induced bioeffects can be broadly divided into thermal and non-thermal categories. Specific limits exist for each phenomenon and potential for tissue damage is expected only when ultrasound exposure thresholds are exceeded.

Thermal effects (i.e., tissue heating) are related to the conversion of acoustic energy into heat and are therefore dependent on time averaged intensity measures and tissue absorption factors. The thermal index is used to predict the rise of tissue temperature in °C under worst case conditions. For transcranial applications, the relevant thermal parameter is the thermal cranial index TIC, since there is bone at the tissue surface [28]. Heating of cranial bone due to absorption can potentially lead to secondary heating of adjacent brain tissue via head conduction. The AIUM and BMUS recommend limiting $TIC < 2.0$ [37].

The TIC is directly related to acoustic power and can be expressed as:

$$TIC = \frac{W_0}{8}\sqrt{\frac{\pi}{A_{\text{ap}}}} \tag{3.2}$$

where W_0 is time averaged acoustic source power (measured in W) and A_{ap} is the active aperture area (measured in m^2).

Neglecting apodization, time averaged acoustic output power W_0 can be deter-

mined for a given excitation waveform by the expression:

$$W_0 = A_{ap}\frac{p_0^2}{2Z}\frac{MT_e}{T_{PRP}} \tag{3.3}$$

where p_0 is the surface pressure amplitude (assuming gated sinusoidal excitation).

Nonthermal effects – primarily cavitation (i.e., collapse of gas bubbles within the medium) and acoustic streaming (i.e., steady fluid current due to nonlinear absorption) – are influenced by peak rarefaction pressures within the acoustic field. Nonthermal effects are characterized by a mechanical index (MI), an attempt to indicate the probability of mechanical damage in a non-thermal process, is given by [96]:

$$MI = \frac{p_{rar,max}}{1000\sqrt{f_e}} \tag{3.4}$$

where $p_{rar,max}$ is the derated (i.e., accounting for soft tissue attenuation) spatiotemporal peak rarefactional pressure (measured in Pa) and f_e is the excitation frequency (measured in Hz). Safety guidelines suggest, in the absence of ultrasound contrast agents (not considered in this work), that $MI < 1.9$ [96]. Using a typical 2 MHz excitation frequency, this results in a maximum rarefactional pressure of 2.7 MPa (neglecting derating). For most TCD applications, TIC is a more restricting limitation and operational MI values are considerably below their threshold values. Because the MI is computed without accounting for the significant attenuating effects of cranial bone, *in situ* MI values can be expected in practice to be considerably reduced.

FDA guidelines also limit the spatial peak temporal averaged intensity I_{SPTA} (as defined in Section 2.1) for diagnostic ultrasound uses to $< 720\text{mW/cm}^2$ (for devices following the output display standard) [96]. The I_{SPTA} is dependent on spatial speak pressures – influenced primarily by transducer characteristics and HV supply levels – and also by relative temporal extent of the excitation waveform to the pulse repetition period. As with MI, I_{SPTA} constraints are not typically a limiting factor for diagnostic operation.

A basis of ultrasound safety is prudent use of the ALARA principle (i.e., "as low as reasonably achievable"). This principle states that acoustic output power should

always be the minimal level necessary to achieve optimal diagnostic information. The ALARA principle is utilized in TCD evaluations by the initial use of moderate power levels during cranial window location. If adequate Doppler signals cannot be obtained, the operator increases acoustic output power levels toward their limiting values and repeats the vessel location procedure. In accordance with the ALARA principle, once the optimal cranial window is localized and a sufficient Doppler signal obtained during examination, acoustic output power should be reduced to the minimal level achievable without discernible degradation to Doppler signal fidelity.

The safety index models described here do not account for duration of exposure. As ultrasound monitoring paradigms shift – especially with the development of wearable ultrasound systems for prolonged monitoring – exposure standards may adapt to account for modified use cases. Because ultrasound exposure guidelines do not yet exist for extended monitoring, a conservative interpretation of the current standards will instead be accepted. Such interpretation is commiserate with existing commercial TCD systems, which can be used in nonambulatory continuous monitoring [94].

Maximum acoustic index values for the prototype TCD systems developed in this work are given in Table 3.3.

Table 3.3: Prototype TCD system maximum global acoustic indices.

Parameter	Accepted Safe Limit	Prototype Device Limit
TIC	< 2.0	< 1.5
MI	< 1.9	< 0.7
I_{SPTA}	< 720 mW/cm^2	< 500 mW/cm^2

3.4 Doppler Processing Algorithm

Signal processing is necessary to condition the received radio frequency (RF) waveform and transform it into meaningful velocimetry data. Early PW Doppler systems utilized considerable analog circuitry to achieve signal processing [99]. Developments

in digital electronics and signal processing, however, have enabled the practical realization of robust and configurable processing schemes, primarily based in software.

The velocity estimation procedure presented in Section 2.4.2 was highly simplified for analytical tractability – neglecting absolute signal levels, noise effects, analog-to-digital conversion, and Fourier transform implementation. A practical velocity estimation signal processing scheme used throughout this work is presented in Figure 3-5, where G_{AFE} is the analog front end (AFE) amplifier gain, T_{ADC} is the analog-to-digital converter (ADC) sampling period, $w[n]$ is a windowing sequence, M is a decimation factor, and FFT is the fast Fourier transform operation. Alternative velocity estimation methods are often used, especially in distinct applications like color flow imaging, and are described in [40,43].

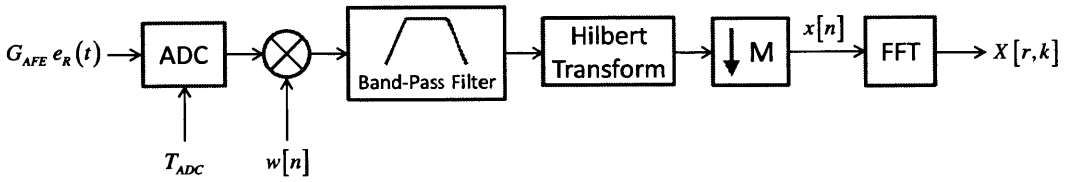

Figure 3-5: Velocity estimation signal processing block diagram.

The windowing sequence $w[n]$ is used to segment the sampled data into fixed length sequences. A decrease in window sequence length results in finer temporal resolution, but also yields spreading of the Doppler spectrum – a phenomenon known as spectral broadening. By evaluating expected time-variation and frequency content in realistic CBFV waveforms, a sufficient balance between time and spectral resolution can be achieved through selection of $w[n]$ length, denoted N_w.

Matched filtering is used subsequent to windowing to limit out of band noise and interferers, thereby increasing the signal-to-noise ratio (SNR). The SNR of the received signal after filtering is theoretically maximized when the filter transfer function is matched to the spectral content of the received signal. An optimal matched filter can be implemented by defining the filter impulse response $h_{bp}[n]$ as the underlying pulse excitation basis function $e_{T0}(t)$ sampled at T_{ADC}. Neglecting frequency dependent attenuation and transducer bandwidth effects, the spectral envelope of the

received signal is therefore approximately equivalent to the band-pass filter transfer function and SNR is maximal.

Use of the Hilbert transform is necessary in Doppler processing to generate an analytic signal (i.e., a complex valued signal composed of in-phase and quadrature data) from the real valued receive sequence. In general, the spectral content of an analytic signal no longer results in a symmetric distribution about the frequency axis and thereby enables differentiation between forward and reverse flow velocities.

Formally, the Hilbert transform is defined in the time domain as [61]:

$$h_{HT}[n] = \begin{cases} \frac{2}{\pi}\frac{\sin^2(\pi n/2)}{n}, & n \neq 0 \\ 0, & n = 0 \end{cases} \tag{3.5}$$

The frequency domain definition of the Hilbert transform, however, generally offers additional insight:

$$H_{HT}(\omega) = \begin{cases} e^{+\jmath\pi/2}, & -\pi < \omega < 0 \\ e^{-\jmath\pi/2}, & 0 < \omega < \pi \\ 0, & \omega = -\pi,\ 0,\ \pi \end{cases} \tag{3.6}$$

The Hilbert transform in effect implements a 90° phase shift to achieve in-phase $y_I[n]$ (i.e., original real valued signal) and quadrature $y_Q[n] = y_I[n] * h_{HT}[n]$ signals. The analytic signal output of the Hilbert transform processing block is then formed as $y_{HT}[n] = y_I[n] + \jmath y_Q[n]$.

The obscuring of flow direction can be seen in Figure 3-6, where a receive signal due to forward flow (i.e., toward the transducer) results in a dual-sided spectrum in the left plot prior to complex manipulation and a single-sided spectrum – corresponding only to forward flow – in the right plot after generation of the analytic signal via Hilbert transform.

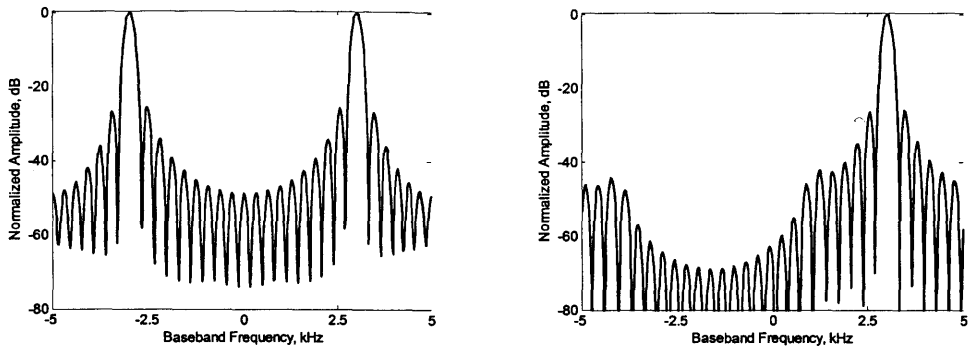

(a) Dual-sided receive signal spectrum prior to Hilbert transform.

(b) Single-sided receive signal spectrum following the Hilbert transform.

Figure 3-6: The effects of analytic signal generation on the differentiation of receive signal flow directions.

The baseband signal $x[n]$ is obtained via decimation by $M = \frac{T_{PRP}}{T_{ADC}}$. Due to the decimation factor relationship, the receive signal is consequently sampled at T_{PRP}. Because energy still exists over a wide spectral range, significant aliasing occurs during decimation. Such aliasing does not, however, degrade the baseband signal as it results in reinforcement of the main tone – and corresponding Doppler information – by the secondary tones and equivalent Doppler content. Prior to decimation, the sequence should be shifted by the sample offset T_s, such that the baseband samples correspond to scatterer interactions within the sample volume, centered at the sample depth z_s .

The FFT is used to implement the discrete Fourier transform, which allows computation of the processed receive sequence spectral content – and therefore the velocity distribution of the scatterer ensemble. Characteristics of the frequency spectra are highly influenced by window sequence length and an N_w-point FFT is generally taken to compute spectral content – since, beyond N_w, higher-order transforms do not improve spectral resolution. A 64-point transform yields $< 2\%$ full-scale velocity resolution, which is generally adequate for clinical TCD applications. Temporal resolution can be improved to a degree by overlapping data segments, rather than using adjacent segments.

Time varying spectral information is visually presented using the sonogram, which

depicts the Doppler spectral power within individual frequency bins – nominally the relative number of scatterers traveling at a corresponding velocity range – for a each time segment by a gray scale intensity (or color). Assuming uniform insonation of the vessel cross-section, the approximate spatial distribution of velocities across the vessel lumen can therefore be visualized as shown in Figure 3-7.

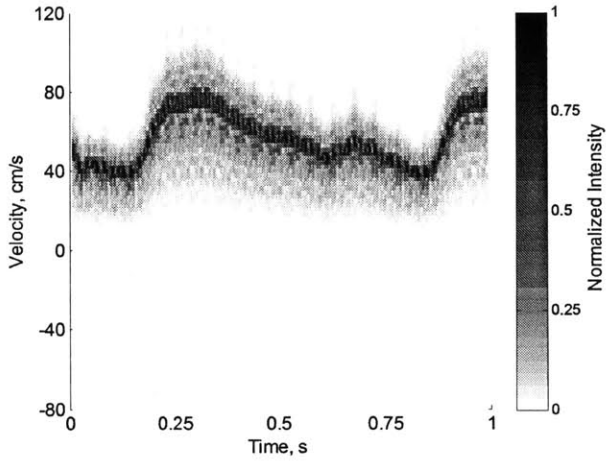

Figure 3-7: Sonogram display of a notional Doppler signal.

Using an ultrasound field solver (Field II, Technical University of Denmark, Lyngby, Denmark) to obtain RF receive data from a time-varying distribution of scatterers, the velocity estimation algorithm can be implemented in MATLAB (MathWorks, Natick, MA) for validation and parameter evaluation [38, 39]. The simulation of a realistic CBFV waveform – shown in Figure 3-8 – demonstrates excellent agreement between the estimated and actual mean scatterer velocity, resulting in a normalized root-mean-square error of $< 5\%$. From simulation data, a 128-point FFT (i.e., $N_w = 128$) using 87.5% overlap was found to yield the highest accuracy velocity estimates, which will be used for TCD hardware implementation.

Although simulated velocity estimation yielded outstanding results, it is important to note that several critical physical effects are not present. Excessive acoustic absorption within the cranial bone results in a highly attenuated receive signal and therefore noise is a critical aspect in the design and operation of TCD instrumentation. As indicated in Section 2.1.1, scattering from stationary tissue tends to dominate the

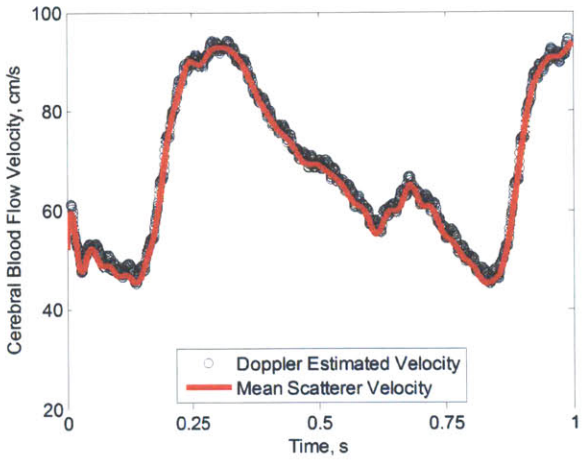

Figure 3-8: Comparison of simulated velocity estimation and simulation scatterer velocity parameter.

receive signal spectrum. Practical systems therefore also need to incorporate sharp high-pass filtering of the baseband signal, often referred to as the wall or clutter filter, to attenuate the high amplitude stationary reflections (i.e., spectral content at or near DC) prior to computation of the FFT.

PMD operation is simply accomplished by computing an array of decimated waveforms at finely spaced sample depths (e.g., 2 mm) across a range of depths. Each resulting waveform must then be passed through a clutter filter to remove effects from stationary scatterers. The total integrated Doppler energy at each sample depth thereby corresponds to the PMD intensity, with predominately negative Doppler frequency content resulting in blue colored regions and predominately positive Doppler frequency content resulting in red colored regions.

3.5 System Architecture

The hardware developments within this work utilize discrete, commercially-available circuit components. This approach places considerable restrictions on feasible system architectures, since access to internal nodes and diversity in component configurations is minimal. A capable and robust system architecture is presented in Figure 3-9. The

selected architecture is, however, considerably hardware inefficient, which leads to increased power dissipation, system dimensions, and complexity.

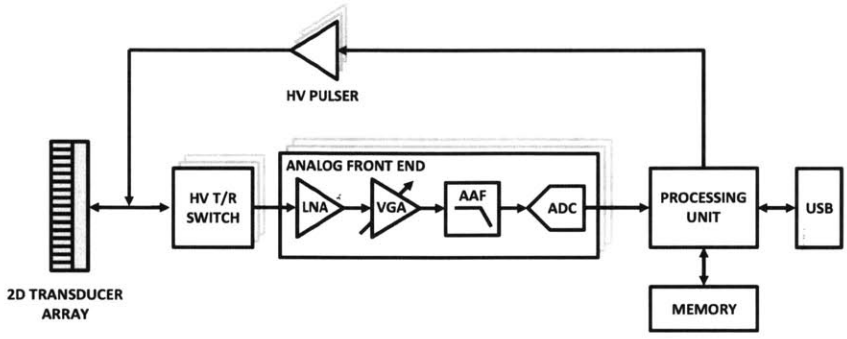

Figure 3-9: System architecture block diagram for prototype TCD instrumentation.

Pulse excitation waveforms are generated in the processing unit and are relayed to each independent high-voltage (HV) pulser channel. The HV pulsers transform digital excitation waveforms into HV transmit pulses. Within the transducer array, each element is connected to a HV pulser channel. The piezoelectric transducer elements convert the HV transmit pulses into acoustic energy, which is radiated into the propagating medium. During transmit, the HV transmit/receive (T/R) switches – one per transducer element – are open to protect sensitive receive electronics from HV signals.

During receive mode, acoustic energy is converted into a low-level electrical signal at each transducer element. The HV T/R switches close, providing a path to the low noise amplifier (LNA) of the AFE, with one AFE per transducer element. A variable gain amplifier (VGA) further amplifies the receive signals such that signal levels are within the ADC operating range. An anti-aliasing filter (AAF) is used to low-pass filter the signal so that spectral content beyond the Nyquist frequency does result in aliasing. The analog signals are then digitized and the resulting bitstreams are sent to the processing unit. Receive beamforming is achieved in post-processing through simple delay and sum methods (i.e., time delaying each channel and adding the resulting outputs). Data can be further manipulated within the processing unit to obtain velocity estimation, stored to memory, or transferred to a computer via

USB for data collection and further analysis.

3.6 Electrical Hardware Implementation

This work describes the design of a first-generation prototype TCD system. Prototype I is an eight channel system that has been fabricated and experimentally tested and is described in detail below. Although the Prototype I system allows for multi-channel operation, it has only been tested with a single element transducer since a transducer array was not yet available. The design of a 64 channel (i.e., 8x8 elements) transducer array for future higher channel count TCD system implementations is presented in Section 3.7.

The Prototype I printed circuit board (PCB) device consists of interconnected circuit components, which can be classified as:

- Power management circuits
- Field programmable gate array (FPGA)
- Universal serial bus (USB) to universal asynchronous receiver transmitter (UART) controller
- High voltage (HV) pulsers
- Transmit/receive (T/R) switches
- Analog front end (AFE) circuits
- Clock generation circuits

A block diagram of the electrical hardware implementation is given in Figure 3-10.

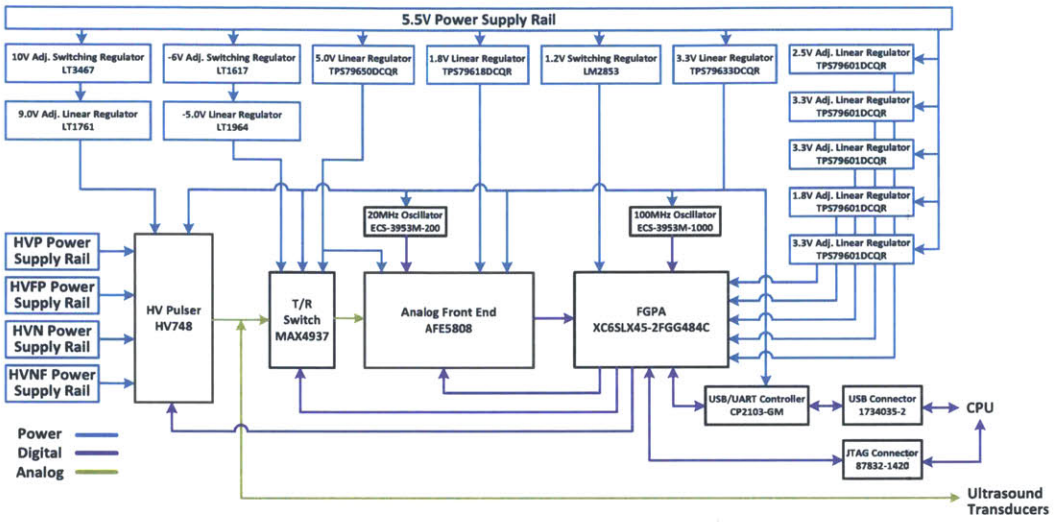

Figure 3-10: Block diagram of the electrical hardware implementation.

The power management circuits consist of a set of linear and switching regulators. The linear regulators – LT1761 and LT1964 (Linear Technologies, Milpitas, CA), TPS79650DCQR, TPS79618DCQR, and TPS79633DCQR (Texas Instruments, Dallas, TX) – are used to provide a constant operating voltage to electrical components. Separate adjustable linear regulators – TPS79601DCQR (Texas Instruments, Dallas, TX) – are employed on the FPGA input/output supplies to allow adjustment of FPGA output voltages, which are initially required to drive peripheral debugging circuitry.

Switching regulators – LT3467 and LT1617 (Linear Technologies, Milpitas, CA) and LM2853 (Texas Instruments, Dallas, TX) – are utilized to increase supply voltages, invert supply voltages, and power-efficiently convert to low supply voltages, respectively. All regulators are powered from a 5.5V supply rail using an external DC power supply. The HV power supply output voltage levels (i.e., HVP, HVFP, HVN, HVFN) are set using external DC power supplies. Irrespective of transducer dependencies, the HV supply voltage levels are limited to HVP < 60V, HVPF < 50V, HVN < -60V, HVNF < -50V.

The FPGA (XC6SLX45-2FGG484C, Xilinx, San Jose, CA) acts as an embedded processing and control unit within the TCD ultrasound system and configures op-

erating parameters for the HV pulsers, T/R switches, and AFEs. Pulse excitation waveforms are generated in the FPGA and relayed to the HV pulsers. Digital echo data is received by the FPGA, which deserializes, digitally filters, and stores echo data. Data alignment of the deserializers is achieved on start-up using a calibration sequence for the AFE. The FPGA transmits captured echo data via USB – utilizing a USB/UART controller (CP2103-GM, Silicon Laboratories, Austin, TX) and mini-USB connector (1734035-2, TE Connectivity, Berwyn, PA) – to a computer for further data processing and analysis. A Joint Test Action Group – known commonly as JTAG – connector (87832-1420, Molex, Lisle, IL) interfaces the FPGA to an external computer based programming file for configuration of the FPGA hardware. High level control of the FPGA timc sequencing is achieved by implementing a Picoblaze microcontroller within the FPGA fabric. The use of a microcontroller allows the abstraction of FPGA tasks into an assembly language.

The HV pulsers (HV748, Supertex, Sunnyvale, CA) level shift digital excitation pulses from low-voltage FPGA outputs to the HV supply rails (i.e., HVP and HVN) for each transducer element. The driving strength (i.e., maximum output current, of the HV pulsers is set through configuration bits via the FPGA. Because all HV pulser channels operate at common HV rails (i.e., HVP and HVN), transmit apodization cannot be accomplished using this architecture.

A T/R switch component (MAX4937, Maxim Integrated, San Jose, CA) protects sensitive receive electronics from high level transmit voltages, since both the HV pulser and AFE are connected to the same transducer line. The FPGA uses a serial peripheral interface bus (SPI) to control T/R switch gating to synchronize switch operation with the other system components.

The AFE (AFE5808, Texas Instruments, Dallas, TX) includes analog LNA, variable attenuation, programmable gain, AAF, and ADC circuit blocks. The gain, filtering, and ADC parameters are configured for application specific functionality via an SPI interface from the FPGA. Analog gain blocks help to limit noise contributions and achieve sufficient signal levels prior to digitization. Programmable analog gain control enables a wide range of achievable system gains, from -4 to $+54$ dB.

Low-pass filtering – via AAF blocks – attenuates high frequency interferers such that frequency aliasing is minimized during data conversion. Apodization can be achieved on receive under this hardware architecture through adjustment of analog gains or by scaling of individual channel data prior to summation. The ADC transforms the analog signal into a 14-bit, serialized low-voltage differential signaling (LVDS) waveform for each channel. The LVDS bitstream is transferred to the FPGA, which deserializes the bitstream for further processing.

The clock generation circuits consist primarily of the 100MHz FPGA oscillator (ECS-3953M-1000, ECS, Olathe, KS) and the 20MHz AFE sampling oscillator (ECS-3953M-200, ECS, Olathe, KS). Both oscillators provide a digital clock for timing of synchronous logic within each component. Additional clocks (e.g., SPI interface clock) are generated at lower speeds within the FPGA using clock divider logic and are therefore referenced to the FPGA clock. The FPGA and AFE clock domains are connected using a first-in, first-out (FIFO) memory structure with separate input and output clock domains within the FPGA.

Figure 3-11 shows the Prototype I PCB electrical hardware.

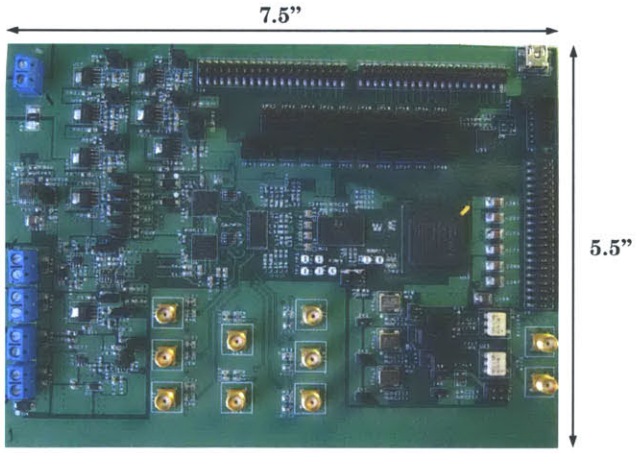

Figure 3-11: A picture of the electrical hardware of the Prototype I PCB.

The purpose of Prototype I is to validate the transmit and receive electronics, processor system control, and velocity estimation methods. A transducer array is not defined for the Prototype I system and instead a single element transducer is utilized

during operation. Throughout experimental validation of the Prototype I system, a $0.25'' \approx 6.4$ mm diameter flat circular transducer (C323-SU, Olympus, Waltham, MA) was used.

Figure 3-12 shows the complete Prototype I TCD ultrasound system, including all necessary peripherals for pulse-echo velocimetry operation.

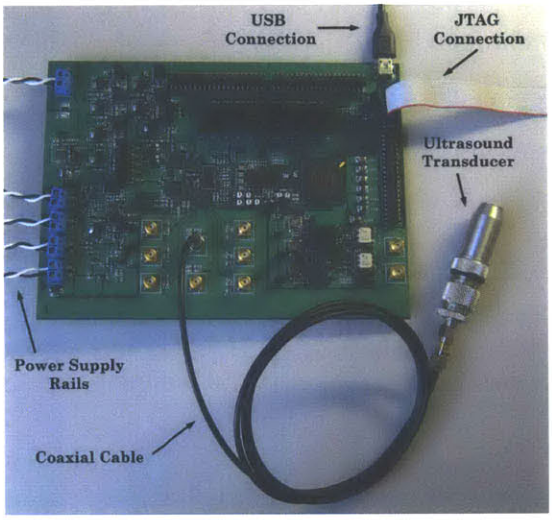

Figure 3-12: A picture of the operable Prototype I TCD ultrasound system.

3.7 Transducer Array Design

This section describes the 2D transducer array design for a future 64-channel (i.e., 8x8) TCD sonography system. Significant aperture constraints are necessary to achieve focusing at the required depths of interest for MCA insonation (30 – 60 mm). These aperture requirements can be achieved using larger transducer element dimensions. As elements become larger, however, directivity degrades and the formation of grating lobes can become problematic. For transtemporal insonation of the MCA, a required steering angle magnitude $< 15°$ is assumed (for both azimuth and elevation angles).

Using expressions from Section 2.2.4, suitable transducer element dimensions are computed as $L_x = L_y = 1.6$mm, $\text{kerf}_x = \text{kerf}_y = 0.1$mm, resulting in equivalent aperture dimensions $L_{x,eq} = L_{y,eq} = 13.5$ mm. Using equivalent aperture dimensions,

maximum focal length and maximum focused half-power spot width are determined:

$$l_{f,\max} \approx \frac{L_{x,eq}^2}{2.44\lambda} = 99.6\,\text{mm} \tag{3.7}$$

$$w_{x,3dB} = w_{y,3dB} = \frac{0.88\lambda l_{f,\max}}{L_{x,eq}} = 4.9\,\text{mm} \tag{3.8}$$

Analysis of the transducer array design indicates a maximum focal length well in excess of the required 60 mm maximum depth of interest for MCA insonation. Although not imperative for the velocity envelope (i.e., $v_{\max}$) method described in Section 2.4.2, relatively uniform vessel insonation is generally desired in velocimetry applications. A calculated half-power spot width of 4.9 mm is consistent with the expected MCA diameter of $\approx$ 3 mm.

Validation of this transducer array design is achieved by comparing simulated focal intensities for phased array operation to a single element transducer design (13 mm diameter, planar circular transducer) commonly used in commercial TCD instrumentation, for a constant output power [13,27].

Figures 3-13 and 3-14 depict the axial intensity dependence for the unfocused single element transducer and the phased array at focal depths of 30 mm and 60 mm, respectively. Acoustic intensity is normalized to the last axial maximum of the unfocused transducer.

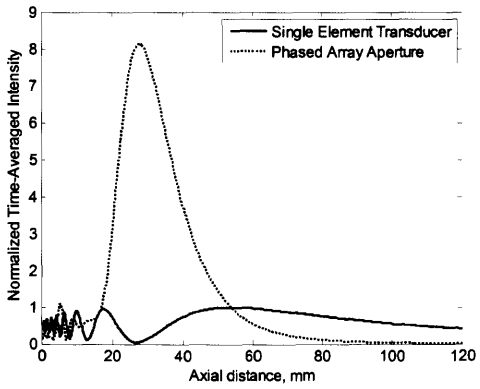

Figure 3-13: Comparison of acoustic intensity for single element and phased array transducers at a focal depth of 30 mm.

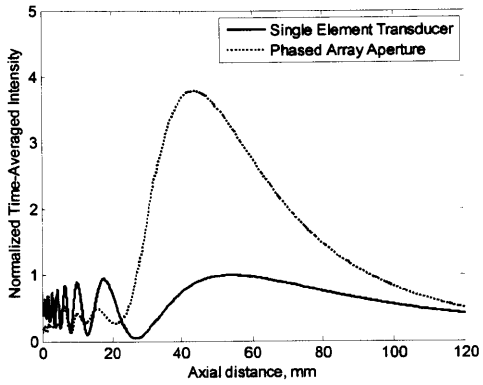

Figure 3-14: Comparison of acoustic intensity for single element and phased array transducers at a focal depth of 60 mm.

In the absence of steering, the phased array design achieves much higher on-axis acoustic intensities – via focusing – over the range expected insonation depths.

In cases where beam steering is required, the single element is manually angled and acoustic intensity along its steering axis is unaffected. By contrast, the phased array employs electronic beamformation to achieve steering, which yields reduced intensities for non-zero steering angles – due mainly to the limited directivity of its relatively large transducer elements. However, even at the most extreme expected steering angle (15°) and focal length (60 mm), the phased array still achieves increased acoustic intensity when compared to the manually steered, unfocused single element transducer, as shown in Figure 3-15.

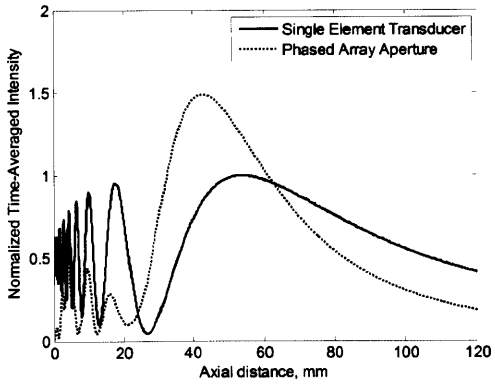

Figure 3-15: Comparison of acoustic intensity for single element and phased array transducers at a focal depth of 60mm and steering angle of 15°.

Therefore, for transtemporal insonation of the MCA, the 2D transducer array design of this work is expected to provide adequate acoustic intensities at all applicable insonation regions.

The designed transducer array dimensions do not satisfy the grating lobe inequalities given in Equations 2.58 and 2.59. Therefore, the emergence of grating lobes is anticipated, as observed in the simulated results presented in Figure 3-16. However, because the velocity envelope method is used for Doppler velocity estimation, the presence of grating lobes should not affect velocimetry results unless high flow regions are observed outside the vessel of interest (i.e., MCA for this work). Such nonidealities in phased array beamformation will, nonetheless, increase system dynamic range and clutter filter requirements – due to additional receive energy from stationary scatterers.

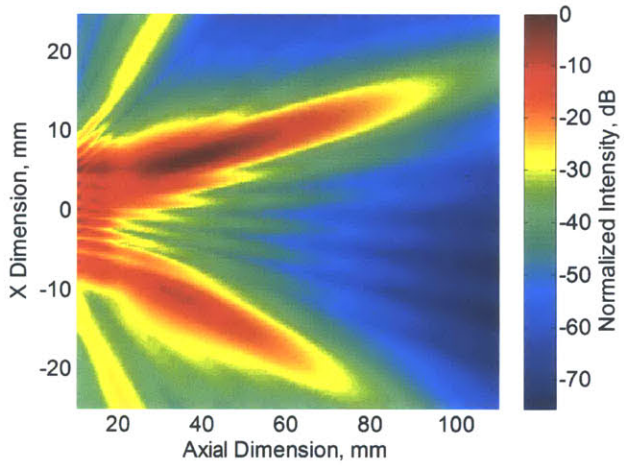

Figure 3-16: Simulated intensity beam pattern in the xz-plane at $y = 0$ mm for an 8x8 transducer array ($L_x = L_y = 1.6$mm, $\text{kerf}_x = \text{kerf}_y = 0.1$mm) with a desired focal region at $(10, 0, 60)$ mm.

Chapter 4

Experimental Characterization

Although theoretical analysis and simulation are vital during the design process, experimentation is needed to characterize and validate the electrical and acoustic performance of prototype TCD instrumentation. Specifically, the Prototype I system described in Section 3.6 will be experimentally evaluated. The transmit and receive signal paths are initially assessed separately. Functionality and accuracy of the TCD sonography system are then characterized for pulse-echo operation by employing a Doppler flow phantom.

4.1 Transmitter Characterization

Transmission properties of the TCD ultrasound system are first characterized electrically. Logic inputs into each channel of the HV pulser (i.e., HV748) are level shifted to the HV supply rails as shown in Figure 4-1. Under realistic loading conditions (i.e., C323-SU transducer element load), a propagation delay of $\approx$ 35 ns exists between the digital inputs and HV output of the pulser.

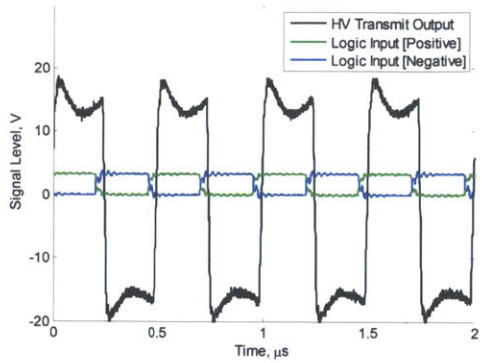

Figure 4-1: Logical inputs and HV output of an HV pulser channel under C323-SU transducer loading. For this measurement, ±20 V HV supply rails and low current drive mode (MC0= 0, MC1= 0) pulser settings are used.

From Figure 4-1, it is apparent that, under practical driving loads, the transmit excitation signal is not an ideal square waveform, as assumed in previous analyses. This nonideality is created by the interaction between the power supply and HV pulser impedances with the resonant characteristics of the ultrasound transducer and cable parasitics. These interactions lead to ringing in the HV transmit signal and an effective reduction in HV supply rail amplitude – thereby resulting in decreased acoustic output power. Figure 4-2 shows the excitation step response of the unloaded and transducer loaded HV pulser. Ringing is only appreciable in the case of the loaded transducer.

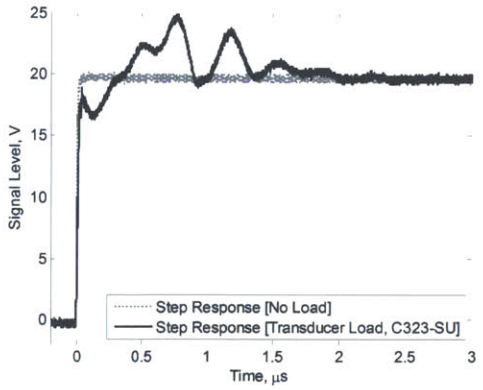

Figure 4-2: HV pulser positive step response for unloaded and C323-SU transducer loaded signal line. For this measurement, ±20 V HV supply rails and low current drive mode (MC0= 0, MC1= 0) pulser settings are used.

By employing a hydrophone (HNC-0400, ONDA, Sunnyvale, CA), the acoustic pressure due to a driven ultrasound transducer can be measured. The hydrophone and preamplifier (AH-2010, ONDA, Sunnyvale, CA) yield an output voltage waveform that, by accounting for the calibrated hydrophone and preamplifier transfer functions, yields an experimentally measured pressure waveform for the corresponding hydrophone location. Figure 4-3 presents the preamplifier output for an on-axis measurement at the last axial maximum in a water medium. Although the transmit excitation is a square waveform, a sinusoidal output is observed due to the bandpass filtering response of the acoustic transducer.

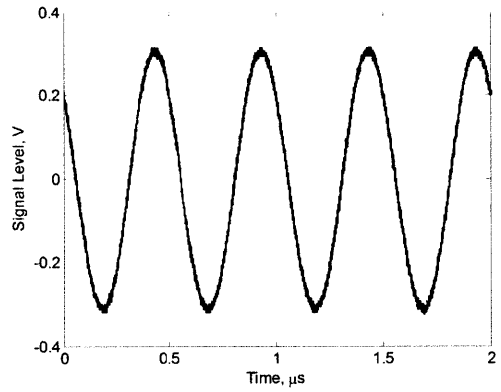

Figure 4-3: Hydrophone preamplifier output for an on-axis measurement $\approx$ 12 mm from the C323-SU transducer surface in a water medium using $\pm$20 V HV supply rails.

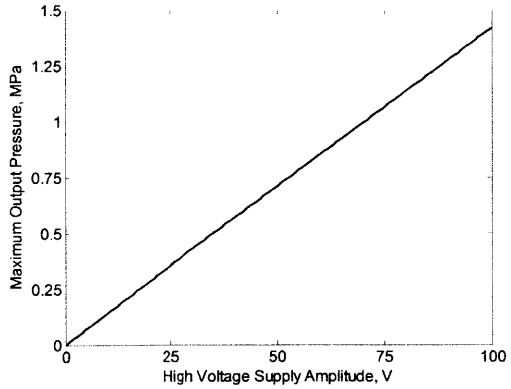

Figure 4-4: Maximum output pressure linearized dependence on HV voltage rail amplitude for the C323-SU transducer.

Assuming linearity for transduction and acoustic propagation, the maximum output pressure amplitude for the unfocused C323-SU transducer can be determined for a range of voltage rail amplitudes using Figure 4-4.

Recall from Equation 2.40, that the pressure at the last axial maximum p_{lam} for a circular transducer is twice the acoustic pressure at the transducer surface (assuming no apodization and neglecting attenuation effects, which are minimal in water). Maximum acoustic output power $W_{\max}$ is therefore computed as:

$$W_{\max} = \frac{\pi p_{lam}^2 D^2}{8Z} \tag{4.1}$$

where D is the transducer element diameter. For the C323-SU transducer excited at ± 20 V HV power supply rails, this yields a maximum acoustic output power of $W_{\max} = 0.84$ W.

4.2 Receiver Characterization

The receiver front end is characterized by inputting a low-level electrical tone at the electrical input/output port of each channel and determining the spectral content and gain characteristics of the receiver system for a variety of amplifier and ADC settings. Figure 4-5 shows the receive spectrum for a 7 mV amplitude, 2.0 MHz frequency sinusoid input. Measured output amplitude of 0.91 V was obtained, resulting in 42.2 dB of receiver gain. This measurement closely matches the expected 42 dB receiver gain (i.e., LNA gain: 24 dB, Attenuator gain: -6 dB, PGA gain: 24 dB).

From Figure 4-5, it is obvious that a substantial number of interferers exist, especially below 1.5 MHz. This is due mainly to a number of switching power supplies, which operate at various switching frequencies and can couple to the receiver input nodes. The fundamental and harmonic power supply switching frequencies were selected such that they do not occur at or near the desired 2.0 MHz operating frequency. Other potential sources of signal pickup – such as AM broadcast radio – may also be present in the receive spectrum.

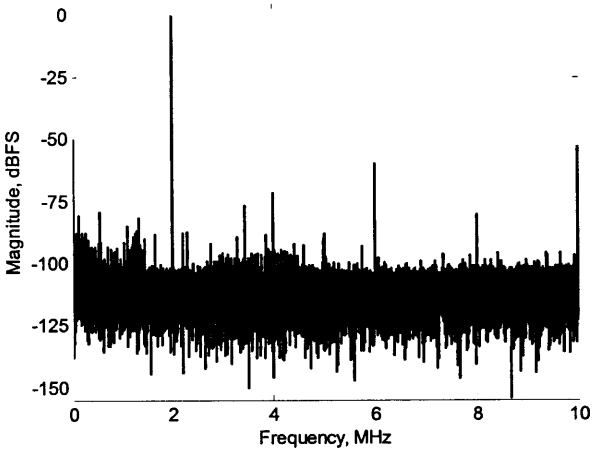

Figure 4-5: Receiver Nyquist-band frequency spectrum for a 7 mV amplitude, 2.0 MHz frequency sinusoidal input.

Although the presence of interferers can be detrimental to Doppler velocimetry accuracy, interferers occurring outside the bandwidth of the bandpass matched filter are highly attenuated and – assuming receiver saturation is avoided – have minimal effect on SNR. The bandpass RF filter impulse response can be modified to further attenuate interferers by realizing higher order filtering.

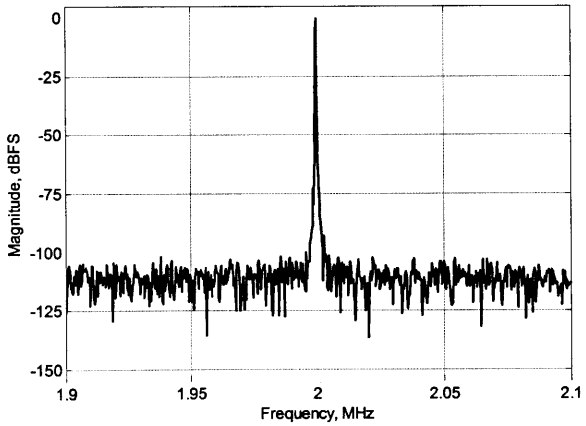

Figure 4-6: Receiver frequency spectrum over the RF filter bandwidth for a 7 mV amplitude, 2.0 MHz frequency sinusoidal input.

The receive signal spectrum is given in Figure 4-6 over the frequency range of interest (i.e., bandpass RF filter bandwidth), which presents no discernible interferers

and is therefore noise limited. An excitation frequency of 2.0 MHz with a ten cycle gate period (i.e., $M = 10$), results in a matched RF filter bandwidth of $BW_{3dB} = \frac{f_e}{M} = 200$ kHz. Integration of noise and distortion power over the bandpass RF filter bandwidth yields a signal-to-noise and distortion ratio ($SNDR$) greater than 80 dB, which has been established as adequate in commercial TCD sonography systems [27].

4.3 Flow Velocity Measurement

Pulse echo characteristics of the system – in addition to the Doppler processing algorithm – can be experimentally validated via flow phantom velocity measurements. The experimental flow phantom setup is presented in Figure 4-7. Blood mimicking fluid is utilized within the flow phantom to emulate the acoustic scattering properties of blood and is composed of water and 30 μm diameter alumina powder particles (AP300-1, South Bay Technology, San Clemente, CA). The vessel phantom is constructed from 6.35 mm inner diameter vinyl tubing (i.e., the available tubing diameter nearest to MCA diameter). A pump motor (C55JXGTS-3835, Emerson, St. Louis, MO) drives the blood mimicking fluid from the fluid reservoir through the flow phantom. A flow regulator is used to control the volumetric fluid flow, which is measured by an in-line flow meter (751021A08, King Instrument Company, Garden Grove, CA). It should be noted that – because the fluid reservoir and pump motor are open air systems and the blood mimicking fluid is not degassed – the flow phantom creates a substantial number of air bubbles, which are likely the dominant scattering mechanism. Therefore, due to a lack of skull bone and increased scattering, receive signal levels from the flow phantom setup are significantly higher than would be expected for *in vivo* measurements. Nonetheless, the flow phantom is suitable for demonstrating successful pulse echo operation of the ultrasound system and validating Doppler velocity estimation techniques.

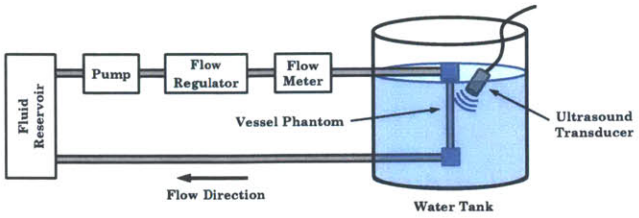

Figure 4-7: Experimental flow phantom setup for evaluation of ultrasound velocimetry instrumentation.

The vessel phantom and manually aligned ultrasound transducer are depicted within the experimental water tank setup in Figure 4-8. Because the vessel phantom can be insonated uniformly – due to visible transducer alignment and controlled vessel phantom course – and the Doppler angle and vessel phantom diameter can be accurately measured, the volumetric flow rate – or equivalently the mean flow velocity – can be used to determine the accuracy of the TCD velocimetry system from flow meter measurements. Although *in vivo* blood flow is pulsatile in nature, the flow phantom setup of this work generates steady flow and thus does not allow the dynamic measurement capabilities of the prototype TCD velocimetry system to be evaluated.

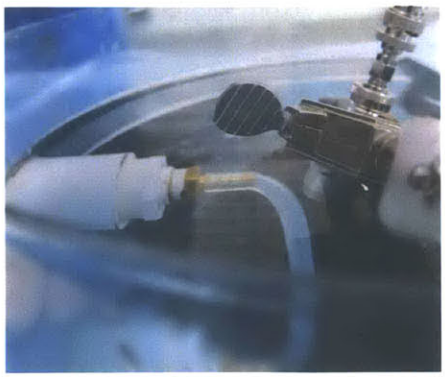

Figure 4-8: Alignment of the ultrasound transducer to the vessel phantom within the experimental flow phantom.

Figure 4-9 presents the Doppler spectrum of a single velocity measurement. Mean flow velocity and volumetric flow rate are computed using the Doppler angle, vessel diameter, and experimental Doppler spectrum as discussed in Section 2.4.2. A mean

flow velocity of -1.34 m/s (i.e., away from the transducer) is obtained via Doppler estimation, when accounting for a measured Doppler angle of 30°.

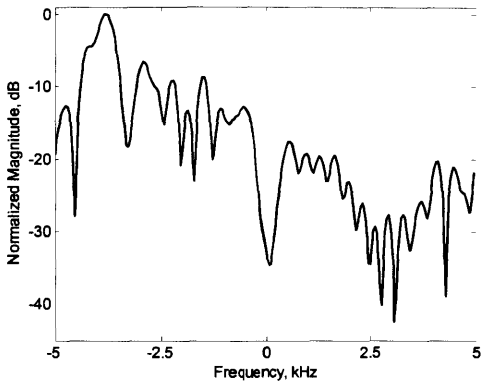

Figure 4-9: Experimental Doppler spectrum using flow phantom setup.

To validate the accuracy of the prototype TCD system, Doppler estimated mean flow velocities are compared to flow meter measurements over the range of anticipated *in vivo* flow velocities in the MCA. From Figure 4-10, it is visually evident that Doppler mean velocity estimations are highly correlated to inline flow meter measurements, which have been converted to mean velocities using known physical dimensions. A 12^{th} order Chebyshev high-pass filter is used for clutter rejection with a stopband frequency corresponding to a scatterer velocity of 6 cm/s.

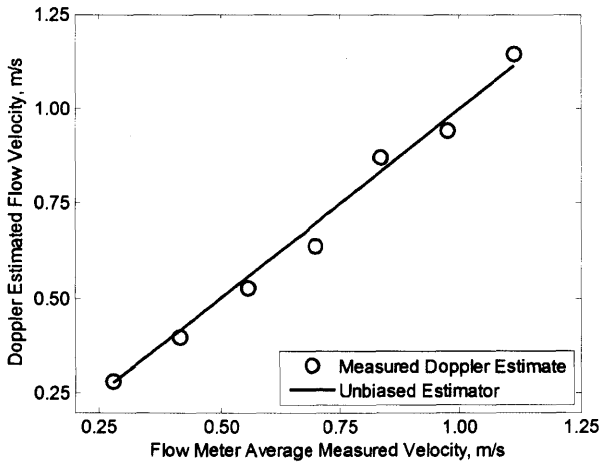

Figure 4-10: Comparison of Doppler estimated and flow meter measured mean flow velocities for expected *in vivo* values in the MCA.

Normalized root-mean-square error ($NRMSE$) analysis is employed to assess estimator performance over the complete experimental data set, as given by:

$$NRMSE = \frac{1}{\bar{v}_{\text{obs,max}} - \bar{v}_{\text{obs,min}}} \cdot \sqrt{\frac{\sum_{i=1}^{n} \left(\bar{v}_{\text{est},i} - \bar{v}_{\text{obs},i}\right)^2}{n}} \tag{4.2}$$

where $\bar{v}_{\text{est}}$ is the Doppler estimated mean velocity at each data point, $\bar{v}_{\text{obs}}$ is the observed mean velocity obtained from flow meter measurements, and n is the number of experimental data points. For the given data set, $NRMSE$ is computed as $< 3.5\%$.

Alternately, Doppler velocity estimation accuracy can be characterized using the difference parameter $\Delta\bar{v}_i = \bar{v}_{\text{est},i} - \bar{v}_{\text{obs},i}$. For the given data set, a difference mean of -0.44 cm/s and difference standard deviation of 3.11 cm/s were achieved. This realized degree of measurement accuracy suggests the potential for clinically acceptable blood flow velocity measurements obtained using the prototype TCD velocimetry instrumentation of this work.

Chapter 5

Conclusion

5.1 Summary

Monitoring of cerebrovascular state is an essential element in the clinical care of patients affected by neurovascular pathologies. Transcranial Doppler (TCD) sonography is a non-invasive method that enables the measurement of blood flow velocities from the basal intracerebral vessels and is clinically indicated in a variety of diagnostic and prognostic neurovascular applications [22]. Although TCD sonography provides several considerable advantages when compared to other measurement modalities – notably safety in prolonged studies, relatively modest system dimensions and equipment costs, and high temporal resolution – the widespread clinical acceptance and adoption of TCD sonography in both conventional (e.g., identification of intracranial vasospasm and stenosis, cerebral embolism detection) and emerging (e.g., intracranial pressure estimation) applications has been hindered by numerous limitations [23,24]. Among these impediments are the need for an experienced operator, velocimetry accuracy and variation concerns, the absence of a patent acoustic window in certain patients, and restrictive measurement techniques and system form factors for certain applications.

In an effort to mitigate these constraints, this work details the development of a highly-compact, wearable TCD ultrasound system for autonomous and continuous measurement of cerebral blood flow velocity (CBFV). To facilitate development, this

work concentrates on unilateral insonation of the middle cerebral artery (MCA).

Relevant theoretical considerations and design of the Prototype I system were presented in Chapters 2 and 3. The eight channel Prototype I system was then characterized and validated using a flow phantom in Chapter 4, which demonstrated a high level of agreement when compared to flow meter measurements under realistic *in vivo* flow velocities.

5.2 Future Work

The following items are anticipated next steps of this project and will be part of subsequent research:

- **Clinical testing of the Prototype I system**

  Despite successful validation of the Prototype I system using a Doppler flow phantom, the acoustic context is significantly different from *in vivo* conditions. The presence of cranial bone significantly complicates measurements, due to acoustic beam distortion and substantial attenuation. Additionally, the flow phantom of this work does not capture the pulsatile nature of blood velocities and therefore characterization of the Prototype I system during measurement of dynamic velocities cannot be performed using the flow phantom. Clinical testing of the Prototype I system is therefore needed, which will compare the systolic, diastolic, and time-averaged flow velocities of the prototype system to data measured using a commercial TCD ultrasound system under similar physiological conditions.

- **Development of increased channel count discrete prototype system**

  Although the Prototype I is a multi-channel system, the operable system uses single element transducers – since a transducer array is not yet available. Additionally, under the proposed architecture of this work, the eight channel electronics are insufficient for beamformation using a 2D transducer array. Extension of the Prototype I system architecture to higher channel count (i.e., 64 channels)

and incorporation with a 2D transducer array, will enable acceptable phased array operation. To achieve untethered operation, additional high voltage power supply generation from a single battery and system memory for data storage are also required.

- **Development of phased array algorithms**

  The need for operator interaction, particularly for manual transducer steering and alignment, can be substantially reduced through developments in vessel location and tracking algorithms. Also, acoustic window patency considerations can be potentially mitigated through the implementation of phase-correction algorithms, which restore acoustic pressures within the focal region in the presence of beam distortion. These techniques require an operational phased array platform for electronic beam steering and therefore cannot be tested or refined prior to the development of a functional phased array system.

- **Use case refinement**

  Further exploration into potential use cases of autonomous TCD sonography may lead to system level modifications in future system developments. Such revisions may include the need for bilateral insonation modes, extension to insonation of additional cerebral vessels, modification of the operator interface and mechanical construction, and inclusion of radio-based data transmission. Input from clinicians, sonographer technologists, and potential users will be sought.

- **Development of integrated circuit electronics**

  Transitioning from discrete commercially available components to integrated circuit based designs leads to a much broader set of realizable system architectures. After the system requirements have been sufficiently defined using discrete components, an application specific integrated circuit (ASIC) can be designed to significantly reduce both system dimensions – due to increased device density, smaller routing dimensions, and reduced electrical component count – and power dissipation – due to mixed signal architectural approaches, reductions in intermediate data rates, and power efficient design implementations. Following

circuit integration, the realization of a truly untethered and wearable system form factor for TCD sonography will be increasingly viable.

The successful execution of our current objectives and future work has the potential to profoundly alter the current clinical approach to neurovascular diagnostics, especially in cases where the role of diagnostic tools has not been clearly established (e.g., emergency assessment of head trauma and stroke, ambulatory intracranial pressure monitoring for cases of moderate traumatic brain injury, home monitoring of hydrocephalus shunt function, long-term monitoring cerebral embolization).

Bibliography

[1] F. J. M. Walters, "Intracranial pressure and cerebral blood flow," *Update in Anesthesia, Physiology*, vol. 8, pp. 18–23, 1998.

[2] H. White and B. Venkatesh, "Applications of transcranial Doppler in the ICU: a review," *Intensive Care Medicine*, vol. 32, pp. 981–994, 2006.

[3] F. M. Kashif, *Modeling and estimation for non-invasive monitoring of intracranial pressure and cerebrovascular autoregulation.* PhD thesis, Massachusetts Institute of Technology, 2011.

[4] H. S. Markus, "Transcranial Doppler ultrasound," *British Medical Bulletin*, vol. 56, no. 2, pp. 378–388, 2000.

[5] H. S. Markus, "Transcranial Doppler ultrasound," *Journal of Neurology, Neurosurgery & Psychiatry*, vol. 67, no. 2, pp. 135–137, 1999.

[6] M. Saqqur, D. Zygun, and A. Demchuk, "Role of transcranial Doppler in neurocritical care," *Crit Care Med*, vol. 35, pp. S216–S223, May 2007.

[7] C. Lysakowski, B. Walder, M. C. Costanza, and M. R. Tramr, "Transcranial Doppler versus angiography in patients with vasospasm due to a ruptured cerebral aneurysm," *Stroke*, vol. 32, no. 10, pp. 2292–2298, 2001.

[8] M. Can, O. Kahyaoglu, I. Colak, and Y. Aydin, "Predictive value of transcranial Doppler to detect clinical vasospasm in patients with aneurysmal subarachnoid haemorrhage," in *Cerebral Vasospasm*, vol. 104 of *Acta Neurochirurgica Supplementum*, pp. 259–261, Springer Vienna, 2008.

[9] P. Y. Han, J. H. Kim, H. I. Kang, B. G. Moon, S. J. Lee, and J. S. Kim, "Is transcranial Doppler ultrasonography old-fashioned?: One institutional validity study," *J Korean Neurosurg Soc*, vol. 44, pp. 63–66, Aug. 2008.

[10] R. J. Adams, V. C. McKie, E. M. Carl, F. T. Nichols, R. Perry, K. Brock, K. McKie, R. Figueroa, M. Litaker, S. Weiner, and D. Brambilla, "Long-term stroke risk in children with sickle cell disease screened with transcranial Doppler," *Annals of Neurology*, vol. 42, no. 5, pp. 699–704, 1997.

[11] R. J. Adams, V. C. McKie, L. Hsu, B. Files, *et al.*, "Prevention of a first stroke by transfusions in children with sickle cell anemia and abnormal results on transcranial Doppler ultrasonography," *New England Journal of Medicine*, vol. 339, no. 1, pp. 5–11, 1998.

[12] H. S. Markus and A. MacKinnon, "Asymptomatic embolization detected by Doppler ultrasound predicts stroke risk in symptomatic carotid artery stenosis," *Stroke*, vol. 36, no. 5, pp. 971–975, 2005.

[13] A. D. Mackinnon, R. Aaslid, and H. S. Markus, "Ambulatory transcranial Doppler cerebral embolic signal detection in symptomatic and asymptomatic carotid stenosis," *Stroke*, vol. 36, no. 8, pp. 1726–1730, 2005.

[14] A. R. Lupetin, D. A. Davis, I. Beckman, and N. Dash, "Transcranial Doppler sonography. part 2. evaluation of intracranial and extracranial abnormalities and procedural monitoring.," *Radiographics*, vol. 15, no. 1, pp. 193–209, 1995.

[15] M. P. Spencer, "Transcranial Doppler monitoring and causes of stroke from carotid endarterectomy," *Stroke*, vol. 28, no. 4, pp. 685–691, 1997.

[16] W. Pugsley, L. Klinger, C. Paschalis, T. Treasure, M. Harrison, and S. Newman, "The impact of microemboli during cardiopulmonary bypass on neuropsychological functioning.," *Stroke*, vol. 25, no. 7, pp. 1393–1399, 1994.

[17] R. Aaslid, K. F. Lindegaard, W. Sorteberg, and H. Nornes, "Cerebral autoregulation dynamics in humans.," *Stroke*, vol. 20, no. 1, pp. 45–52, 1989.

[18] F. Kashif, T. Heldt, and G. Verghese, "Model-based estimation of intracranial pressure and cerebrovascular autoregulation," in *Computers in Cardiology, 2008*, pp. 369–372, Sep. 2008.

[19] Orlando Regional Healthcare, *Overview of Adult Traumatic Brain Injuries.* Orlando Regional Healthcare, Orlando, FL, 2004.

[20] J. A. Langlois, W. Rutland-Brown, and M. M. Wald, "The epidemiology and impact of traumatic brain injury: a brief overview," *J Head Trauma Rehabil*, vol. 21, pp. 375–378, Sep. – Oct. 2006.

[21] M. R. Bullock and J. T. Povlishock, "Guidelines for the management of severe traumatic brain injury. editor's commentary," *J Neurotrauma*, vol. 24 Suppl 1, pp. S1–S106, 2007.

[22] M. Sloan, A. Alexandrov, C. Tegeler, M. Spencer, L. Caplan, E. Feldmann, L. Wechsler, D. Newell, C. Gomez, V. Babikian, *et al.*, "Assessment: transcranial Doppler ultrasonography report of the Therapeutics and Technology Assessment Subcommittee of the American Academy of Neurology," *Neurology*, vol. 62, no. 9, pp. 1468–1481, 2004.

[23] Q. Shen, J. Stuart, B. Venkatesh, J. Wallace, and J. Lipman, "Inter observer variability of the transcranial Doppler ultrasound technique: Impact of lack of practice on the accuracy of measurement," *Journal of Clinical Monitoring and Computing*, vol. 15, pp. 179–184, 1999.

[24] B. Venkatesh, Q. Shen, and J. Lipman, "Continuous measurement of cerebral blood flow velocity using transcranial Doppler reveals significant moment-to-moment variability of data in healthy volunteers and in patients with subarachnoid hemorrhage," *Crit Care Med*, vol. 30, pp. 563–569, Mar. 2002.

[25] N. A. Martin, K. M. Thomas, and M. Caron, "Transcranial Doppler–techniques, application, and instrumentation," *Neurosurgery*, vol. 33, pp. 761–764, Oct. 1993.

[26] G. Tsivgoulis, V. Sharma, and A. Alexandrov, "Multi-depth power M-mode Doppler in the evaluation of acute cerebral ischemia," in *Science Innovation Synergy Symposiums in Cardiac and Vascular Medicine 2007 Yearbook*, pp. 42–54, 2007.

[27] M. A. Moehring and M. P. Spencer, "Power M-mode Doppler (PMD) for observing cerebral blood flow and tracking emboli," *Ultrasound Med Biol*, vol. 28, pp. 49–57, Jan. 2002.

[28] R. W. Baumgartner, ed., *Handbook on neurovascular ultrasound*, vol. 21 of *Frontiers of neurology and neuroscience*. Basel, Switzerland: Karger, first ed., 2006.

[29] C. J. McMahon, P. McDermott, D. Horsfall, J. R. Selvarajah, A. T. King, and A. Vail, "The reproducibility of transcranial Doppler middle cerebral artery velocity measurements: implications for clinical practice," *Br J Neurosurg*, vol. 21, pp. 21–27, Feb. 2007.

[30] M. Corriveau and K. Johnston, "Interobserver variability of carotid Doppler peak velocity measurements among technologists in an ICAVL-accredited vascular laboratory," *Journal of Vascular Surgery*, vol. 39, no. 4, pp. 735–741, 2004.

[31] L. R. Wechsler and V. L. Babikian, "Transcranial Doppler sonography: Clinically useful," *Arch Neurol*, vol. 51, pp. 1054–1056, Oct. 1994.

[32] M. Marinoni, A. Ginanneschi, P. Forleo, and L. Amaducci, "Technical limits in transcranial Doppler recording: Inadquate acoustic windows," *Ultrasound in Medicine & Biology*, vol. 23, no. 8, pp. 1275–1277, 1997.

[33] T. Gerriets, G. Seidel, I. Fiss, B. Modrau, and M. Kaps, "Contrast-enhanced transcranial color-coded duplex sonography: efficiency and validity," *Neurology*, vol. 52, pp. 1133–1137, Apr. 1999.

[34] G. T. Clement, J. White, and K. Hynynen, "Investigation of a large-area phased array for focused ultrasound surgery through the skull," *Phys Med Biol*, vol. 45, pp. 1071–1083, Apr. 2000.

[35] S. Deverson, D. H. Evans, and D. Bouch, "The effects of temporal bone on transcranial Doppler ultrasound beam shape," *Ultrasound in Medicine & Biology*, vol. 26, no. 2, pp. 239–244, 2000.

[36] G. T. Clement and K. Hynynen, "A non-invasive method for focusing ultrasound through the human skull," *Phys Med Biol*, vol. 47, pp. 1219–1236, Apr. 2002.

[37] A. D. Mackinnon, R. Aaslid, and H. S. Markus, "Long-term ambulatory monitoring for cerebral emboli using transcranial Doppler ultrasound," *Stroke*, vol. 35, no. 1, pp. 73–78, 2004.

[38] J. Jensen, "Field: A program for simulating ultrasound systems," *Medical and Biological Engineering and Computing*, vol. 34, Supplement 1, pp. 351–353, 1996.

[39] J. Jensen and N. Svendsen, "Calculation of pressure fields from arbitrarily shaped, apodized, and excited ultrasound transducers," *Ultrasonics, Ferroelectrics and Frequency Control, IEEE Transactions on*, vol. 39, no. 2, pp. 262–267, 1992.

[40] T. L. Szabo, *Diagnostic ultrasound imaging: inside out.* Academic Press series in biomedical engineering, Burlington, MA: Elsevier Academic Press, first ed., 2004.

[41] F. A. Duck, "Nonlinear acoustics in diagnostic ultrasound," *Ultrasound in Medicine & Biology*, vol. 28, no. 1, pp. 1–18, 2002.

[42] T. Duck, A. Baker, and H. Starritt, eds., *Ultrasound in medicine.* Medical science series, Bristol, UK: Institute of Physics Publishing, first ed., 1998.

[43] J. A. Jensen, *Estimation of blood velocities using ultrasound: a signal processing approach.* New York, NY: Cambridge University Press, first ed., 1996.

[44] D. A. Christensen, *Ultrasonic bioinstrumentation.* New York, NY: John Wiley & Sons, first ed., 1988.

[45] F. T. Ulaby, *Fundamentals of Applied Electromagnetics.* Upper Saddle River, NJ: Pearson Prentice Hall, fifth ed., 2007.

[46] D. Evans and W. McDicken, *Doppler ultrasound: physics, instrumentation, and signal processing.* New York, NY: Wiley, second ed., 2000.

[47] D. K. Nassiri and C. R. Hill, "The differential and total bulk acoustic scattering cross sections of some human and animal tissues," *The Journal of the Acoustical Society of America*, vol. 79, no. 6, pp. 2034–2047, 1986.

[48] K. K. Shung and G. Thieme, eds., *Ultrasonic scattering in biological tissues.* Boca Raton, FL: CRC, first ed., 1993.

[49] K. K. Shung, R. Sigelmann, J. Reid, *et al.*, "Scattering of ultrasound by blood," *Biomedical Engineering, IEEE Transactions on*, vol. 23, no. 6, pp. 460–467, 1976.

[50] Y. W. Yuan and K. K. Shung, "Ultrasonic backscatter from flowing whole blood – I: Dependence on shear rate and hematocrit," *The Journal of the Acoustical Society of America*, vol. 84, no. 1, pp. 52–58, 1988.

[51] Y. W. Yuan and K. K. Shung, "Ultrasonic backscatter from flowing whole blood – II: Dependence on frequency and fibrinogen concentration," *The Journal of the Acoustical Society of America*, vol. 84, no. 4, pp. 1195–1200, 1988.

[52] K. K. Shung, G. Cloutier, and C. Lim, "The effects of hematocrit, shear rate, and turbulence on ultrasonic Doppler spectrum from blood," *Biomedical Engineering, IEEE Transactions on*, vol. 39, pp. 462–469, May 1992.

[53] H. S. Markus and M. M. Brown, "Differentiation between different pathological cerebral embolic materials using transcranial Doppler in an in vitro model," *Stroke*, vol. 24, no. 1, pp. 1–5, 1993.

[54] A. Oliner, R. Li, and H. Bertoni, "Catalog of acoustic equivalent networks for planar interfaces," *Proceedings of the IEEE*, vol. 60, pp. 1513–1518, Dec. 1972.

[55] M. Hayner and K. Hynynen, "Numerical analysis of ultrasonic transmission and absorption of oblique plane waves through the human skull," *The Journal of the Acoustical Society of America*, vol. 110, no. 6, pp. 3319–3330, 2001.

[56] G. T. Clement, P. J. White, and K. Hynynen, "Enhanced ultrasound transmission through the human skull using shear mode conversion," *The Journal of the Acoustical Society of America*, vol. 115, no. 3, pp. 1356–1364, 2004.

[57] R. Aaslid, *Transcranial Doppler sonography.* Wien, Austria: Springer-Verlag, first ed., 1986.

[58] I. Wygant, X. Zhuang, D. Yeh, O. Oralkan, A. Ergun, M. Karaman, and B. Khuri-Yakub, "Integration of 2D CMUT arrays with front-end electronics for volumetric ultrasound imaging," *Ultrasonics, Ferroelectrics and Frequency Control, IEEE Transactions on*, vol. 55, no. 2, pp. 327–342, 2008.

[59] D. Leedom, R. Krimholtz, and G. Matthaei, "Equivalent circuits for transducers having arbitrary even-or odd-symmetry piezoelectric excitation," *Sonics and Ultrasonics, IEEE Transactions on*, vol. 18, no. 3, pp. 128–141, 1971.

[60] B. Steinberg, "Digital beamforming in ultrasound," *Ultrasonics, Ferroelectrics and Frequency Control, IEEE Transactions on*, vol. 39, pp. 716–721, Nov. 1992.

[61] A. Oppenheim and R. Schafer, *Discrete-time signal processing.* Upper Saddle River, NJ: Prentice Hall, third ed., 2010.

[62] G. Tupholme, "Generation of acoustic pulses by baffled plane pistons," *Mathematika*, vol. 16, pp. 209–224, 1969.

[63] P. Stepanishen, "The time-dependent force and radiation impedance on a piston in a rigid infinite planar baffle," *The Journal of the Acoustical Society of America*, vol. 49, pp. 841–849, 1971.

[64] J. A. Jensen, "A model for the propagation and scattering of ultrasound in tissue," *The Journal of the Acoustical Society of America*, vol. 89, no. 1, pp. 182–190, 1991.

[65] P. Stepanishen, "Pulsed transmit/receive response of ultrasonic piezoelectric transducers," *The Journal of the Acoustical Society of America*, vol. 69, pp. 1815–1827, 1981.

[66] U. Vyas and D. Christensen, "Ultrasound beam simulations in inhomogeneous tissue geometries using the hybrid angular spectrum method," *IEEE Trans Ultrason Ferroelectr Freq Control*, vol. 59, pp. 1093–1100, Jun. 2012.

[67] D. Newell and R. Aaslid, *Transcranial Doppler*. Raven Press, 1992.

[68] P. Huber and J. Handa, "Effect of contrast material, hypercapnia, hyperventilation, hypertonic glucose and papaverine on the diameter of the cerebral arteries. Angiographic determination in man," *Investigative Radiology*, vol. 2, no. 1, pp. 17–32, 1967.

[69] J. M. Serrador, P. A. Picot, B. K. Rutt, J. K. Shoemaker, and R. L. Bondar, "MRI measures of middle cerebral artery diameter in conscious humans during simulated orthostasis," *Stroke*, vol. 31, no. 7, pp. 1672–1678, 2000.

[70] J. Valdueza, J. Balzer, A. Villringer, T. Vogl, R. Kutter, and K. Einhäupl, "Changes in blood flow velocity and diameter of the middle cerebral artery during hyperventilation: assessment with MR and transcranial Doppler sonography," *American Journal of Neuroradiology*, vol. 18, no. 10, pp. 1929–1934, 1997.

[71] K. Lindegaard, T. Lundar, J. Wiberg, D. Sjøberg, R. Aaslid, and H. Nornes, "Variations in middle cerebral artery blood flow investigated with noninvasive transcranial blood velocity measurements," *Stroke*, vol. 18, no. 6, pp. 1025–1030, 1987.

[72] A. Dahl, D. Russell, R. Nyberg-Hansen, and K. Rootwelt, "Effect of nitroglycerin on cerebral circulation measured by transcranial Doppler and SPECT," *Stroke*, vol. 20, no. 12, pp. 1733–1736, 1989.

[73] S. Satomura and Z. Kaneko, "Ultrasonic blood rheograph," in *Proceedings of the 3rd International Conference on Medical Electronics*, pp. 254–258, 1960.

[74] R. Aaslid, T. Markwalder, and H. Nornes, "Noninvasive transcranial Doppler ultrasound recording of flow velocity in basal cerebral arteries," *Journal of Neurosurgery*, vol. 57, no. 6, pp. 769–774, 1982.

[75] O. Bonnefous, P. Pesque, and X. Bernard, "A new velocity estimator for color flow mapping," in *IEEE 1986 Ultrasonics Symposium*, pp. 855–860, IEEE, 1986.

[76] P. Magnin, "A review of Doppler flow mapping techniques," in *IEEE 1987 Ultrasonics Symposium*, pp. 969–978, IEEE, 1987.

[77] J. Womersley, "Oscillatory motion of a viscous liquid in a thin-walled elastic tube – I: The linear approximation for long waves," *Philosophical Magazine*, vol. 46, no. 373, pp. 199–221, 1955.

[78] D. Evans, "Some aspects of the relationship between instantaneous volumetric blood flow and continuous wave Doppler ultrasound recordings – III," *Ultrasound in Medicine & Biology*, vol. 8, no. 6, pp. 617–623, 1982.

[79] E. Kandel, J. Schwartz, T. Jessell, *et al.*, *Principles of neural science*, vol. 4. McGraw-Hill New York, 2000.

[80] M. de Boorder, J. van der Grond, A. van Dongen, C. Klijn, L. Jaap Kappelle, P. Van Rijk, and J. Hendrikse, "Spect measurements of regional cerebral perfusion and carbondioxide reactivity: Correlation with cerebral collaterals in internal carotid artery occlusive disease," *Journal of Neurology*, vol. 253, no. 10, pp. 1285–1291, 2006.

[81] Wikipedia, "Circle of Willis — Wikipedia, the free encyclopedia," 2012. [Online; accessed 3 November 2012].

[82] H. Riggs and C. Rupp, "Variation in form of circle of Willis: the relation of the variations to collateral circulation: anatomic analysis," *Archives of Neurology*, vol. 8, no. 1, pp. 24–30, 1963.

[83] P. Hodes, F. Campoy, H. Riggs, and P. Bly, "Cerebral angiography: fundamentals in anatomy and physiology," *The American Journal of Roentgenology, Radium Therapy, and Nuclear Medicine*, vol. 70, no. 1, pp. 63–82, 1953.

[84] T. JF, *Cerebrovascular disorders*. New York, NY: Raven Press, third ed., 1984.

[85] T. Gabrielsen and T. Greitz, "Normal size of the internal carotid, middle cerebral and anterior cerebral arteries," *Acta Radiologica: Diagnosis*, vol. 10, no. 1, pp. 1–10, 1970.

[86] K. K. Jain, "Some observations on the anatomy of the middle cerebral artery," *Canadian Journal of Surgery*, vol. 7, pp. 134–139, 1964.

[87] A. Harders and J. Gilsbach, "Transcranial Doppler sonography and its application in extracranial-intracranial bypass surgery," *Neurol Res*, vol. 7, pp. 129–141, Sep. 1985.

[88] R. Gosling and D. King, "Arterial assessment by Doppler-shift ultrasound," *Proceedings of the Royal Society of Medicine*, vol. 67, no. 6 Pt 1, pp. 447–449, 1974.

[89] A. Baker, D. Evans, D. Prytherch, D. Morton, S. Bentley, M. Asher, and P. Bell, "Some failings of pulsatility index and damping factor," *Ultrasound in Medicine & Biology*, vol. 12, no. 11, pp. 875–881, 1986.

[90] J. Bellner, B. Romner, P. Reinstrup, K. Kristiansson, E. Ryding, L. Brandt, *et al.*, "Transcranial Doppler sonography pulsatility index (PI) reflects intracranial pressure (ICP)," *Surgical Neurology*, vol. 62, no. 1, pp. 45–50, 2004.

[91] A. Lupetin, D. Davis, I. Beckman, and N. Dash, "Transcranial Doppler sonography. part 1. principles, technique, and normal appearances," *Radiographics*, vol. 15, no. 1, pp. 179–191, 1995.

[92] A. A. Jarquin-Valdivia, J. McCartney, D. Palestrant, S. C. Johnston, and D. Gress, "The thickness of the temporal squama and its implication for transcranial sonography," *Journal of Neuroimaging*, vol. 14, no. 2, pp. 139–142, 2004.

[93] K. Hynynen and F. Jolesz, "Demonstration of potential noninvasive ultrasound brain therapy through an intact skull," *Ultrasound in Medicine & Biology*, vol. 24, no. 2, pp. 275–283, 1998.

[94] Spencer Technologies, *ST3 Digital Transcranial Doppler System Model PMD150 Operator's Manual.* Spencer Tecchnologies, Seattle, WA, 2009.

[95] A. Comerota, M. Katz, J. Hosking, H. Hashemi, R. Kerr, and A. Carter, "Is transcranial Doppler a worthwhile addition to screening tests for cerebrovascular disease?," *Journal of Vascular Surgery*, vol. 21, no. 1, pp. 90–97, 1995.

[96] U.S. Department of Health and Human Services, *Guidance for industry and FDA staff - information for manufacturers seeking marketing clearance of diagnostic ultrasound systems and transducers.* U.S. Department of Health and Human Services, Rockville, MD, 2008.

[97] AIUM, *Bioeffects and safety of diagnostic ultrasound.* Laurel, MD: AIUM Publications, 1998.

[98] British Medical Ultrasound Society, *Guidelines for the safe use of diagnostic ultrasound equipment.* British Medical Ultrasound Society, London, UK, 2009.

[99] D. Baker, "Pulsed ultrasonic Doppler blood-flow sensing," *Sonics and Ultrasonics, IEEE Transactions on*, vol. 17, pp. 170–184, Jul. 1970.